

Hypersonic Elastic Excitations in Soft Mesoscopic Structures

— A Brillouin light scattering study

DISSERTATION

zur Erlangung des Grades
"Doktor der Naturwissenschaften"

am Fachbereich Chemie, Pharmazie und Geowissenschaften
der Johannes Gutenberg-Universität Mainz

vorgelegt von

Master-Chem. **Wei Cheng**
geb.: 02.04.1979
aus Hunan/China

Mainz, 2007

Tag der mündlichen prüfung: March 23rd, 2007

Dekan: Prof. Dr. Peter Langguth

1. Berichterstatter: Prof. Dr. Hans-Jürgen Butt (MPIP)
2. Berichterstatter: Prof. Dr. Manfred Schmidt (Uni-Mainz)
3. Berichterstatter: Prof. Dr. Christos N. Likos (Uni-Düsseldorf)

Die vorliegende Arbeit wurde im Zeitraum von Juni 2004 bis Dezember 2006 am Max-Planck-Institute für Polymerforschung in Mainz unter der Anleitung von Herrn Prof. Dr. H.-J. Butt und Herrn Prof. Dr. G. Fytas angefertigt.

献给我最亲爱的父母...

(To my dearest parents...)

Preface

This dissertation is devoted to the experimental exploration of the propagation of elastic waves in soft mesoscopic structures with submicrometer dimensions. A strong motivation of this work is the large technological relevance and the fundamental importance of the subject. Elastic waves are accompanied by time-dependent fluctuations of local stress and strain fields in the medium. As such, the propagation phase velocities are intimately related to the elastic moduli. Knowledge of the elastic wave propagation directly provides information about the mechanical properties of the probed mesoscopic structures, which are not readily accessible experimentally. On the other hand, elastic waves, when propagating in an inhomogeneous medium with spatial inhomogeneities comparable to their wavelength, exhibit rather rich behavior, including the appearance of novel physical phenomena, such as phononic bandgap formation. So far, the experimental work has been restricted to macroscopic structures, which limit wave propagation below the KHz range. It was anticipated that an experimental approach capable of probing the interplay of the wave propagation with the controlled mesoscopic structures would contribute to deeper insights into the fundamental problem of elastic wave propagation in inhomogeneous systems.

The mesoscopic nature of the structures to be studied precludes the use of traditional methods, such as sound transmission, for the study of elastic wave propagation. In this work, an optical method utilizing the inelastic scattering of photons by GHz frequency thermally excited elastic waves, known as Brillouin light scattering spectroscopy (BLS), was employed. Two important classes of soft structures were investigated: thin films and colloidal crystals. For the former, the main interest was the effect of the one-dimensional (1D) confinement on the wave propagation due to the presence of the free-surface or interface of the layer and the utilization of these waves to extract relevant material parameters. For the second system, the primary interest was the interaction of the elastic wave and the strong scattering medium with local resonance units in a three-dimensional (3D) periodic arrangement.

The dissertation is organized as follows. Chapter 1 serves as a general introduction and the background of the present work. In Chapter 2 and Chapter 3, the physical principles of elastic wave propagation and the BLS method necessary for comprehending the results in later chapters are introduced. Chapter 4 is devoted to the experimental technique encompassing the tandem Fabry-Perot interferometer and the related scattering geometry. From Chapter 5 to Chapter 8, the BLS results for the various mesoscopic structures are presented, including thin supported polymer films, multilayer polymer films, dry colloidal crystals, and wet colloidal crystals. In Chapter 9 a brief summary and perspectives are provided.

Table of contents

Chapter 1

Introduction	1
---------------------------	---

Chapter 2

Elastic wave propagation in solids	6
2.1 Elasticity fundamentals	6
2.1.1 Stress and strain	6
2.1.2 Hook's law	8
2.1.3 Elastic moduli of isotropic bodies	9
2.2 Elastic waves in isotropic media	11
2.2.1 Longitudinal and transverse waves	11
2.2.2 Spherical-wave solutions	12
2.3 Elastic waves in supported thin layers	14
2.4 Vibrations of an elastic sphere	21
2.4.1 Vibration eigenmodes	21
2.4.2 Single sphere scattering	23
2.5 Elastic waves in periodic elastic composites	26
2.5.1 General overview	26
2.5.2 The plane-wave (PW) method	27
2.5.3 The multiple-scattering (MS) method	31

Chapter 3

Light scattering basics	35
3.1 Fundamental light scattering theory	35
3.2 Introduction to BLS	39
3.2.1 A simple approach to BLS	40
3.2.2 A thermodynamic approach to BLS	42
3.3 Some remarks	47
3.4 Surface BLS	48

Chapter 4

Brillouin light scattering instrumentation	50
4.1 Introduction to Fabry-Perot interferometer	50
4.1.1 Multiple beam interference	50
4.1.2 Standard Fabry-Perot interferometer	53
4.1.3 Tandem Fabry-Perot interferometer	56
4.2 Experimental setup	59
4.3 Scattering geometry	61

Chapter 5

Elastic excitations in supported thin polymer films	65
5.1 Introduction	65
5.2 Experimental	66
5.2.1 Sample preparation	66

5.2.2	Film characterization	67
5.3	Results and discussion	69
5.3.1	Elastic constants	69
5.3.2	Glass transition	76

Chapter 6

Elastic excitations in 1D polymeric photonic structures	83	
6.1	Introduction	83
6.2	Film characterization	84
6.3	Results and discussion	85
6.3.1	Dispersion relation for in-plane phonon propagation	85
6.3.2	Finite element analysis (FEA) modeling	88
6.3.3	Temperature dependence of the elastic constants	92
6.3.4	Mechanical anisotropy	94

Chapter 7

Elastic excitations in dry colloidal crystals	97	
7.1	Introduction	97
7.2	PS colloidal crystal film preparation	98
7.3	Results and discussion	100
7.3.1	Brillouin spectra	100
7.3.2	Eigenmodes identification	102
7.3.3	Particle size distribution	105
7.3.4	The low-frequency continuum	107
7.4	An application of the particle eigenfrequencies	108
7.4.1	Introduction	108
7.4.2	Results	109

Chapter 8

Elastic excitations in wet colloidal crystals	112	
8.1	Introduction	112
8.2	Experimental	114
8.3	Results and discussion	116
8.3.1	Hypersonic Bragg gap formation	116
8.3.2	Hypersonic Bragg gap tuning	118
8.3.3	Hybridization gap effect	122
8.3.4	Some remarks	127

Chapter 9

Epilogue	129	
9.1	Conclusions	129
9.2	Outlook	131

Bibliography	133
---------------------------	-----

Acknowledgement	141
------------------------------	-----

Curriculum Vitae	143
-------------------------------	-----

Chapter 1

Introduction

It is generally acknowledged that many of the true breakthroughs in technology have their roots in a deeper understanding of the properties of materials. The use of materials from which major tools have been constructed has had such a significant impact that archaeologists refer to those materials to classify the prehistoric human societies, e.g. the Bronze Age. The past century has witnessed the greatest changes in human history, results benefiting chiefly from the advanced comprehension of nature that has enabled manifold significant technological progress permeating every corner of life. Once again, the discovery and usage of new materials have played paramount roles. For instance, one can try to imagine what would happen if synthetic polymers are removed from daily life, being aware that they are essentially the chemical building blocks of plastics, rubbers, fibers, paints, and adhesives.

It has been realized that the properties of a material depend not only on its chemical composition but also on its dimension. Many materials exhibit different properties from their corresponding bulk properties when the dimensions of the system approach the molecular level. For example, metal and semi-conducting nanoclusters with dimensions of a few nanometers exhibit remarkable optical, electrical, mechanical, catalytic, and magnetic properties [1]. For polymers, the size-dependent effect is expected to appear at larger length scale as the dimensions of a single polymer chain can reach tens of nm or even larger depending on the molecular weight. Advances in nanotechnology have permitted the fabrication of materials, especially polymeric materials, with various submicrometer

structures [2-8]. These materials, having structures at least in one dimension in the range about a few hundred nm, are often called mesoscopic materials.

Polymer thin films with thicknesses below hundreds of nm are used extensively in technological applications such as protective or optical coatings, barrier layers, and packaging materials. The dramatically increased surface-to-volume ratio and the restriction on the chain conformation in the film thickness direction are believed to influence the mobility of the molecules and consequently lead to different viscoelastic properties of the thin film compared to the bulk [9]. Continuous theoretical and experimental efforts are being carried out in an attempt to achieve better understanding of the dynamics of macromolecules in confined environments [9]. Of great practical importance and therefore particular experimental interest is the reliable determination of the glass transition temperature (T_g) and the elastic moduli of polymer thin films as their performance depends highly on these material properties. Despite the facile experimental access to the T_g and mechanical properties of bulk polymers, this is prohibitive for thin films due to the low signal-to-noise ratio inherent to the small dimensions of the sample. Hence traditional methods for thermal and mechanical characterization can hardly be employed.

The first systematic study of the dependence of T_g on the thickness of thin polymer films was conducted by Keddie et al. [10] using ellipsometry. Since then, a number of techniques with high sensitivity including ellipsometry [11-13], dielectric spectroscopy [14,15], X-ray reflectivity [16], positron annihilation life time spectroscopy [17], Brillouin light scattering (BLS) [11,18], and local thermal analysis [19] have been applied to measure T_g of polymer thin films, either supported or free-standing. Following the seminal experiments by Forrest et al. [20], it is now widely perceived that the T_g of free-standing thin films (below 100 nm) is substantially lower than that of the bulk material. But for supported thin films, no reliable conclusion has been drawn about the magnitude of the shift of T_g on the film thickness and even the direction of the shift (positive or negative) is ambiguous since the results from different techniques have been contradictory [21,22]. The determination of mechanical properties of thin polymer films is a more arduous task. The state-of-the-art methods are based mainly on the mechanical deformation of the thin film [23], e.g. the substrate curvature test, the nanoindentation and the bulge test, or on the acoustic wave propagation within the film [23,24], e.g. impulsive stimulated thermal scattering and BLS. The wave propagation based methods show great promise because of their noncontact, nondestructive

characteristics, the virtue of requiring no special sample preparation procedures and the high reproducibility of the results. In addition, the measured quantity, usually the phase velocity of the acoustic wave, is sensitive to the change in the free-volume of polymer. Therefore in combination with a change in temperature, these methods have been directly used to determine T_g of thin polymer films.

To date, BLS is the only wave propagation based method that has been used to determine elastic properties of thin polymer films with thickness below 100 nm [18,25]. Briefly, this technique leverages the Doppler shift of the inelastic light scattered by thermally activated hypersonic (GHz) elastic waves in the matter. This frequency shift and the scattering geometry allow the determination of the phase velocity of the acoustic waves. In spite of few BLS studies on thin polymer films [11,18,24-26], ample space remains for further investigations. For example, the determination of T_g by BLS has so far been restricted to free-standing thin films [11,18]. Furthermore, the exploration of elastic excitations in some both theoretically and practically important systems, including the multilayer stack of alternating thin layers, is essentially lacking.

From a fundamental point of view, the study of acoustic wave propagation in inhomogeneous systems is itself of great importance. Since the late 1980s, it has been realized that fascinating material properties can be introduced by constructing composites with periodic structures. The pioneering work by Joannopoulos [27-32] and Yablonovitch [32-35] has shown that composite materials with specially designed periodic variation of dielectric constant, or photonic crystals, offer the possibility of complete control over light propagation. This powerful capability mainly originates from a distinct hallmark of photonic crystals, that is, the existence of photonic bandgaps, which prevent light with certain frequencies from propagating through the crystal in analogy to electronic bandgaps in semiconductors. Recalling the impact of semiconductors on the field of electronics, one can easily anticipate the revolution in optical, information and telecommunication industries by the development of photonic crystals. For example, future high-speed computers may be based on photonic crystal chips using light signals instead of electricity for data processing. Soon after the birth of this emerging field of the novel manipulation of light, theoretical work embarked on the propagation of acoustic waves in structures with periodic variations of density and/or sound velocities, these structures are coined phononic crystals [36] by analogy with their optical counterparts. A major effort is the search for phononic bandgaps

that forbid the propagation of acoustic waves within certain energy ranges. Phononic crystals could achieve the same level of control over acoustic waves as photonic crystals do on light and semiconductors on electrons. Therefore, promising technological applications in sonics, ultrasonics, and hypersonics are highly anticipated, including sound shields, acoustic superlenses, acoustic lasers, and thermal barriers [37-44].

In spite of the different physical nature of phononic and photonic crystals as well as semiconductors, the physical reason for the bandgap formation in these systems is essentially the same. In all cases, the bandgap is generated by the destructive interference of Bragg diffracted waves in periodic structures [45]. The bandgap formation phenomenon, however, becomes increasingly complex when the system varies from semiconductors to photonic crystals and then to phononic crystals in as much as the corresponding wave nature changes from scalar wave (electronic) to transverse wave (electromagnetic) and finally to full vector wave (acoustic). For phononic crystals, more material parameters are required to specify the system, which further complicates the nature of wave propagation. Two theoretical papers in 1993 by Kushwaha et al. [36] and Economou et al. [46] have been generally regarded to trigger the research on phononic crystals. Thereafter, an increasingly growing number of publications have been devoted to this newly-born field every year.

Most of the studies on phononic crystals are from a theoretical point of view and with a special emphasis on the band structure calculations for various lattice types and elastic combinations. The existence of bandgaps in various phononic crystals has been experimentally confirmed [40,42-44] and some derivative novel physical effects have also been observed, such as the tunneling effect [47] and negative refraction [48,49]. These experiments were mainly based on ultrasonic transmission techniques. All of the systems realized so far have been restricted to sonic and ultrasonic crystals with macroscopic periodicity, e.g. in the millimeter range patiently assembled manually [40,43,44]. The desire for further extending the investigation of this phononic bandgap formation phenomenon to even higher frequencies, entering the hypersonic range, largely comes from the distinct nature inherent to hypersonic waves and the consequent emergence of possible novel applications [37-39,41].

Unlike sonic and ultrasonic waves, whose generation usually relies on an external stimulus, acoustic waves at hypersonic frequencies (phonons) can be formed merely by

random thermal motion of the atoms of a material. In dielectric materials, thermal energy is mainly transported by phonons, therefore hypersonic phononic crystals capable of manipulating the flow of phonons are expected to have an impact on controlling the thermal conductivity. Furthermore, a hypersonic crystal permits concurrence of phononic and photonic bandgaps [37,38,41], making the integrated management of electromagnetic and elastic waves possible. This feature, unique to hypersonic crystals, allows the design of a number of novel acousto-optical devices [37,38,41], including optical modulators and optically pumped acoustic oscillators. The significance of hypersonic crystals calls for thorough experimental investigations, unfortunately the dual difficulties associated with the fabrication and characterization caused by the intrinsic small dimensions of the structure (submicrometer scale) pose serious obstacles.

From the introduction above, one can recognize that the study of elastic excitations in mesoscopic materials is of both practical and fundamental importance. The status quo is that compared to the knowledge on the electronic and optical properties, the understanding of the elastic properties of mesoscopic systems is much less satisfactory. The present dissertation therefore was carried out in an attempt to narrow this gap.

Chapter 2

Elastic wave propagation in solids

2.1 Elasticity fundamentals

2.1.1 Stress and strain

When a solid body²⁻¹ is deformed under the application of external forces, the arrangement of its molecules changes from the initial equilibrium state, internal forces therefore arise which tend to restore the body to equilibrium. These internal forces associated with deformation are called internal stresses.

Consider a closed volume V of the body, the total internal force on V can be represented by $\int_V \mathbf{F}dV$, where \mathbf{F} is the force per unit volume and $\mathbf{F}dV$ is the force on a volume element dV in V . With the aid of Gauss's divergence theorem, the volume forces can be related to the surface forces via the following relation

$$\int_V \mathbf{F}dV = \int_S \mathbf{n} \cdot \boldsymbol{\sigma}dS, \text{ with } \mathbf{F} = \nabla \cdot \boldsymbol{\sigma}, \quad (2.1)$$

where dS is a surface element of the surface S that encloses V , and \mathbf{n} is the unit normal characterizing the direction of dS whose positive direction is pointing outward of dS . Since \mathbf{F} is a vector, $\boldsymbol{\sigma}$ is then a second-rank tensor, which is called the stress tensor. Written in component form, we have

²⁻¹ The "solid" discussed in this chapter includes also liquid, the latter can be regarded as a special case of solid which cannot support shear stress, or equivalently, $\mu=0$, where μ is the Lamé coefficient whose meaning will be made clear in the following.

$$F_i = \frac{\partial \sigma_{ik}}{\partial x_k}, \quad (2.2)$$

where the Einstein summation convention is used. It can be readily shown that [50] the stress tensor is symmetrical, namely, $\sigma_{ik} = \sigma_{ki}$. Therefore there are only six independent components of stress, among which σ_{11} , σ_{22} and σ_{33} are called normal components of stress as they cause dilatation or contraction of the body; while σ_{12} , σ_{13} and σ_{23} are called shear components of stress as they lead to a change in the shape of the body.

The deformation of a solid body can be completely described if the displacement of every point of the body is known. Consider some particular point whose position vector before the deformation is \mathbf{r} , and after the deformation is \mathbf{r}' . The displacement of this point due to the deformation is denoted by the so-called displacement vector \mathbf{u} ,

$$\begin{aligned} \mathbf{u} &= \mathbf{r}' - \mathbf{r} \\ \text{or } u_i &= x'_i - x_i. \end{aligned} \quad (2.3)$$

Certainly u_i is a function of the coordinates x_i . When a body is deformed, the distances between its points change. Consider two closely spaced points. If the distance vector joining them before the deformation is dx_i , obviously the distance between them is given by $dl = \sqrt{dx_i^2}$. After the deformation, the distance vector joining the two points becomes $dx'_i = dx_i + du_i$, correspondingly the distance between them is $dl' = \sqrt{dx_i'^2}$.

Substituting $du_i = \frac{\partial u_i}{\partial x_k} dx_k$, we obtain

$$dl' = \sqrt{dl^2 + 2 \frac{\partial u_i}{\partial x_k} dx_i dx_k + \frac{\partial u_i}{\partial x_k} \frac{\partial u_i}{\partial x_l} dx_k dx_l}. \quad (2.4)$$

For small deformations as in the context of this thesis, the higher order terms in Eq. (2.4) can be ignored, therefore

$$dl' = \sqrt{dl^2 + 2 \frac{\partial u_i}{\partial x_k} dx_i dx_k}. \quad (2.5)$$

Defining a second-rank tensor u_{ik} as

$$u_{ik} = \frac{1}{2} \left(\frac{\partial u_i}{\partial x_k} + \frac{\partial u_k}{\partial x_i} \right), \quad (2.6)$$

Eq. (2.5) becomes
$$dl' = \sqrt{dl^2 + 2u_{ik} dx_i dx_k} . \quad (2.7)$$

The tensor u_{ik} is called the strain tensor. It is self-evident from its definition that the strain tensor is also a symmetrical tensor, that is, $u_{ik} = u_{ki}$.

2.1.2 Hook's law

For a perfectly elastic body, Hook's law can be generalized to state that each component of stress is linearly related to each component of strain, namely

$$\sigma_{ik} = c_{iklm} u_{lm}, \quad (2.8)$$

where c_{iklm} is a fourth-rank tensor called the elastic constant tensor or stiffness tensor. In the most general case, c_{iklm} has $3 \times 3 \times 3 \times 3 = 81$ components. Fortunately, by virtue of the symmetry of the stress and strain tensors (both of them have only six independent components), the number of the coefficients can be reduced to $6 \times 6 = 36$. It can be shown that further reduction is possible from energy considerations [50,51]. The number of independent elastic constants for the most general anisotropic body can be reduced to 21, as a result of the following symmetry relations,

$$c_{iklm} = c_{kilm} = c_{ikml} = c_{lmik} . \quad (2.9)$$

For solids with certain symmetries, e.g. crystals, the number of the elastic constants can be even reduced according to Voigt's principle [50,51] which states that the symmetry of the physical process is superimposed on the symmetry of the crystal. In practice it is customary to use the matrix notation in place of the full tensor notation to express the stress-strain relation in Eq. (2.8). The following rules are adopted:

Tensor notation	11	22	33	23, 32	13, 31	12, 21
Matrix notation	1	2	3	4	5	6

For example, the tensor component c_{1122} is replaced by the matrix index C_{12} , and so on. Accordingly Eq. (2.8) can be rewritten in the following equivalent matrix form,

$$\begin{bmatrix} \sigma_1 \\ \sigma_2 \\ \sigma_3 \\ \sigma_4 \\ \sigma_5 \\ \sigma_6 \end{bmatrix} = \begin{bmatrix} C_{11} & C_{12} & C_{13} & C_{14} & C_{15} & C_{16} \\ C_{21} & C_{22} & C_{23} & C_{24} & C_{25} & C_{26} \\ C_{31} & C_{32} & C_{33} & C_{34} & C_{35} & C_{36} \\ C_{41} & C_{42} & C_{43} & C_{44} & C_{45} & C_{46} \\ C_{51} & C_{52} & C_{53} & C_{54} & C_{55} & C_{56} \\ C_{61} & C_{62} & C_{63} & C_{64} & C_{65} & C_{66} \end{bmatrix} \begin{bmatrix} u_1 \\ u_2 \\ u_3 \\ u_4 \\ u_5 \\ u_6 \end{bmatrix}. \quad (2.10)$$

This symmetric 6×6 matrix $[C]$ is called the stiffness matrix. The general discussion of the specific matrix form corresponding to a given crystal symmetry can be found in specialized treatises. Here the result will be given only for the simplest case, the isotropic body, for which the physical properties do not depend on the orientation of the body. In many cases, especially when polymeric materials are concerned, the isotropic treatment serves as a very good approximation.

2.1.3 Elastic moduli of isotropic bodies

For an isotropic body, symmetry considerations show that the stiffness matrix in Eq. (2.10) has the following form

$$\begin{bmatrix} \sigma_1 \\ \sigma_2 \\ \sigma_3 \\ \sigma_4 \\ \sigma_5 \\ \sigma_6 \end{bmatrix} = \begin{bmatrix} C_{11} & C_{12} & C_{12} & 0 & 0 & 0 \\ C_{12} & C_{11} & C_{12} & 0 & 0 & 0 \\ C_{12} & C_{12} & C_{11} & 0 & 0 & 0 \\ 0 & 0 & 0 & C_{44} & 0 & 0 \\ 0 & 0 & 0 & 0 & C_{44} & 0 \\ 0 & 0 & 0 & 0 & 0 & C_{44} \end{bmatrix} \begin{bmatrix} u_1 \\ u_2 \\ u_3 \\ u_4 \\ u_5 \\ u_6 \end{bmatrix}. \quad (2.11)$$

In fact, there are only two independent elastic constants as the following relation holds

$$C_{11} = C_{12} + 2C_{44}. \quad (2.12)$$

Conventionally two elastic parameters, the so-called Lamé coefficients λ and μ , are often used to describe the elastic properties of an isotropic body. Their relation to the elastic constants is

$$\lambda = C_{12} \text{ and } \mu = C_{44}. \quad (2.13)$$

μ is also called shear modulus and sometimes is denoted by G . Some other elastic parameters are also often encountered, e.g., the bulk modulus, the Young's modulus and the Poisson's ratio.

The bulk modulus is defined as the ratio of the hydrostatic pressure ($p = -\sigma_{11} = -\sigma_{22} = -\sigma_{33}$) to the fractional volume change,

$$K \equiv -\frac{\delta p}{\delta u_{ii}} = \lambda + \frac{2}{3}\mu. \quad (2.14)$$

The Young's modulus is defined as the ratio of the longitudinal stress to the longitudinal strain,

$$E \equiv \frac{\sigma_{11}}{u_{11}} = \frac{\mu(3\lambda + 2\mu)}{\lambda + \mu}. \quad (2.15)$$

The ratio of the lateral strain to the longitudinal strain is called the Poisson's ratio,

$$\sigma \equiv -\frac{u_{22}}{u_{11}} = \frac{\lambda}{2(\lambda + \mu)}. \quad (2.16)$$

The use of σ to denote the Poisson's ratio and σ_{ik} (or σ_i in the matrix notation) to denote the components of the stress tensor cannot lead to ambiguity, since the latter always have suffixes.

2.2 Elastic waves in isotropic media

2.2.1 Longitudinal and transverse waves

The equation of motion for an elastic body can be obtained from the Newton's second law. Specifically, one has to equate the resultant force due to the internal stresses to the product of acceleration and mass per unit volume. By referring to Eq. (2.2), we have

$$\frac{\partial \sigma_{ik}}{\partial x_k} = \rho \frac{\partial^2 u_i}{\partial t^2}, \quad (2.17)$$

where ρ is the density and u_i is the displacement vector. For an infinite homogeneous and isotropic medium, after applying Hook's law and adopting the Lamé coefficients representation, the equation of motion is found to have the following form:

$$(\lambda + 2\mu)\nabla(\nabla \cdot \mathbf{u}) - \mu\nabla \times (\nabla \times \mathbf{u}) - \rho\partial_t^2 \mathbf{u} = 0. \quad (2.18)$$

In the case of a harmonic elastic wave of angular frequency ω , the displacement vector \mathbf{u} can be written as

$$\mathbf{u}(\mathbf{r}, t) = \text{Re} \left[\mathbf{u}(\mathbf{r}) e^{-i\omega t} \right], \quad (2.19)$$

and Eq. (2.18) can be reduced to the following time-independent form:

$$(\lambda + 2\mu)\nabla(\nabla \cdot \mathbf{u}) - \mu\nabla \times (\nabla \times \mathbf{u}) + \rho\omega^2 \mathbf{u} = 0. \quad (2.20)$$

Mathematically we can express \mathbf{u} as the sum of two vectors $\mathbf{u} = \mathbf{u}_l + \mathbf{u}_t$ such that

$$\nabla \times \mathbf{u}_l = 0 \text{ and } \nabla \cdot \mathbf{u}_t = 0. \quad (2.21)$$

Eq. (2.20) can then be decomposed into two independent Helmholtz equations of motion:

$$(\nabla^2 + k_l^2)\mathbf{u}_l = 0 \quad (2.22)$$

$$\text{and } (\nabla^2 + k_t^2)\mathbf{u}_t = 0, \quad (2.23)$$

where $k_l = \omega_l/c_l$ and $k_t = \omega_t/c_t$ are the wavenumbers of the longitudinal and transverse waves, respectively. The solutions of these two equations represent two elastic waves which propagate independently: the longitudinal wave with a phase velocity $c_l = \sqrt{C_{11}/\rho} = \sqrt{(\lambda + 2\mu)/\rho}$, also called the longitudinal sound velocity; and the transverse or shear wave with a phase velocity $c_t = \sqrt{C_{44}/\rho} = \sqrt{\mu/\rho}$, also called the transverse or shear sound velocity.

For the longitudinal wave the particle displacement is in the direction of wave propagation, while for the transverse wave the particle displacement is perpendicular to the direction of propagation. It is easy to recognize that the transverse wave has two possible polarizations which are orthogonal to each other. Note also that the longitudinal wave involves changes in the volume of the medium, i.e. dilatation or compression of a local volume element. On the other hand, the transverse wave causes no volume change.

2.2.2 Spherical-wave solutions

Elastic wave propagation in an isotropic medium usually serves as the start point for studying more complicated systems, e.g. composite materials having two or more components. In the present thesis, composite elastic media with many spherical inclusions will be examined. To theoretically explore elastic wave propagation in such systems, a feasible and usually adopted approach [52-54] is to consider the scattering of a plane-wave by these spherical inclusions. In this instance, the use of a Cartesian coordinate system will meet many difficulties in the treatment of the equation of motion. The choice of a spherical coordinate system, however, could simplify much the computation.

In the following, we briefly introduce the spherical-wave solutions of the elastic wave equation for an isotropic medium. In a spherical coordinate system, the displacement vector \mathbf{u} can be written as the sum of three vectors $\mathbf{u} = \mathbf{l} + \mathbf{m} + \mathbf{n}$ such that Eq. (2.20) can be broken into three independent vector Helmholtz equations [55] as the following:

$$(\nabla^2 + k_l^2)\mathbf{l} = 0, \quad (\nabla^2 + k_t^2)\mathbf{m} = 0, \quad (\nabla^2 + k_t^2)\mathbf{n} = 0. \quad (2.24)$$

Evidently, \mathbf{l} represents the displacement associated with the longitudinal wave and \mathbf{m} and \mathbf{n} represent the transverse displacements which are orthogonal to each other. The longitudinal

component of the solution, \mathbf{l} , can be written as the gradient of a scalar function, φ , which is the solution of a scalar Helmholtz equation $(\nabla^2 + k_t^2)\varphi = 0$:

$$\mathbf{l} = \frac{1}{k_t} \nabla \varphi. \quad (2.25)$$

The transverse displacement vectors \mathbf{m} and \mathbf{n} can be expressed as the curl and the curl curl of a vector function. The vector function can be constructed from the product of a constant vector and a scalar potential function which satisfies the scalar Helmholtz equations $(\nabla^2 + k_t^2)\psi = 0$ and $(\nabla^2 + k_t^2)\chi = 0$ for \mathbf{m} and \mathbf{n} respectively. For spherical coordinates, in place of the constant vector, the position vector \mathbf{r} can be used, and \mathbf{m} and \mathbf{n} remain independent of \mathbf{l} . Then one can write

$$\mathbf{m} = \nabla \times \mathbf{r} \psi, \quad (2.26)$$

$$\mathbf{n} = \frac{1}{k_t} \nabla \times \nabla \times \mathbf{r} \chi. \quad (2.27)$$

The solution of the scalar Helmholtz equation in a spherical coordinate system is well known and has the form:

$$f_{lm}(r, \theta, \phi) = R_l(kr) Y_{lm}(\theta, \phi). \quad (2.28)$$

$Y_{lm}(\theta, \phi)$ are the so-called spherical harmonics, with $l=0, 1, 2, 3, \dots$, and m running over all integer values from $-l$ to l . The radial functions, $R_l(kr)$, are the appropriate Bessel functions. For each l there are two linearly independent Bessel functions, j_l and n_l . The function n_l diverges [56] at $r=0$ and therefore it is excluded in a region which contains the origin. The function $h_l = j_l + in_l$ describes an outgoing spherical wave and consequently it is this linear combination of j_l and n_l which should be used in the case of a scattered wave.

The basic vector solutions of Eq. (2.24) in a spherical coordinate system, \mathbf{l}_{lm} , \mathbf{m}_{lm} and \mathbf{n}_{lm} , can then be derived from the solution of the scalar Helmholtz equation. The result is as follows:

$$\mathbf{l}_{lm}(R, k_l) = \frac{1}{k} \nabla [R_l(k_l r) Y_{lm}(\hat{r})], \quad l=0, 1, 2, 3, \dots \quad (2.29)$$

$$\mathbf{m}_{lm}(R, k_l) = \nabla \times [\mathbf{r} R_l(k_l r) Y_{lm}(\hat{r})], \quad l=1, 2, 3, \dots \quad (2.30)$$

$$\mathbf{n}_{lm}(R, k_l) = \frac{1}{k_l} \nabla \times \nabla \times [\mathbf{r} R_l(k_l r) Y_{lm}(\hat{r})], \quad l=1, 2, 3, \dots \quad (2.31)$$

Note that monopole ($l=0$) waves can exist only as longitudinal solutions.

2.3 Elastic waves in supported thin layers

In the preceding discussion of the elastic wave propagation in an isotropic body, it was assumed that the body is infinitely large so that the boundary effect can be ignored. Practically, an elastic body is always finite. If its surface is concerned or if its size is very small compared to the wavelength of the elastic wave, the existence of the boundaries will have a substantial influence on the wave propagation and hence cannot be neglected. Regarding the boundary effects, an important case of much theoretical and practical interest is wave propagation in supported thin layers. This section will give a brief introduction to this subject.

Considering the following system consisting of a substrate and a thin layer on top as shown in **Fig. 2.1**, both the substrate and the layer are infinite in the directions parallel to their interface and are treated as isotropic. The coordinate system to be used for the discussion is also illustrated. It can be seen that the $x_3=0$ plane is the interface between the layer and the substrate while the plane $x_3=h$ is the free surface of the layer. To study elastic waves in the thin supported layer, the wave equation (2.18) is still workable and has to be applied to both the layer and the substrate. The major difference now is that the mechanical boundary conditions must be taken into account. More explicitly, the continuity of the stress and the strain at the interface ($x_3=0$) and the vanishing of the stress at the free surface ($x_3=h$) must be satisfied, which leads to much more complicated wave propagation compared to the bulk.

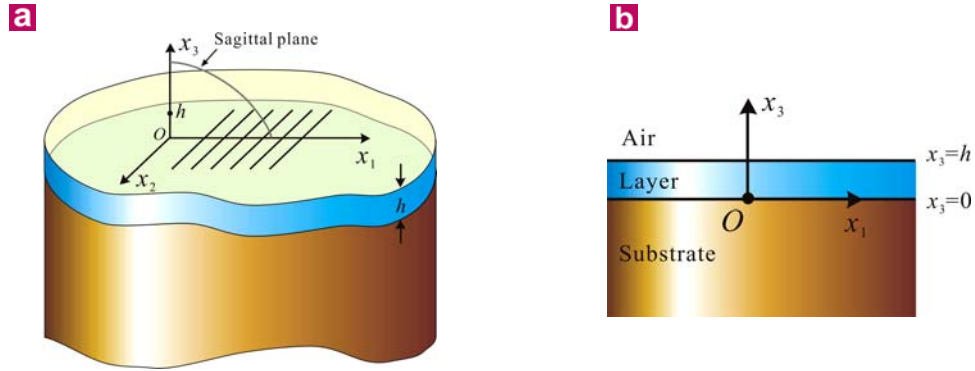


Figure 2.1 Coordinate system for elastic wave propagation in thin layers. **a**, Propagation direction and sagittal plane. **b**, Sagittal plane coordinates.

It is easily appreciated from symmetry considerations that the waves of interest will be “straight crested” in the sense that there are no variations of any of the displacement components in a direction parallel to the free surface and perpendicular to the direction of propagation. The direction of propagation will be taken as the x_1 direction in **Fig. 2.1**, thus the disturbance has constant phase and amplitude for each component along any line parallel to the x_2 axis. However, the nature of the waves will be such that they decay with depth into the substrate and in general become of negligible amplitude a few wavelengths below the interface. In fact, this nature is in accordance with the assumption that the waves of interest are surface or film excitations. Therefore one is seeking for straight-crested propagating waves of the following form:

$$u_j = \alpha_j \exp(ikbx_3) \exp[ik(x_1 - vt)]. \quad (2.32)$$

It will be seen below that b is in general complex and it gives, in this interpretation, the variation with depth of the amplitude and phase of the partial waves measured on a “plane of constant phase”, namely, a plane perpendicular to x_1 . The α_j ($j=1, 2, 3$) give the relative amplitudes of the different components of each partial wave.

Substituting Eq. (2.32) into Eq. (2.18) results in the following relation between v , b and α in the isotropic substrate considered:

$$\begin{bmatrix} \Gamma_{11} - \rho v^2 & \Gamma_{12} & \Gamma_{13} \\ \Gamma_{12} & \Gamma_{22} - \rho v^2 & \Gamma_{23} \\ \Gamma_{13} & \Gamma_{23} & \Gamma_{33} - \rho v^2 \end{bmatrix} \begin{bmatrix} \alpha_1 \\ \alpha_2 \\ \alpha_3 \end{bmatrix} = 0 \quad (2.33)$$

where

$$\begin{aligned} \Gamma_{11} &= c_{44}b^2 + c_{11} & \Gamma_{12} &= 0 & \Gamma_{13} &= (c_{11} - c_{44})b \\ \Gamma_{22} &= c_{44}(1 + b^2) & \Gamma_{23} &= 0 & \Gamma_{33} &= c_{11}b^2 + c_{44} \end{aligned}$$

In order to have nontrivial solutions, the determinant of the square matrix in Eq. (2.33) must be set equal to zero, which produces the secular equation of the form:

$$|\Gamma_{rs} - \delta_{rs}\rho v^2| = 0 \quad r, s, = 1, 2, 3. \quad (2.34)$$

An important point to note in Eq. (2.33) is that the sagittal-plane displacements, α_1 and α_3 of Eq. (2.32), are completely uncoupled in the equations of motion from the transverse displacements, α_2 . Thus, Eq. (2.34) separates into two equations

$$(c_{44}b^2 + c_{44} - \rho v^2)(c_{11}b^2 + c_{11} - \rho v^2) = 0$$

and

$$c_{44}b^2 + c_{44} - \rho v^2 = 0, \quad (2.35)$$

which can be regarded as algebraic equations in b for an assumed value of v .

Similar equation as Eq. (2.33) can be found for the displacement components in the isotropic layer, involving layer material parameters referred to the same axes. In the final solution, all the partial waves (Eq. (2.32)) in the substrate and layer will have the same phase velocity. The roots and corresponding eigenvectors for the two media are

I. for transverse motion in the substrate

$$b^{(a)} = -i[1 - (v/v_t)^2]^{1/2} \quad \alpha^{(a)} = [0, 1, 0] \quad (2.36)$$

II. for transverse motion in the layer

$$\begin{aligned} b^{(1)} &= +i[1 - (v/\hat{v}_t)^2]^{1/2} & \alpha^{(1)} &= [0, 1, 0] \\ b^{(2)} &= -i[1 - (v/\hat{v}_t)^2]^{1/2} & \alpha^{(2)} &= [0, 1, 0] \end{aligned} \quad (2.37)$$

III. for sagittal motion in the layer

$$\begin{aligned}
 b^{(5)} &= +i[1 - (v/\hat{v}_t)^2]^{1/2} & \alpha^{(5)} &= [-b^{(5)}, 0, 1] \\
 b^{(6)} &= +i[1 - (v/\hat{v}_t)^2]^{1/2} & \alpha^{(6)} &= [1, 0, b^{(6)}] \\
 b^{(7)} &= -i[1 - (v/\hat{v}_t)^2]^{1/2} & \alpha^{(7)} &= [-b^{(7)}, 0, 1] \\
 b^{(8)} &= -i[1 - (v/\hat{v}_t)^2]^{1/2} & \alpha^{(8)} &= [1, 0, b^{(8)}]
 \end{aligned} \tag{2.38}$$

IV. for sagittal motion in the substrate

$$\begin{aligned}
 b^{(c)} &= -i[1 - (v/v_t)^2]^{1/2} & \alpha^{(c)} &= [-b^{(c)}, 0, 1] \\
 b^{(d)} &= -i[1 - (v/v_t)^2]^{1/2} & \alpha^{(d)} &= [1, 0, b^{(d)}]
 \end{aligned} \tag{2.39}$$

where $v_t = (c_{44}/\rho)^{1/2}$ and $\hat{v}_t = (\hat{c}_{44}/\hat{\rho})^{1/2}$ are the transverse sound velocities for bulk waves in the substrate and the layer, respectively, while $v_l = (c_{11}/\rho)^{1/2}$ and $\hat{v}_l = (\hat{c}_{11}/\hat{\rho})^{1/2}$ are the corresponding bulk longitudinal sound velocities. Notice that for the substrate only values of b lying in the lower half of the complex plane are retained, as the solutions desired (Eq. (2.32)) are to represent surface waves.

Under the isotropic assumption, it can be easily shown that [57] the boundary-condition equations also separate into two uncoupled sets, one set involving roots a , 1 and 2 and hence the in-plane (x_1 - x_2 plane) displacement components only, and the second set involving the roots 5, 6, 7, 8, c , and d and thereby sagittal-plane displacements only. Thus for the isotropic case, the final solutions for elastic wave propagation in supported thin layers are divided into two categories:

- I. *Love modes*
- II. *Lamb modes*

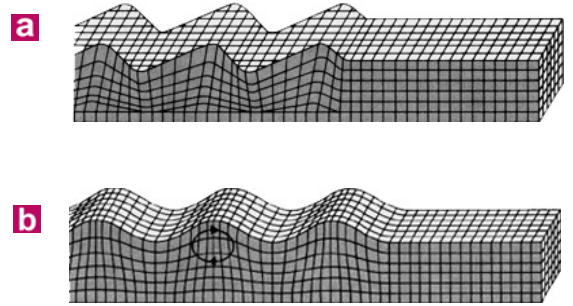


Figure 2.2 Schematic show of the displacements of the two uncoupled surface modes. **a**, *Love modes*. **b**, *Lamb modes*.

Love modes have only in-plane displacements, in contrast, only sagittal-plane displacements are involved in Lamb modes. Their displacements are schematically depicted in **Fig. 2.2a** and **b**, respectively. It is seen that only Lamb modes can cause interface or surface

corrugation, which is important for the determination of Lamb modes on an opaque substrate by light scattering techniques [58].

The following discussion will be restricted to Lamb modes, since it is the Lamb modes that have been probed in this work. In addition, experimental investigations on waves in thin layers are almost exclusively focused on Lamb modes. Mechanical boundary conditions for the sagittal-plane displacements lead to the following equation:

$$\begin{bmatrix} b^{(5)} & -1 & -b^{(5)} & -1 & -b^{(c)} & 1 \\ -1 & -b^{(6)} & -1 & b^{(6)} & 1 & b^{(d)} \\ 1-b^{(5)2} & 2b^{(6)} & 1-b^{(5)2} & -2b^{(6)} & -r(1-b^{(c)2}) & -2rb^{(d)} \\ 2b^{(5)} & -(1-b^{(5)2}) & -2b^{(5)} & -(1-b^{(5)2}) & -2rb^{(c)} & r(1-b^{(c)2}) \\ (1-b^{(5)2})\exp(ikb^{(5)}h) & 2b^{(6)}\exp(ikb^{(6)}h) & (1-b^{(5)2})\exp(-ikb^{(5)}h) & -2b^{(6)}\exp(-ikb^{(6)}h) & 0 & 0 \\ 2b^{(5)}\exp(ikb^{(5)}h) & -(1-b^{(5)2})\exp(ikb^{(6)}h) & -2b^{(5)}\exp(-ikb^{(5)}h) & -(1-b^{(5)2})\exp(-ikb^{(6)}h) & 0 & 0 \end{bmatrix} \begin{bmatrix} C_5 \\ C_6 \\ C_7 \\ C_8 \\ C_c \\ C_d \end{bmatrix} = 0$$

where $r = c_{44}/\hat{c}_{44}$

(2.40)

Given that the material properties of both the substrate and the layer are known, from Eq. (2.36) to Eq. (2.39) we easily see that b is only a function of v , the phase velocity of the surface wave. Substituting Eq. (2.38) and Eq. (2.39) into Eq. (2.40) and equating the determinant of the square matrix to zero, one actually defines an implicit function, v , which is a function of kh , the product of the wavenumber of the surface wave and the film thickness. This relation $v=v(kh)$, is often referred to as the dispersion relation. Unfortunately, there is no simple analytical solution to Eq. (2.40) and numerical calculations are necessary to determine the propagation velocity v . In general, the solution to Eq. (2.40) can be rather complicated, which highly depends on the elastic combination of the two relevant media, the substrate and the layer. A complete discussion of all possible cases is far beyond the scope of this chapter, only some most common situations will be checked below.

First, a special case will be considered, that is, the substrate has a free surface, or equivalently, the layer thickness $h=0$. In this instance, kh is always zero. By referring to Eq. (2.40) it can be easily seen that all the exponential terms in the square matrix will vanish and be replaced by 1. Consequently, the solution v for a given set of elastic parameters of the substrate is a constant, which represents a non-dispersive mode, the so-called Rayleigh mode. Love modes at this time degenerate into the horizontally polarized bulk shear waves propagating parallel to the substrate surface. The velocity of the Rayleigh wave is somewhat

less than the bulk transverse velocity v_t , and ranges from $0.874v_t$ to $0.955v_t$, corresponding to a variation of the Poisson's ratio σ from 0 to 0.5.

With the presence of a layer on top of the substrate surface, $h \neq 0$, and the phase velocities then become kh dependent. We consider two cases:

- I. *Layer stiffens the substrate*²⁻² ($\hat{v}_t > v_t$)
- II. *Layer loads the substrate* ($\hat{v}_t < v_t$)

When $\hat{v}_t > v_t$, the layer is said to “stiffen” the substrate because the presence of the layer increases the surface wave velocity above that of the Rayleigh velocity of the substrate, whereas when $\hat{v}_t < v_t$, the layer is said to “load” the substrate because the velocity of the free-surface Rayleigh mode on the substrate is decreased by the presence of the layer.

For the stiffening situation, it is characteristic for the dispersion curve ($v \sim kh$) to start from $kh=0$ at the substrate Rayleigh velocity and increase until the substrate shear velocity is reached at a particular value of kh ; for larger values of kh this mode of propagation does not exist. For the material combination of this type, only one Lamb mode can propagate and that only for a limited range of kh . Since the minimum velocity of this mode is the substrate Rayleigh velocity and the maximum is the substrate shear velocity, the phase velocity does not cover a wide range. An example of the dispersion curve of this type is given in **Fig. 2.3a** for a silicon layer on a ZnO substrate.

When the layer loads the substrate, a significant feature is the existence of an unlimited number of higher order Lamb modes, sometimes also called Sezawa modes [57]. In this case, the dispersion curve for the first Lamb mode, often referred to simply as Rayleigh mode, starts with negative slope at the Rayleigh velocity of the substrate, for $kh=0$. As kh increases, the phase velocity continues to decrease and for layer thickness large compared to the wavelength, $kh \gg 1$, it tends asymptotically to the Rayleigh velocity of a free surface of the layer material. The higher order Lamb modes all have a low frequency cutoff²⁻³ at which

²⁻² More strictly speaking, the “stiffening” (or “loading”) behavior refers to the case that there is substantial difference between the shear moduli of the layer and the substrate, i.e. $\hat{v}_t > \sqrt{2}v_t$ (or $\hat{v}_t < \sqrt{2}v_t$).

²⁻³ The appearance of this cutoff frequency is due to the restriction imposed by our definition of a surface wave, which has to decay into the substrate. If the velocity exceeds the substrate shear wave velocity, the corresponding wave will radiate into the substrate, representing a leaky wave. We will see in Chapter 5 that these leaky waves have been experimentally probed.

the phase velocity is equal to the substrate shear velocity. Their phase velocities also decrease with increasing kh and have a high frequency asymptote at the layer shear velocity. An example of the dispersion relation of this type of material combination is given in **Fig. 2.3b** for a ZnO layer on a silicon substrate, the reverse case of **Fig. 2.3a**.

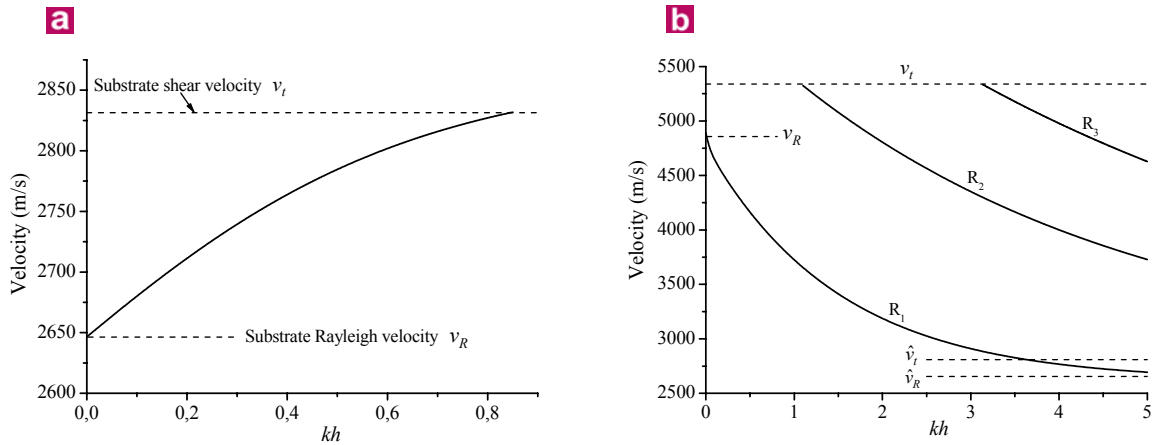


Figure 2.3 Examples of the dispersion relation for Lamb modes. a, *Silicon layer on ZnO substrate, the stiffening case. ZnO: $v_l=6000$ m/s, $v_t=2831$ m/s, $v_R=2649$ m/s; silicon: $v_l=8945$ m/s, $v_t=5341$ m/s, $v_R=4890$ m/s. b, *ZnO layer on silicon substrate, the loading case. Only the first three Lamb modes (R_1 , R_2 and R_3) are shown. (see Ref.[57])**

In addition to the above mentioned well-known surface and film excitations, in the past 20 years or so, people found that there exists another kind of elastic excitations on the surface which is mainly longitudinally polarized, the so-called longitudinal guided mode [59,60]. It can be regarded as the longitudinal counterpart of the Rayleigh mode, and has a phase velocity slightly below the bulk longitudinal velocity. Since this mode radiates usually quite strongly into transverse substrate waves, it is quasi-localized, i.e. leaky. The longitudinal guided mode is not often observed experimentally, especially for a free surface or a very thin layer (in a sense kh is small), and further discussion of it will be omitted.

2.4 Vibrations of an elastic sphere

2.4.1 Vibration eigenmodes

In the preceding section, the modification of elastic wave propagation due to the presence of one-dimensional confinement has been studied. In this section, another important confinement effect, elastic excitations in a sphere, will be considered. The restriction imposed by the three-dimensional spherical boundary makes the description of the elastic excitations in such a sphere in terms of traveling waves no longer valid.

In this case, the sphere of finite size actually forms an elastic resonator that sustains elastic standing waves, and hence it “vibrates”. These elastic standing waves are usually called vibration eigenmodes. The free vibrations of an isotropic elastic sphere under stress-free boundary condition have been studied more than a century ago by Lamb [61]. Two types of modes are found: the torsional modes and the spheroidal modes. The torsional modes involve only shear motions and do not change the volume of the sphere, whereas the spheroidal modes involve both shear and stretching motions and produce radial displacements. Both the torsional and spheroidal modes are specified by two indices in analogy to the atomic orbitals: an angular momentum l ($=0, 1, 2, \dots$) and a branch number n ($=1, 2, 3, \dots$).

In the following, the computation of the vibration eigenmodes will be briefly described. Instead of just treating an elastic sphere with a stress-free boundary, a more general situation is considered, in which the sphere is embedded in an infinite homogeneous medium. It should be pointed out at this stage that strictly speaking one can only talk about eigenmodes when the sphere has a stress-free boundary. When the sphere is embedded in an elastic medium, the eigenmodes are coupled to the acoustic waves propagating through the surrounding medium, consequently energy leakage will happen, e.g. from the sphere to the surrounding medium. If the energy leakage is serious, the particle character will become diminished and finally disappear in case the particle has exactly the same density and elastic parameters as the surrounding medium. On the other hand, if the coupling between the eigenmodes and the acoustic waves is weak, the energy will be highly concentrated within the sphere. In this instance the presence of the surrounding medium has insignificant impact on the sphere vibration eigenmodes.

Assume the sphere of radius r_s has a density ρ_i and is made of a material with the longitudinal and transverse sound velocities c_{li} and c_{ti} respectively. The elastic parameters of the surrounding medium are correspondingly given by ρ_o , c_{lo} and c_{to} . The field inside the sphere, \mathbf{u}^{in} , can be expanded as a linear combination of spherical waves \mathbf{l}_{lm} , \mathbf{m}_{lm} and \mathbf{n}_{lm} , as discussed in Section 2.2.2,

$$\mathbf{u}^{in}(\mathbf{r}) = \sum_{lm} \{A_{lm} \mathbf{l}_{lm}(j, k_{li}) + B_{lm} \mathbf{m}_{lm}(j, k_{ti}) + C_{lm} \mathbf{n}_{lm}(j, k_{ti})\}, \quad (2.41)$$

where $k_{li} = \omega / c_{li}$ and $k_{ti} = \omega / c_{ti}$ are the wavenumbers used in the Bessel functions $j(k_{li}r)$ and $j(k_{ti}r)$. In a similar way, the field outside can be written as,

$$\mathbf{u}^{out}(\mathbf{r}) = \sum_{lm} \{D_{lm} \mathbf{l}_{lm}(h, k_{lo}) + E_{lm} \mathbf{m}_{lm}(h, k_{to}) + F_{lm} \mathbf{n}_{lm}(h, k_{to})\}, \quad (2.42)$$

where $k_{lo} = \omega / c_{lo}$ and $k_{to} = \omega / c_{to}$ are the wavenumbers used in the Bessel functions $h(k_{li}r)$ and $h(k_{ti}r)$. These Bessel functions were chosen so that the field is appropriately defined everywhere, i.e., it is finite in the origin of the sphere and outgoing outside the sphere.

The two fields defined above must satisfy boundary conditions (the continuity of the stress and strain across the boundary) at the surface of the sphere, i.e. at $r = r_s$,

$$\mathbf{u}^{in} \Big|_{r=r_s} = \mathbf{u}^{out} \Big|_{r=r_s}, \quad (2.43)$$

$$\mathbf{P}^{in} \Big|_{r=r_s} = \mathbf{P}^{out} \Big|_{r=r_s}, \quad (2.44)$$

where $p_i = \sigma_{ik} n_k$ is the force per unit area of the surface of the sphere with \mathbf{n} being the outgoing unit vector normal to the surface. Each of the above equations is equivalent to three scalar equations. Thus, the boundary conditions form a system of six homogeneous equations with an infinite number of unknowns. Using the orthonormality over the spherical surface of the spherical harmonics Y_{lm} , after a few calculations, one can decompose each of these equations into an infinite number of equations, one for each l . Due to the fact that the coefficients in these equations are not functions of m , the unknowns will depend only on l and we can re-denote them as: A_l , B_l , C_l , D_l , E_l and F_l . Therefore, for each l there are six homogeneous equations with six unknowns. Because of the orthogonality of the vector

spherical harmonic \mathbf{m}_{lm} to \mathbf{l}_{lm} and \mathbf{n}_{lm} , the system of six equations can be broken into two smaller systems: one of two equations involving only the coefficients B_l and E_l of the basic vector \mathbf{m}_{lm} , and one of four equations containing only the rest four coefficients corresponding to \mathbf{l}_{lm} and \mathbf{n}_{lm} . These two systems admit nontrivial solutions if and only if their determinants are zero. For each l , the condition that the determinant is zero is satisfied only by a discrete set of modes of frequencies ω_l^n , where n is the branch number. The solutions of the two systems lead to the previously mentioned two types of modes: the torsional modes (involve only \mathbf{m}_{lm}) and the spheroidal modes (involve only \mathbf{l}_{lm} and \mathbf{n}_{lm}).

2.4.2 Single sphere scattering

In this section, we consider the scattering of a plane sound wave propagating in a host material by a single elastic sphere. During this process, resonances may occur at certain frequencies of the incident wave and strong resonances will appear at frequencies close to the eigenfrequencies of the sphere vibrations. If the elastic mismatch between the sphere and the surrounding medium is sufficiently large, the eigenmodes are well-localized within the sphere and the strong resonances can be found as sharp peaks in the plot of scattering cross section versus frequency. When the elastic contrast is not remarkable, the resonances do not manifest themselves as sharp peaks. Instead, they are considerably broadened due to energy leakage and the peak frequencies also exhibit noticeable shift from the eigenfrequencies of a free-boundary sphere.

The significance of study of the single sphere sound scattering lies not just in the fact that it offers an alternative way to compute the eigenfrequencies of an elastic sphere. More importantly it could provide deeper insights into the physics of wave propagation in elastic composites with many spherical inclusions — a practically often encountered situation. For instance, if the coupling between the acoustic wave and the eigenmodes is weak, the information given by the single sphere scattering is enough to describe the corresponding collective modes of the composite. In this case, these modes propagate by coherently hopping from one scatterer to another, in analogy to electronic propagation in solids by a linear combination of atomic orbitals (LCAO) with the eigenmodes being the analogues of atomic orbitals. It has been pointed out by Economou et al. [62] that the single sphere

scattering cross section can be connected with the appearance of acoustic bandgaps in such composites induced by multiple phonon scattering. Moreover, the calculation of the scattering cross section by a single sphere constitutes the basis for a more complicated multiple scattering method for the study of more complex modes.

When the incident wave impinges onto the sphere, in general there are subsequently three separate waves: one is the unimpeded incident wave, \mathbf{u}^{inc} ; the second is the wave scattered by the sphere, \mathbf{u}^{sc} ; and the third is the wave excited inside the sphere, \mathbf{u}^{in} . The following calculations are based on the determination of \mathbf{u}^{sc} and \mathbf{u}^{in} . As in the case of the calculation of the sphere eigenmodes, we expand all these waves into vector spherical harmonics, \mathbf{l}_{lm} , \mathbf{m}_{lm} and \mathbf{n}_{lm} ,

$$\mathbf{u}^{inc}(\mathbf{r}) = \sum_{lm} \left\{ \alpha_{lm}^1 \mathbf{l}_{lm}(j, k_{lo}) + \alpha_{lm}^2 \mathbf{m}_{lm}(j, k_{lo}) + \alpha_{lm}^3 \mathbf{n}_{lm}(j, k_{lo}) \right\}, \quad (2.45)$$

$$\mathbf{u}^{in}(\mathbf{r}) = \sum_{lm} \left\{ \beta_{lm}^1 \mathbf{l}_{lm}(j, k_{li}) + \beta_{lm}^2 \mathbf{m}_{lm}(j, k_{li}) + \beta_{lm}^3 \mathbf{n}_{lm}(j, k_{li}) \right\}, \quad (2.46)$$

$$\mathbf{u}^{sc}(\mathbf{r}) = \sum_{lm} \left\{ \gamma_{lm}^1 \mathbf{l}_{lm}(h, k_{lo}) + \gamma_{lm}^2 \mathbf{m}_{lm}(h, k_{lo}) + \gamma_{lm}^3 \mathbf{n}_{lm}(h, k_{lo}) \right\}. \quad (2.47)$$

The coefficients α_{lm}^i are supposed to be known for a given incident wave, while the coefficients β_{lm}^i and γ_{lm}^i are calculated by applying the boundary conditions at the surface of the sphere. The boundary conditions are similar to Eq. (2.43) and (2.44). In this case the displacement vector outside the sphere consists of two contributions: the incident wave and the scattered wave. We have

$$\mathbf{u}^{in} \Big|_{r=r_s} = \mathbf{u}^{inc} \Big|_{r=r_s} + \mathbf{u}^{sc} \Big|_{r=r_s}, \quad (2.48)$$

$$\mathbf{P}^{in} \Big|_{r=r_s} = \mathbf{P}^{inc} \Big|_{r=r_s} + \mathbf{P}^{sc} \Big|_{r=r_s}. \quad (2.49)$$

Similar as before, the above equations can be decomposed into six scalar equations which can be easily separated (each of them) into an infinite number of equations, one for each lm combination. Then for each lm there is a system of six equations with the unknowns β_{lm}^i and γ_{lm}^i ($i=1, 2, 3$), therefore β_{lm}^i and γ_{lm}^i can be uniquely determined.

The scattering cross section is defined as the ratio of the scattered energy flux to the incident energy flux per unit surface, in the far field. Suppose that the sphere is placed at the origin of the coordinate system and the incident wave travels along the z axis, the above definition can be mathematically expressed as:

$$\sigma = \frac{\langle J_r^{sc} \rangle r^2 d\Omega}{\langle J_z^{inc} \rangle}, \text{ for } r \rightarrow \infty \quad (2.50)$$

where J_i is the energy flux per unit area defined broadly in terms of the complex fields,

$$J_i = \sigma_{ij} \frac{\partial u_j}{\partial t}, \quad (2.51)$$

and the symbol “ $\langle \rangle$ ” denotes the time average. Assume the time-dependent field is of the form $e^{-i\omega t}$, the time-averaged energy flux per unit area is transformed into:

$$\langle J_i \rangle = -\frac{1}{2} \omega \text{Im}(\sigma_{ij}^* u_j), \quad (2.52)$$

where “ Im ” and “ $*$ ” represent the imaginary part and the complex conjugate of a complex quantity, respectively. By using the corresponding expressions for σ_{ij} and u_j in Eq. (2.52) and then inserting it into Eq. (2.50), the dimensionless scattering cross section is finally given by

$$\hat{\sigma} = \frac{\sigma}{\pi r_s^2} = \frac{\sum_{l,m} \left[c_{l_o} \frac{|\gamma_{rm}^1|^2}{Z_{l_o}^2} + c_{t_o} l(l+1) \frac{|\gamma_{rm}^2|^2 + |\gamma_{rm}^3|^2}{Z_{l_o}^2} \right]}{\pi(c_{l_o} + c_{t_o})} = \sum_{l=0}^{\infty} \hat{\sigma}_l. \quad (2.53)$$

Here $Z_{l_o} = k_{l_o} r_s$, $Z_{t_o} = k_{t_o} r_s$ and $\hat{\sigma}$ is the dimensionless partial cross section due to the contribution of the l^{th} spherical wave; c_{l_o} and c_{t_o} are the previously defined longitudinal and transverse wave velocities in the surrounding medium; γ_{lm}^1 , γ_{lm}^2 and γ_{lm}^3 are the coefficients in Eq. (2.47).

Figure 2.4 shows an example of how the scattering cross section varies with the frequency of the incident sound wave for a silica sphere embedded in a cyclohexane/decalin solvent. The sharp, well-separated peaks correspond to diverse l -resonances, which are

obtained by subtracting from the scattering amplitude of the silica sphere the scattering amplitude of a rigid (incompressible) sphere of the same size for better visualization [63].

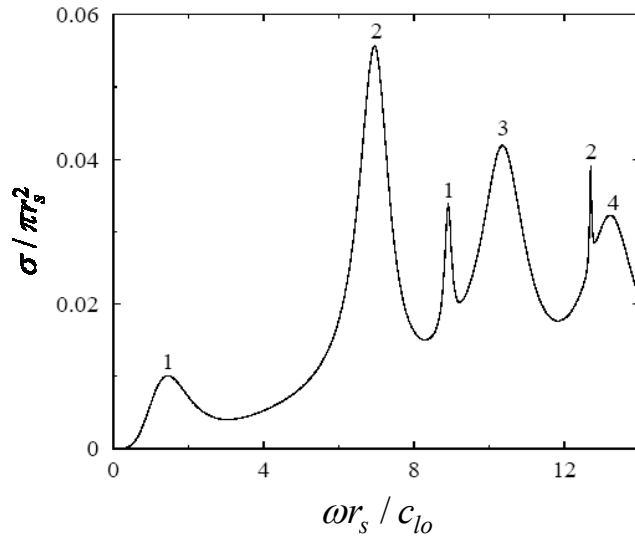


Figure 2.4 Total dimensionless scattering cross section of silica spheres in cyclohexane/decalin matrix. The incident wave is longitudinal and the numbers on top of the peaks denote the spherical harmonics l responsible for the resonances. Silica: $\rho = 1.83 \text{ g/cm}^3$, $v_l = 5600 \text{ m/s}$, $v_t = 3400 \text{ m/s}$; matrix: $\rho = 0.78 \text{ g/cm}^3$, $v_l = 1270 \text{ m/s}$, $v_t = 0$. (see Ref.[63])

2.5 Elastic waves in periodic elastic composites

2.5.1 General overview

Composite materials with periodic variations of density and/or sound velocities are often called phononic crystals as introduced in Chapter 1. Elastic wave propagation in phononic crystals differs greatly from that in a homogeneous medium, with the most distinct characteristic being the possible formation of phononic bandgaps. Although this phenomenon is similar to the appearance of electronic bandgaps in semi-conductors and electromagnetic bandgaps in photonic crystals, the situation for the elastic wave propagation is much more complicated due to the full vector nature of the wave field and the large number of material parameters involved. Regarding the latter difference, for example, in the case of a binary system (consisting of material 2 distributed in material 1), we have for photonic crystals two independent parameters: the ratio of the dielectric constants of the two materials, $\varepsilon_2/\varepsilon_1$, and the fractional volume occupied by material 2, φ . Yet for phononic

crystals there are five independent parameters: μ_2/μ_1 , λ_2/λ_1 , ρ_2/ρ_1 , μ_2/λ_1 and φ , where ρ_j , λ_j and μ_j denote the mass density, and the Lamé coefficients of the material $j=1, 2$.

Motivated by the promising technological applications, the study of phononic crystals is currently focused mainly on the search for phononic crystals that can display complete (or absolute) bandgaps, where no elastic wave can propagate whatever the direction of propagation. Moreover, the exploration of elastic wave propagation in phononic crystals can also lead to a deeper insight into the wave localization phenomenon in random media. As suggested by John and Rangarajan [64], and by Economou and Zdetsis [65], the existence of a band of localized eigenstates in a random system is directly related to the existence of spectral gaps in a periodic system, since both are due to destructive interference of multiply scattered waves. Indeed, by gradually disordering a periodic system possessing gaps, one creates tails of localized eigenstates within the gap. At the same time, also the band states of the periodic crystal near the gap become localized, thus increasing the frequency range where acoustic waves cannot be transmitted through the system [66].

The detailed wave propagation behavior in phononic crystals depends on the lattice type, the topology and the elastic combinations. To theoretically investigate the normal modes in phononic crystals, which in the most general case include both propagating and non-propagating modes, more complex computation techniques have to be used. Various methods have been developed for the calculation of the frequency band structure of phononic crystals, some most often used include the plane-wave (PW) method [67,68], the multiple-scattering (MS) method [52-54], and the finite-difference-time domain method (FDTD) [69]. In the following, the PW and the MS methods will be briefly introduced.

2.5.2 The plane-wave (PW) method

The PW method is a fast and easy-to-apply method for the calculation of the band structure of an infinite periodic composite. It is based on the expansion of the periodic coefficients in the wave equation into Fourier series. This method is ideal for the calculation of the dispersion relation of solid/solid or fluid/fluid composites, but it encounters problems for mixed (solid/fluid) composites. Let's first consider the solid/solid combination.

The starting point of the calculation is the general elastic wave equation for isotropic elastic medium, which has the following form:

$$\frac{\partial^2 u_i}{\partial t^2} = \frac{1}{\rho} \left\{ \frac{\partial}{\partial x_i} \left(\lambda \frac{\partial u_l}{\partial x_l} \right) + \frac{\partial}{\partial x_l} \left[\mu \left(\frac{\partial u_i}{\partial x_l} + \frac{\partial u_l}{\partial x_i} \right) \right] \right\}, \quad i, l=1, 2, 3, \quad (2.54)$$

where u_i and x_i are the Cartesian components of the displacement vector $\mathbf{u}(\mathbf{r}, t)$ and of the position vector \mathbf{r} , respectively. The density $\rho(\mathbf{r})$ and the two Lamé coefficients $\lambda(\mathbf{r})$ and $\mu(\mathbf{r})$ are functions of the position vector \mathbf{r} . Assuming the time-dependent displacement vector to be of the form $\mathbf{u}(\mathbf{r}, t) = \mathbf{u}(\mathbf{r})e^{-i\omega t}$, Eq. (2.54) then becomes,

$$-\omega^2 u_i = \frac{1}{\rho} \left\{ \frac{\partial}{\partial x_i} \left(\lambda \frac{\partial u_l}{\partial x_l} \right) + \frac{\partial}{\partial x_l} \left[\mu \left(\frac{\partial u_i}{\partial x_l} + \frac{\partial u_l}{\partial x_i} \right) \right] \right\}, \quad i, l=1, 2, 3. \quad (2.55)$$

For a phononic crystal, in general all the elastic parameters ρ , λ and μ are periodic functions of spatial coordinates \mathbf{r} , namely,

$$f(\mathbf{r} + \mathbf{R}) = f(\mathbf{r}), \quad (2.56)$$

where \mathbf{R} is a lattice vector, and $f(\mathbf{r})$ stands for $\lambda(\mathbf{r})$, $\mu(\mathbf{r})$ or $\rho^{-1}(\mathbf{r})$. Because of the periodicity of the lattice, $f(\mathbf{r})$ can be expanded into a three-dimensional Fourier series,

$$f(\mathbf{r}) = \sum_{\mathbf{G}} f_{\mathbf{G}} e^{i\mathbf{G}\cdot\mathbf{r}}, \quad (2.57)$$

where the summation extends over all reciprocal lattice vectors \mathbf{G} . Due to the periodicity of ρ , λ and μ , which are the coefficients in Eq. (2.55), its eigensolutions can be written in the following form according to Bloch's theorem,

$$\mathbf{u}(\mathbf{r}) = e^{i\mathbf{k}\cdot\mathbf{r}} \mathbf{u}_{\mathbf{k}}(\mathbf{r}). \quad (2.58)$$

Here \mathbf{k} is a vector in the reciprocal lattice, and $\mathbf{u}_{\mathbf{k}}(\mathbf{r})$ is a periodic function of \mathbf{r} that also satisfies Eq. (2.56) and therefore can be expanded into Fourier series in the same manner as in Eq. (2.57). Consequently, Eq. (2.58) can be rewritten as

$$\mathbf{u}(\mathbf{r}) = \sum_{\mathbf{G}} \mathbf{u}_{\mathbf{k}+\mathbf{G}} e^{i(\mathbf{k}+\mathbf{G})\cdot\mathbf{r}}. \quad (2.59)$$

Substituting Eq. (2.57) (with $f = \lambda, \mu, \rho^{-1}$) and Eq. (2.59) into Eq. (2.55) finally leads to

$$\omega^2 u_{\mathbf{k}+\mathbf{G}}^i = \sum_{\mathbf{G}'} \left\{ \sum_{l, \mathbf{G}''} \rho_{\mathbf{G}-\mathbf{G}'}^{-1} [\lambda_{\mathbf{G}''-\mathbf{G}'} (\mathbf{k}+\mathbf{G}')_l (\mathbf{k}+\mathbf{G}'')_i + \mu_{\mathbf{G}''-\mathbf{G}'} (\mathbf{k}+\mathbf{G}')_i (\mathbf{k}+\mathbf{G}'')_l] u_{\mathbf{k}+\mathbf{G}'}^l + \sum_{\mathbf{G}''} \left[\rho_{\mathbf{G}-\mathbf{G}''}^{-1} \mu_{\mathbf{G}''-\mathbf{G}'} \sum_j (\mathbf{k}+\mathbf{G}')_j (\mathbf{k}+\mathbf{G}'')_j \right] u_{\mathbf{k}+\mathbf{G}''}^i \right\}. \quad (2.60)$$

Here $u_{\mathbf{k}+\mathbf{G}}^i$ ($i=1, 2, 3$) are the Fourier transformation coefficients of u^i , the Cartesian components of the displacement vector $\mathbf{u}(\mathbf{r})$. If the infinite series in Eq. (2.57) and Eq. (2.59) can be approximated by a sum over N reciprocal vectors, then Eq. (2.60) can be reduced to a $3N \times 3N$ matrix eigenvalue equation of the form $\mathbf{A}\mathbf{X} = \omega^2 \mathbf{X}$ for the $3N$ unknown coefficients $u_{\mathbf{k}+\mathbf{G}}^i$. The number of N needed depends on the desired convergence. For a good convergence better than 1%, N is on the order of 400-500.

The calculation is done for some \mathbf{k} directions in the first Brillouin zone (BZ), especially those of high-symmetry near the center and at the boundary of the zone. For a given \mathbf{k} in the first BZ, it turns out that an infinite number of eigensolutions are obtained, each characterized by a natural number n (besides \mathbf{k}), and the corresponding eigenfrequency is $\omega_{\mathbf{k},n}$. Usually one plots $\omega_{\mathbf{k},n}$ vs \mathbf{k} for $n=1, 2, 3, \dots$, as the tip of \mathbf{k} varies along straight segments in the first BZ. A spectral gap corresponds to a region in the frequency axis to which no $\omega_{\mathbf{k},n}$ belongs.

Figure 2.5 shows an example of the band structure calculated by the PW method, for elastic wave propagation in an fcc (face-centered-cubic) lattice consisting of Pb spheres embedded in an epoxy matrix. The volume fraction occupied by the spheres is $\varphi = 0.25$. The calculation is done for \mathbf{k} in a few high symmetry directions in the first BZ ($U-L-\Gamma-X-W-K$) up to the first sixteen bands. A wide complete gap appears between the sixth and the seventh band.

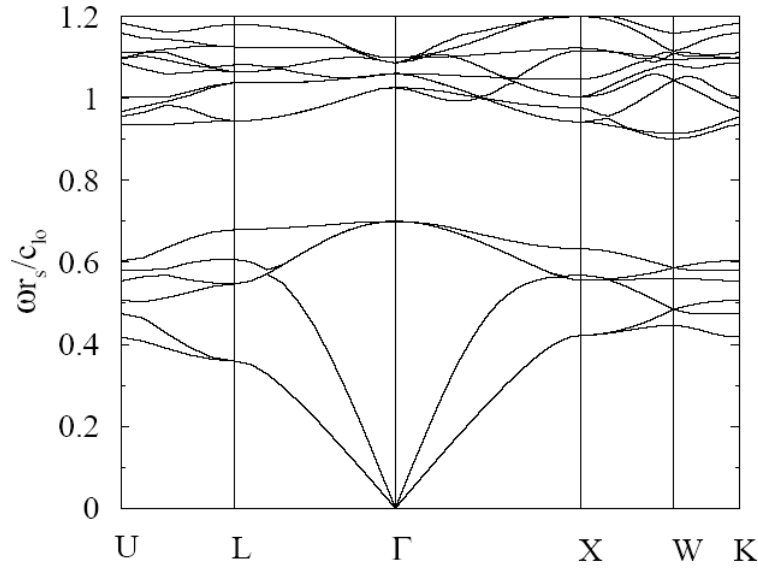


Figure 2.5 Phononic band structure for an fcc lattice of Pb spheres in epoxy. *The wavevector varies across the irreducible Brillouin zone. The volume fraction of the Pb spheres is $\varphi=0.25$. The relevant elastic parameters for Pb and epoxy are: for Pb, $\rho=11.36 \text{ g/cm}^3$, $c_l=2160 \text{ m/s}$, $c_t=860 \text{ m/s}$; for epoxy, $\rho=1.18 \text{ g/cm}^3$, $c_l=2540 \text{ m/s}$, $c_t=1160 \text{ m/s}$. (see Ref. [63])*

When dealing with a fluid/fluid composite, the treatment is very similar. The only difference is that in this case $\mu=0$, and by introducing the pressure $p=-\lambda\nabla\cdot\mathbf{u}$, Eq. (2.55) becomes

$$\lambda(\mathbf{r})\nabla\cdot\left[\rho^{-1}(\mathbf{r})\nabla p(\mathbf{r})\right]+\omega^2 p(\mathbf{r})=0. \quad (2.61)$$

Following the same steps as before (i.e. the Fourier transformation of $\lambda(\mathbf{r})$ and $\rho^{-1}(\mathbf{r})$, and the application of Bloch's theorem to the pressure field, $p(\mathbf{r})=e^{i\mathbf{k}\cdot\mathbf{r}}p_{\mathbf{k}}(\mathbf{r})$), the corresponding form of Eq. (2.60) is

$$\sum_{\mathbf{G}''} \sum_{\mathbf{G}'} \lambda_{\mathbf{G}-\mathbf{G}'} \rho_{\mathbf{G}'-\mathbf{G}''}^{-1} (\mathbf{k}+\mathbf{G}')\cdot(\mathbf{k}+\mathbf{G}'') p_{\mathbf{k}+\mathbf{G}''} = \omega^2 p_{\mathbf{k}+\mathbf{G}}. \quad (2.62)$$

Eq. (2.62) is an $N\times N$ matrix eigenvalue equation for N Fourier expansion terms, in contrast to a $3N\times 3N$ matrix equation in the case of solid/solid combination.

Despite its success in band structure calculation, the PW method has some limitations. First, it encounters problems in the calculation of the dispersion relation of mixed

(fluid/solid) composites, e.g. solid scatterers in fluid host. In this case, besides the normal modes of the whole system which are purely longitudinal, there exist also transverse modes localized inside the solid scatterers. The PW method is unsuitable to describe this kind of modes due to their localized character. Secondly, this method cannot calculate the wave propagation in non-periodic systems. In addition, the PW method can only be applied to infinite periodic elastic structures and is also unable to calculate the transmission properties. Therefore new methods are desired to overcome these shortcomings, and one of them is the multiple scattering algorithm.

2.5.3 The multiple-scattering (MS) method

The MS method is a powerful method for band structure calculation, it can be applied to both periodic and non-periodic composites, can treat mixed (solid/fluid) composites, deal with finite systems and account for the transmission properties. The MS method is based on the well-known Korringa-Kohn-Rostoker (KKR) theory in the electronic band structure community [70]. In the following, we shortly describe the calculation of elastic wave band structure by the MS method with reference to periodic systems consisting of non-overlapping spherical solid scatterers embedded in fluid host.

The basic idea is that the incident wave on one sphere is the sum of the scattered waves from all the other spheres and the external field (if present). This can be expressed mathematically in terms of summation of the pressure fields $p(\mathbf{r})$ in the fluid defined in the previous section,

$$p_n^{inc}(\mathbf{r}) = \sum_{p \neq n} p_p^{sc}(\mathbf{r}) + p_0(\mathbf{r}), \quad (2.63)$$

where $p_0(\mathbf{r})$ is the external field and the subscripts n and p denote the scatterer at the position \mathbf{R}_n and \mathbf{R}_p , respectively. For the calculation of the global eigenmodes, the external field must be taken as zero and Eq. (2.63) becomes

$$p_n^{inc}(\mathbf{r}) = \sum_{p \neq n} p_p^{sc}(\mathbf{r}). \quad (2.64)$$

Both sides of Eq. (2.64) can be expanded as a sum of elementary spherical waves, that is,

$$p_p^{sc}(\mathbf{r}) = \sum_{lm} b_{lm}^p \Phi_{lm}^p(\mathbf{r}), \quad (2.65)$$

$$p_n^{inc}(\mathbf{r}) = \sum_{lm} a_{lm}^n \Psi_{lm}^n(\mathbf{r}), \quad (2.66)$$

where $\Phi_{lm}^p(\mathbf{r}) = h_l(k_o |\mathbf{r} - \mathbf{R}_p|) Y_{lm}(\mathbf{r} - \mathbf{R}_p)$, $\Psi_{lm}^n(\mathbf{r}) = j_l(k_o |\mathbf{r} - \mathbf{R}_n|) Y_{lm}(\mathbf{r} - \mathbf{R}_n)$ and $k_o = \omega/c_o$ with c_o the sound velocity in the host material. Inserting Eq. (2.65) and (2.66) into Eq. (2.64), one can obtain

$$\sum_{lm} a_{lm}^n \Psi_{lm}^n(\mathbf{r}) = \sum_{p \neq n} \sum_{lm} b_{lm}^p \Phi_{lm}^p(\mathbf{r}). \quad (2.67)$$

The coefficients b_{lm}^p are proportional to a_{lm}^p ,

$$b_{lm}^p = t_l^p a_{lm}^p. \quad (2.68)$$

The proportionality coefficient t_l^p is called scattering coefficient which can be found by solving a single scattering problem [52,62] as in Section 2.4.2. Due to the periodicity of the system under consideration, all the scatterers are identical, thus $t_l^p \equiv t_l$ is independent of the lattice position.

The spherical functions in Eq. (2.65) centered at \mathbf{R}_p can be transformed to functions centered at \mathbf{R}_n ,

$$\Phi_{lm}^p(\mathbf{r}) = \sum_{l'm'} \Psi_{l'm'}^n(\mathbf{r}) g_{l'm'lm}^{(h)}(\mathbf{R}_p - \mathbf{R}_n) \quad (2.69)$$

for $|\mathbf{r} - \mathbf{R}_n| < |\mathbf{R}_p - \mathbf{R}_n|$,

where $g_{l'm'lm}^{(R)}(\mathbf{D}) = \sum_{\lambda} \left[(-1)^{(l'-l-\lambda)/2} 4\pi C_{l'm';lm;\lambda m-m'} R_{\lambda}(kD) \times Y_{\lambda m-m'}(D) \right]$, $R=j$ or h , and

$C_{l'm';lm;\lambda m-m'}$ are the Gaunt numbers [52,71]. Applying Bloch's theorem, the coefficients b_{lm}^p at different lattice sites can be connected,

$$b_{lm}^p = e^{i\mathbf{k} \cdot (\mathbf{R}_p - \mathbf{R}_n)} b_{lm}^n. \quad (2.70)$$

Substituting Eq. (2.68), (2.69) and (2.70) into Eq. (2.67), interchanging the (l', m') with the (l, m) , after a few algebraic manipulations, we obtain

$$\sum_{l'm'} \left[(t_{l'})^{-1} \delta_{ll'} \delta_{mm'} - \sum_p e^{i\mathbf{k} \cdot (\mathbf{R}_p - \mathbf{R}_n)} \times g_{lm'l'm'}^{(h)}(\mathbf{R}_p - \mathbf{R}_n)(1 - \delta_{pn}) \right] b_{l'm'}^n = 0. \quad (2.71)$$

Eq. (2.71) is a linear homogeneous algebraic system. To have nontrivial solutions the determinant must vanish, which gives the eigenmodes of this periodic system. In other words, the dispersion relation is obtained.

Figure 2.6 shows the elastic wave band structure of two fcc periodic composites calculated by the MS method (open circles). One system consists of steel spheres in air (**Fig. 2.6a**) and the other is made of glass spheres in water (**Fig. 2.6b**), the volume fraction of the spheres in both cases is $\varphi = 0.5$. For comparison, the band structure calculated by the PW method is also given (solid lines). Note that in order to apply the PW method to such a solid/fluid combination, the transverse component of the wave within the solid scatterer is completely ignored, namely, $\mu = 0$ is used.

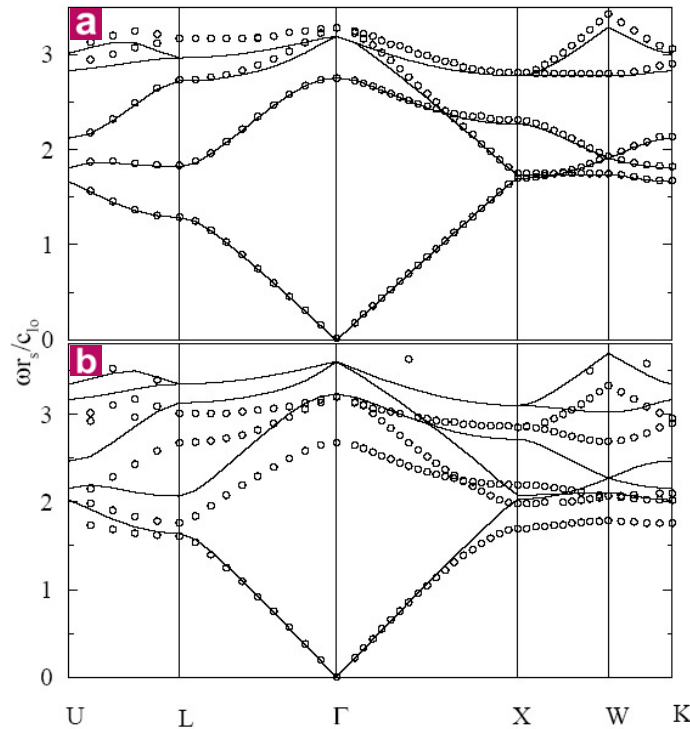


Figure 2.6 Phononic band structure for two fcc phononic crystals. The open circles are calculation results from the MS method and the solid lines are from the PW method. The volume fraction of the spheres in both systems is $\varphi = 0.25$. **a**, Steel spheres in air. Material parameters: steel, $\rho = 7.8 \text{ g/cm}^3$, $c_l = 5940 \text{ m/s}$, $c_t = 3220 \text{ m/s}$; air, $\rho = 0.001 \text{ g/cm}^3$, $c_l = 345 \text{ m/s}$, $c_t = 0$. **b**, Glass spheres in water. Material parameters: glass, $\rho = 2.5 \text{ g/cm}^3$, $c_l = 5700 \text{ m/s}$, $c_t = 3400 \text{ m/s}$; water, $\rho = 1.0 \text{ g/cm}^3$, $c_l = 1500 \text{ m/s}$, $c_t = 0$. (see Ref.[63])

In **Fig. 2.6a**, the MS method and the PW method are in very good agreement for the system consisting of steel spheres in air. The success of the PW method in this case is due to the very large elastic mismatch between steel and air. Under such a condition, the steel spheres are so “hard” as to exclude almost all traveling waves from penetrating into its interior, as a result, the details of the waves inside the sphere are irrelevant. However, for the glass/water combination which has smaller elastic contrast, the PW method which neglects the shear stress of the solid, is no longer acceptable. Large deviation from the results by the MS method appears as in **Fig. 2.6b**.

A very powerful variant of the MS method is the so-called layer-multiple-scattering (LMS) method, which can describe elastic composites with the same two-dimensional periodicity (in the x - y plane) while periodicity along the normal (z) direction is not required [53,54]. Therefore, this method allows to calculate the frequency band structure of a three-dimensional phononic crystal, viewed as an infinite succession of planes of scatterers parallel to a given crystallographic plane (layers), but also the transmission and reflection coefficients of an acoustic wave incident at a given angle on a finite slab of the crystal. Composite systems which include, in addition, homogeneous slabs and/or substrates can be treated in a straightforward manner, thus allowing the realistic description of an actual experiment. The LMS method takes into account the full vector nature of the acoustic field, consequently it can be applied to systems of solid or fluid scatterers in a fluid or solid host. An additional advantage of the method is that, contrary to traditional band structure or time-domain methods, it proceeds at a given frequency, i.e., it is an “on-shell” method. Therefore, it can directly describe composite media characterized by frequency-dependent elastic coefficients and treat absorption or viscosity. Further, it provides all modes, propagating and evanescent, of the system at a given frequency. The LMS method employs spherical-wave expansions for the acoustic field to describe multiple scattering within each plane of scatterers, while interlayer multiple scattering is evaluated by expanding the field into plane waves. A powerful computer program which implements numerically the LMS method became recently available [72].

Chapter 3

Light scattering basics

The experimental investigation of the propagation of elastic waves in an elastic medium with spatial periodicities or inhomogeneities in the length scale of tens of nanometers to a few micrometers cannot be realized by using conventional acoustic methods, e.g. ultrasonic transmission technique which uses a couple of ultrasonic broadband transmitter/receiver transducers, due to the very high frequencies (GHz) associated with these waves. In this work, a noncontact, nondestructive method which is so far unique to achieve this purpose was employed. It is based on the scattering of light by thermally excited phonons, referred to as Brillouin light scattering (BLS). By analyzing the scattered light, information about the excited phonons can be obtained since the scattering process is very sensitive to the characteristics of the phonons. In this chapter, the mechanism responsible for BLS will be discussed.

3.1 Fundamental light scattering theory

In the following theoretical description of light scattering, both the scattering medium and the light are treated classically, without having to specify the molecular properties. In fact, a single molecule can also scatter light, e.g. the well-known molecular Raman scattering. In that case a satisfied description of the scattering process requires at least treating the molecule quantum mechanically [73]. The discussion of scattering of light by such quantum systems is beyond the scope of this dissertation, and for our purposes it is sufficient to confine ourselves to the phenomenological description on the basis of classical electromagnetic theory.

The optical property of an isotropic medium (nonmagnetic, nonconducting, nonabsorbing) is usually characterized by the dielectric constant ε_0 . More precisely speaking, this is only an average value, and the dielectric constant associated with a local volume is actually fluctuating around ε_0 owing to the thermal motion of the molecules of the medium. Taking into account possible anisotropy introduced by the fluctuation of the relative orientations of anisotropic molecules, the local dielectric constant, in its most general form, becomes a tensor quantity, and can be written as

$$\boldsymbol{\varepsilon}(\mathbf{r}, t) = \varepsilon_0 \mathbf{I} + \delta\boldsymbol{\varepsilon}(\mathbf{r}, t), \quad (3.1)$$

where $\delta\boldsymbol{\varepsilon}(\mathbf{r}, t)$ is the dielectric constant fluctuation tensor at position \mathbf{r} and time t , \mathbf{I} is the second-rank unit tensor. Suppose the incident light to be a plane wave of the form

$$\mathbf{E}_i(\mathbf{r}, t) = \mathbf{n}_i E_0 \exp i(\mathbf{k}_i \cdot \mathbf{r} - \omega_i t), \quad (3.2)$$

where \mathbf{n}_i is a unit vector in the direction of the incident electric field, E_0 is the field amplitude, \mathbf{k}_i is the wavevector, and ω_i is the angular frequency. The scattered electric field $\mathbf{E}_s(\mathbf{R}, t)$ at a large distance R from the scattering volume can be computed by demanding that the total field $\mathbf{E} = \mathbf{E}_i + \mathbf{E}_s$ satisfies the Maxwell equations throughout all space. The detailed derivation can be found in Ref. [74,75], here only the solution of the Maxwell equations is given, as it is the physics behind instead of the extensive mathematics that concerns us.

The component of the scattered electric field at a large distance R from the scattering volume with polarization \mathbf{n}_s , wavevector \mathbf{k}_s , and frequency ω_s is [74]

$$E_s(R, t) = \frac{E_0}{4\pi R \varepsilon_0} \exp i k_s R \int_V d^3 r \exp i(\mathbf{q} \cdot \mathbf{r} - \omega_i t) [\mathbf{n}_s \cdot [\mathbf{k}_s \times (\mathbf{k}_s \times (\delta\boldsymbol{\varepsilon}(\mathbf{r}, t) \cdot \mathbf{n}_i))]]. \quad (3.3)$$

Although this equation looks complicated, its components can be broken down and the essence can be understood physically without the need to resort to complex mathematics. In **Fig. 3.1** a large portion of the scattering volume V is indicated by the irregular region in yellow, O inside the scattering volume is the origin of the established reference coordinate system. The detector of the scattered light is located at the position \mathbf{R} with respect to the origin, \mathbf{r} is the position of an infinitesimal volume element inside the scattering volume, and the distance vector between the volume element and the detector is given by $\mathbf{R} - \mathbf{r}$, here $R \gg r$ (**Fig. 3.1a**). The so-called scattering wavevector \mathbf{q} is defined as the vector difference

between the wavevector of the incident light (\mathbf{k}_i) and that of the scattered light (\mathbf{k}_s), whose magnitude can be readily calculated as follows by referring to **Fig. 3.1b**,

$$q^2 = |\mathbf{k}_s - \mathbf{k}_i|^2 = k_s^2 + k_i^2 - 2\mathbf{k}_i \cdot \mathbf{k}_s = 2k_i^2 - 2k_i^2 \cos \theta = 4k_i^2 \sin^2 \frac{\theta}{2}$$

$$\text{or } q = 2k_i \sin \frac{\theta}{2} = \frac{4\pi n}{\lambda_i} \sin \frac{\theta}{2}. \quad (3.4)$$

In the above, the relation $|\mathbf{k}_i| \cong |\mathbf{k}_s|$ was used since the incident wavelength (λ_i) changes very little in the scattering process.

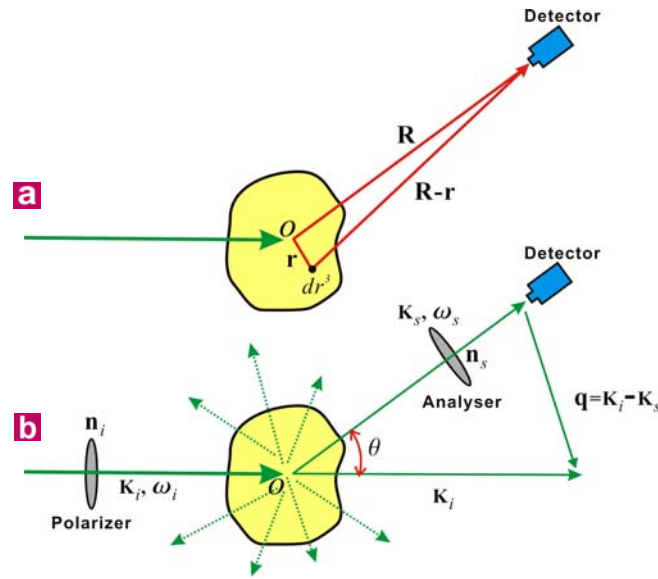


Figure 3.1 Scheme of light scattering geometry. **a**, The relative position of the scattering volume V and the detector, the yellow region denotes a large portion of the scattering volume. Note that the size of the scattering volume is exaggerated for clarity. The total scattered field at the detector is the superposition of the fields radiated from all infinitesimal volumes d^3r at position \mathbf{r} with respect to the center of the scattering volume. **b**, The light scattering process. The incident light impinges onto the sample and is scattered in all directions. The position of the detector determines the scattering geometry which further defines the scattering wavevector $\mathbf{q} = \mathbf{k}_i - \mathbf{k}_s$. The polarizer and the analyzer are used to select the polarization state of the incident and scattered light, respectively.

In Eq. (3.3), the integration is performed over the whole space within the scattering volume V , and it only influences terms in the integrand containing the space coordinates \mathbf{r} . Eq. (3.3) can be then rewritten as

$$E_s(R, t) = \frac{E_0}{4\pi R \epsilon_0} \exp i(k_s R - \omega_i t) \left[\mathbf{n}_s \cdot \left[\mathbf{k}_s \times (\mathbf{k}_s \times (\int_V d^3r \exp i\mathbf{q} \cdot \mathbf{r} \delta \epsilon(\mathbf{r}, t)) \cdot \mathbf{n}_i)) \right] \right], \quad (3.5)$$

where the term $\frac{E_0}{4\pi R\epsilon_0} \exp i(k_s R - \omega_i t)$ represents a spherical wave emitted from the origin O in the scattering volume. Its appearance is not unexpected since the scattering volume is rather small compared to its distance to the detector. To a first approximation, the scattering volume can be regarded as a point scatterer at the origin. Certainly this picture is oversimplified and corrections are needed. The integral $\int_V dr^3 \exp i\mathbf{q} \cdot \mathbf{r} \delta\boldsymbol{\epsilon}(\mathbf{r}, t)$ accounts for the interference effect between the wavelets emitted from different volume elements within the finite scattering volume. The vector cross and dot products are responsible for the angular distribution and the polarization of the scattered field.

The integral is actually the spatial Fourier transformation of the dielectric fluctuation $\delta\boldsymbol{\epsilon}(\mathbf{r}, t)$:

$$\delta\boldsymbol{\epsilon}(\mathbf{q}, t) = \int_V dr^3 \exp i\mathbf{q} \cdot \mathbf{r} \delta\boldsymbol{\epsilon}(\mathbf{r}, t). \quad (3.6)$$

Eq. (3.5) then becomes

$$E_s(R, t) = \frac{E_0}{4\pi R\epsilon_0} \exp i(k_s R - \omega_i t) [\mathbf{n}_s \cdot [\mathbf{k}_s \times (\mathbf{k}_s \times (\delta\boldsymbol{\epsilon}(\mathbf{q}, t) \cdot \mathbf{n}_i))]]. \quad (3.7)$$

By working out the vector product Eq. (3.7) can be simplified to

$$E_s(R, t) = \frac{-k_s^2 E_0}{4\pi R\epsilon_0} \exp i(k_s R - \omega_i t) \delta\epsilon_{is}(\mathbf{q}, t), \quad (3.8)$$

where $\delta\epsilon_{is}(\mathbf{q}, t) \equiv \mathbf{n}_s \cdot \delta\boldsymbol{\epsilon}(\mathbf{q}, t) \cdot \mathbf{n}_i$ is the component of the dielectric constant fluctuation tensor along the initial and final polarization directions. The time-correlation function of E_s can be computed as

$$\langle E_s^*(R, 0) E_s(R, t) \rangle = \frac{k_s^4 E_0^2}{16\pi^2 R^2 \epsilon_0^2} \langle \delta\epsilon_{is}^*(\mathbf{q}, 0) \delta\epsilon_{is}(\mathbf{q}, t) \rangle \exp i(-\omega_i t). \quad (3.9)$$

And the spectral density of the scattered light reads,

$$\begin{aligned} I_{is}(\mathbf{q}, \omega_s, R) &= \int dt \exp i\omega_s t \langle E_s^*(R, 0) E_s(R, t) \rangle \\ &= \frac{k_s^4 I_0}{16\pi^2 R^2 \epsilon_0^2} \int dt \langle \delta\epsilon_{is}^*(\mathbf{q}, 0) \delta\epsilon_{is}(\mathbf{q}, t) \rangle \exp i(\omega_s - \omega_i) t, \quad (3.10) \\ &= \frac{k_s^4 I_0}{16\pi^2 R^2 \epsilon_0^2} \int dt \langle \delta\epsilon_{is}^*(\mathbf{q}, 0) \delta\epsilon_{is}(\mathbf{q}, t) \rangle \exp i\omega t \end{aligned}$$

where $\omega \equiv \omega_s - \omega_i$ is the frequency change in the scattering process, and $I_0 \equiv E_0^2$ is the incident beam intensity. Important features of Eq. (3.10) are:

1. $I_{is} \propto k_s^4$ (or λ^{-4}), the scattering intensity is inversely proportional to the fourth power of the light wavelength.
2. $I_{is} \propto R^{-2}$, this R^{-2} dependence is expected from a spherical wave.
3. I_{is} depends on ω_i and ω_s only through their difference $\omega \equiv \omega_s - \omega_i$.

Note that for a given scattering experiment, the proportionality coefficient in Eq. (3.10) is a constant and the scattering intensity is then determined by the integral which is in fact the spectral density of the dielectric constant fluctuations:

$$I_{is}(\mathbf{q}, \omega) = \int dt \langle \delta\epsilon_{is}^*(\mathbf{q}, 0) \delta\epsilon_{is}(\mathbf{q}, t) \rangle \exp i\omega t. \quad (3.11)$$

If $\delta\epsilon_{is}(\mathbf{q}, t)$ is time-independent, obviously I_{is} is non-zero only when $\omega=0$. This means that “frozen” fluctuations (static optical inhomogeneities) can only lead to elastic scattering, in which the frequency of the scattered wave coincides to the frequency of the incident wave. The frequency changes only when $\delta\epsilon_{is}(\mathbf{q}, t)$ varies with time.

From the above discussion it is easy to appreciate that the light scattering spectrum $I_{is}(\mathbf{q}, \omega)$ directly measures the local dielectric constant fluctuations in a medium, which is in turn caused by various thermal fluctuations, e.g. density fluctuations, orientation fluctuations for anisotropic molecules. Therefore light scattering can in principle provide valuable information about diverse dynamic processes in a system.

3.2 Introduction to BLS

BLS usually refers to the scattering of light by thermal sound waves in a medium. The most distinct characteristic of BLS is the appearance of a doublet in the frequency distribution of the scattered light. This doublet was first predicted by Leon Brillouin [76] and now is known as the Brillouin doublet.

3.2.1 A simple approach to BLS

In its simplest description, BLS can be understood as constructive interference between multiply reflected light beams by sound waves. To appreciate this, let's refer to **Fig. 3.2** where the interaction of the incident light and the propagating sound wave is schematically depicted assuming a plane wave form with a wavelength Λ . The existence of such an elastic wave in the medium modulates the local dielectric constant which also assumes a plane wave form of identical wavelength traveling along the same direction.

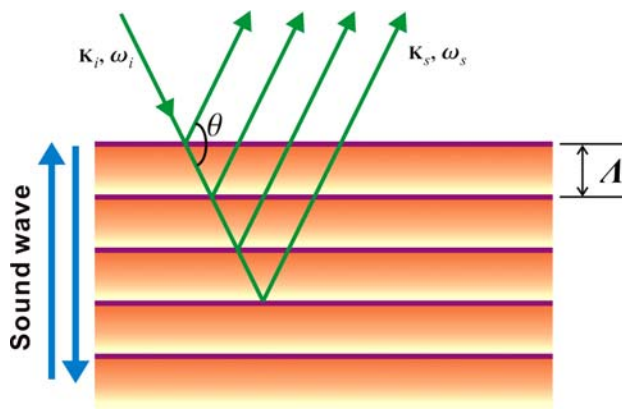


Figure 3.2 Understanding Brillouin light scattering from multiple-beam interference. The scattering process can be regarded as constructive interference between multiply reflected beams at the interface between two adjacent “layers”. Each “layer” has a thickness corresponding to the wavelength (Λ) of the sound which produces the “multilayers”.

Due to the large discrepancy between the speed of light ($\sim 3 \times 10^8$ m/s) and sound ($\sim 3 \times 10^5$ m/s), at any given instant when a single light scattering event happens, the spatial variation of the dielectric constant in the medium can be regarded as “frozen”, i.e. static dielectric inhomogeneities described by a spatial plane wave. The travel of the beam inside the medium is then very similar to that in a periodic multilayer stack with periodicity Λ as shown in **Fig. 3.2**, where the light beam undergoes multiply reflections³⁻¹. The maximum reflected intensity, or the scattering, will occur only when the condition for constructive interference is satisfied, namely,

$$2n\Lambda \sin \frac{\theta}{2} = \lambda_i. \quad (3.12)$$

Here, n is the refractive index of the medium, λ_i is the wavelength of the incident light, and θ is the angle between the incident and reflected beams. The Bragg condition, Eq. (3.12), can be rewritten as

³⁻¹ For more details about multiple beam interference, see Chapter 4.

$$\frac{2\pi}{\Lambda} = \frac{4\pi n}{\lambda_i} \sin \frac{\theta}{2}. \quad (3.13)$$

A comparison of Eq. (3.13) and Eq. (3.4) leads to

$$q = \frac{2\pi}{\Lambda}. \quad (3.14)$$

Eq. (3.14) indicates that the wavevector \mathbf{k} ($k = 2\pi / \Lambda$) of the sound wave is equivalent to the scattering wavevector \mathbf{q} . By changing the scattering angle θ , a different \mathbf{q} is selected and correspondingly different sound waves are probed by BLS. The equality $\mathbf{q}=\mathbf{k}$ reflects the exchange of momentum between the sound wave and the light during the scattering process.

The traveling sound wave has a certain phase velocity, say v , therefore the frequency f_s of the scattered light seen by the detector suffers a Doppler shift, that is,

$$f_s = f_i \left(1 \pm 2 \frac{v}{c} \sin \frac{\theta}{2}\right), \quad (3.15)$$

where f_i is incident light frequency and $c = f_i \lambda_i / n$ is the velocity of light within the scattering medium. The plus and minus signs correspond to the two possible propagation directions of the sound wave: one is toward the detector (“+”) leading to an increase in the frequency of the scattered light (anti-Stokes scattering), the other is away from the detector (“−”) leading to a frequency decrease (Stokes scattering). Eq. (3.15) can be further simplified to:

$$\begin{aligned} f_s &= f_i \pm \frac{v}{2\pi} \frac{4\pi n}{\lambda_i} \sin \frac{\theta}{2} \\ &= f_i \pm \frac{v}{2\pi} q \end{aligned} \quad (3.16)$$

In terms of angular frequency,

$$\omega = \omega_s - \omega_i = \pm vq. \quad (3.17)$$

Now it becomes clear that in the scattering spectrum $I_{is}(\mathbf{q}, \omega)$ there is a doublet centered at the frequency $\omega = \pm vq$. Since q is also the wavenumber of the sound wave (Eq. (3.14)) traveling at a speed v , then ω naturally becomes the angular frequency of the sound wave. Therefore Eq. (3.17) reflects the energy exchange between the sound wave and the light.

As already mentioned we do not have to invoke any quantum mechanical treatment. However, some basic concepts from quantum mechanics can offer a better understanding of

BLS. The scattering process is in fact governed by two fundamental laws in nature, as seen already, the momentum conservation and the energy conservation. These two conservation laws can be more easily appreciated by viewing the scattering event in terms of inelastic photon-phonon collisions. An incident photon with energy $\hbar\omega_i$ and momentum $\hbar\mathbf{k}_i$ is inelastically scattered by a phonon of energy $\hbar\omega$ and momentum $\hbar\mathbf{q}$ in the scattering medium. During this process a phonon is either created with the scattered photon losing the corresponding energy, or annihilated with the scattered photon gaining the corresponding energy. Conservations of momentum and energy in the scattering process require

$$\text{Momentum conservation: } \hbar\mathbf{k}_s = \hbar\mathbf{k}_i \pm \hbar\mathbf{q} \quad (3.18)$$

$$\text{Energy conservation: } \hbar\omega_s = \hbar\omega_i \pm \hbar\omega \quad (3.19)$$

The plus sign corresponds to the phonon annihilation (anti-Stokes scattering), while the minus sign indicates the phonon creation (Stokes scattering).

A phonon is an elastic analogue of a photon, that is, a piece of quantized elastic energy. In the context of this dissertation, phonons are used to refer to high frequency (GHz) thermally excited elastic waves. Despite the subtle difference in the meanings of names like sound waves, elastic waves, acoustic waves, mechanical waves, elastic excitations and phonons, they will not be distinguished in this dissertation and will be used interchangeably.

3.2.2 A thermodynamic approach to BLS

The above simple approach is elegant in elucidating the main features of BLS, e.g., the appearance of the doublet and the correct prediction of its frequency in relation to the sound velocity in the medium. However, the factors that determine the intensity of the scattered light are not included. To have more complete information of the scattered light, we must recall Eq. (3.11), the most general description of light scattering and address the question how the sound wave determines the dielectric constant fluctuations $\langle \delta\varepsilon_{is}^*(\mathbf{q}, 0) \delta\varepsilon_{is}(\mathbf{q}, t) \rangle$.

Thermal sound waves in a medium are essentially density or pressure fluctuations caused by the thermal random motion of the molecules. Associated with the thermal sound waves are fluctuations of the local thermodynamic properties. For a homogeneous one-component system at equilibrium, a macroscopic physical property can in general be

specified by two independent thermodynamic parameters. Therefore the dielectric constant ε of an isotropic medium is a function of any pair of independent thermodynamic variables, e.g. the density ρ and the temperature T , or the pressure P and the entropy S , that is, $\varepsilon(\rho, T)$ or $\varepsilon(P, S)$. Note that the fluctuation of the thermal dynamical properties is isotropic and hence $\delta\varepsilon$ caused by the fluctuation is a scalar, or the tensor $\delta\varepsilon_{is}$ has no off-diagonal element. Then the scattering formula Eq. (3.11) can be simplified as

$$I_{is}(\mathbf{q}, \omega) = (\mathbf{n}_i \cdot \mathbf{n}_s)^2 \int dt \langle \delta\varepsilon(\mathbf{q}, 0) \delta\varepsilon(\mathbf{q}, t) \rangle \exp i\omega t. \quad (3.20)$$

The immediate information from the above formula is that the scattering by local fluctuations of the thermodynamic properties is polarized scattering, i.e., the scattered light has the same polarization as the incident light. This is obvious by noticing the vector product $\mathbf{n}_i \cdot \mathbf{n}_s = 0$ when $\mathbf{n}_i \perp \mathbf{n}_s$.

Usually it is convenient to choose the density ρ and the temperature T as independent variables as they are properties that can be readily measured. Expressing $\delta\varepsilon(\mathbf{r}, t)$ in terms of ρ and T , we get

$$\delta\varepsilon(\mathbf{r}, t) = \left(\frac{\partial \varepsilon}{\partial \rho} \right)_T \delta\rho(\mathbf{r}, t) + \left(\frac{\partial \varepsilon}{\partial T} \right)_\rho \delta T(\mathbf{r}, t). \quad (3.21)$$

In most cases, $\left(\frac{\partial \varepsilon}{\partial T} \right)_\rho \cong 0$ is a very good approximation. Substitution of Eq. (3.21) into Eq. (3.6) and referring to Eq. (3.20), we obtain the scattering power spectrum,

$$I_{is}(\mathbf{q}, \omega) = (\mathbf{n}_i \cdot \mathbf{n}_s)^2 \left(\frac{\partial \varepsilon}{\partial \rho} \right)_T^2 \int dt \langle \delta\rho(\mathbf{q}, 0) \delta\rho(\mathbf{q}, t) \rangle \exp i\omega t. \quad (3.22)$$

Clearly, the density fluctuations are responsible for the scattering spectrum. In this section, our main concern is the total scattering intensity,

$$I_{is}(\mathbf{q}) = \int d\omega I_{is}(\mathbf{q}, \omega), \quad (3.23)$$

rather than the detailed spectral distribution. Inserting Eq. (3.22) into Eq. (3.23), we obtain

$$\begin{aligned}
I_{is}(\mathbf{q}) &= (\mathbf{n}_i \cdot \mathbf{n}_s)^2 \left(\frac{\partial \mathcal{E}}{\partial \rho} \right)_T^2 \int dt \left(\int d\omega \exp i\omega t \right) \langle \delta\rho(\mathbf{q}, 0) \delta\rho(\mathbf{q}, t) \rangle \\
&= (\mathbf{n}_i \cdot \mathbf{n}_s)^2 \left(\frac{\partial \mathcal{E}}{\partial \rho} \right)_T^2 \int dt \delta(t) \langle \delta\rho(\mathbf{q}, 0) \delta\rho(\mathbf{q}, t) \rangle \\
&= (\mathbf{n}_i \cdot \mathbf{n}_s)^2 \left(\frac{\partial \mathcal{E}}{\partial \rho} \right)_T^2 \langle |\delta\rho(\mathbf{q})|^2 \rangle
\end{aligned} \tag{3.24}$$

According to Eq. (3.24) the total scattering intensity is simply determined by the mean-square fluctuation of the q^{th} Fourier component of the density fluctuation $\delta\rho(\mathbf{q})$. In BLS experiments the probed q is relatively small, and the corresponding $2\pi q^{-1}$ (>100 nm) is much greater than the intermolecular interactions, hence the \mathbf{q} dependence of $\delta\rho(\mathbf{q})$ can be ignored. In this case,

$$\begin{aligned}
\langle |\delta\rho(\mathbf{q})|^2 \rangle_{q \rightarrow 0} &= \left\langle \left| \int_V d\mathbf{r} e^{i\mathbf{q}\cdot\mathbf{r}} \delta\rho(\mathbf{r}) \right|^2 \right\rangle_{q \rightarrow 0} \\
&= V^2 \langle |\delta\rho(\mathbf{r})|^2 \rangle \\
&= V^2 \langle |\delta\rho|^2 \rangle
\end{aligned} \tag{3.25}$$

Statistical thermodynamics [77] shows that

$$\langle |\delta\rho|^2 \rangle = \frac{1}{V} \rho^2 k_B T \beta_T, \tag{3.26}$$

where V is the scattering volume, ρ is the average density, k_B is the Boltzmann constant, and $\beta_T = \frac{1}{\rho} \left[\frac{\partial \rho}{\partial P} \right]_T = -\frac{1}{V} \left[\frac{\partial V}{\partial P} \right]_T$ is the isothermal compressibility. The integrated scattering intensity consequently becomes

$$I_{is}(\mathbf{q}) = (\mathbf{n}_i \cdot \mathbf{n}_s)^2 \left(\frac{\partial \mathcal{E}}{\partial \rho} \right)_T^2 V \rho^2 k_B T \beta_T. \tag{3.27}$$

This formula was first derived by Einstein (1910). Neglecting the possible small change of the scattering volume V with the change of scattering angle in an experiment, the total scattering intensity is independent of \mathbf{q} .

The density fluctuations can be also expressed in terms of fluctuations of the pressure P and the entropy S . Following similar procedures and noting the statistical independence of P and S , we can easily obtain

$$\langle |\delta\rho|^2 \rangle = \left(\frac{\partial\rho}{\partial P} \right)_s^2 \langle |\delta P|^2 \rangle + \left(\frac{\partial\rho}{\partial S} \right)_p^2 \langle |\delta S|^2 \rangle. \quad (3.28)$$

Now the density fluctuations are decomposed into two independent parts:

1. *the adiabatic fluctuations* (constant entropy)
2. *the isobaric fluctuations* (constant pressure)

The scattering intensity due to the adiabatic density fluctuations is

$$I_{is}^{ad}(\mathbf{q}) = (\mathbf{n}_i \cdot \mathbf{n}_s)^2 \left(\frac{\partial\varepsilon}{\partial\rho} \right)_T^2 V^2 \left(\frac{\partial\rho}{\partial P} \right)_s^2 \langle |\delta P|^2 \rangle. \quad (3.29)$$

By definition

$$\beta_s = \frac{1}{\rho} \left(\frac{\partial\rho}{\partial P} \right)_s = -\frac{1}{V} \left(\frac{\partial V}{\partial P} \right)_s, \quad (3.30)$$

where β_s is the adiabatic compressibility. From statistical thermodynamics,

$$\langle |\delta P|^2 \rangle = \frac{k_B T}{\beta_s V}. \quad (3.31)$$

Inserting Eq. (3.30) and Eq. (3.31) into Eq. (3.29), we obtain

$$I_{is}^{ad}(\mathbf{q}) = (\mathbf{n}_i \cdot \mathbf{n}_s)^2 \left(\frac{\partial\varepsilon}{\partial\rho} \right)_T^2 V \rho^2 k_B T \beta_s. \quad (3.32)$$

The scattering intensity due to isobaric density fluctuations is

$$I_{is}^{iso}(\mathbf{q}) = (\mathbf{n}_i \cdot \mathbf{n}_s)^2 \left(\frac{\partial\varepsilon}{\partial\rho} \right)_T^2 V^2 \left(\frac{\partial\rho}{\partial S} \right)_p^2 \langle |\delta S|^2 \rangle. \quad (3.33)$$

From statistical thermodynamics,

$$\frac{1}{\rho} \left(\frac{\partial\rho}{\partial S} \right)_p = -\frac{1}{V} \left(\frac{\partial V}{\partial S} \right)_p = -\frac{T}{C_p V^2} \left(\frac{\partial V}{\partial T} \right)_p \quad (3.34)$$

$$\text{and} \quad \langle |\delta S|^2 \rangle = k_B C_p \rho V, \quad (3.35)$$

where C_p is the heat capacity at constant pressure. Since the thermal expansion coefficient α is defined as

$$\alpha = \frac{1}{V} \left(\frac{\partial V}{\partial T} \right)_P, \quad (3.36)$$

Eq. (3.33) can be rewritten as

$$I_{is}^{iso}(\mathbf{q}) = (\mathbf{n}_i \cdot \mathbf{n}_s)^2 \left(\frac{\partial \varepsilon}{\partial \rho} \right)_T^2 V \rho^2 \frac{k_B T^2 \alpha^2}{C_p \rho}. \quad (3.37)$$

The total scattering intensity is the sum of Eq. (3.32) and Eq. (3.37),

$$I_{is}(\mathbf{q}) = (\mathbf{n}_i \cdot \mathbf{n}_s)^2 \left(\frac{\partial \varepsilon}{\partial \rho} \right)_T^2 V \rho^2 k_B T \left(\beta_s + \frac{T \alpha^2}{C_p \rho} \right). \quad (3.38)$$

Compare the above formula with Eq. (3.27), the following relation is found,

$$\beta_T = \beta_s + \frac{T \alpha^2}{C_p \rho}. \quad (3.39)$$

It can be shown [75] (by computing respectively the time-correlation functions of the pressure and the entropy fluctuations) that only the adiabatic density fluctuations are responsible for the appearance of the Brillouin doublet. The isobaric density fluctuations are not propagating fluctuations and contribute to a central line without frequency shift. Consequently only the adiabatic compressibility β_s affects BLS intensity. Note that [78,79]

$$\beta_s = 1 / \rho v_l^2, \quad (3.40)$$

where v_l is the longitudinal sound velocity in the scattering medium. Therefore BLS intensity is also a direct indicator of the “hardness” of a material. The intensity ratio of the central line to the Brillouin doublet can be easily calculated,

$$\frac{I_c}{2I_B} = \frac{I_{is}^{iso}}{I_{is}^{ad}} = \frac{\beta_T - \beta_s}{\beta_s} = \frac{\beta_T}{\beta_s} - 1. \quad (3.41)$$

By definition, the specific heat ratio γ is

$$\gamma = \frac{\beta_T}{\beta_S} = \frac{C_P}{C_V}, \quad (3.42)$$

and hence

$$\frac{I_c}{2I_B} = \frac{C_P - C_V}{C_V} = \gamma - 1. \quad (3.43)$$

This ratio, first calculated by Landau and Placzek [80], is called the Landau-Placzek ratio.

3.3 Some remarks

This chapter was devoted to the origin of BLS and its main features. It has to be pointed out that the thermal sound waves responsible for the Brillouin doublet should not be only understood as traveling plane waves (including damped plane waves) with longitudinal polarization as in the usual context of sound. Transverse waves can too lead to the Brillouin doublet, and the Doppler effect explanation works equally well. However, the preceding thermodynamic argument is no longer valid to account for the scattering intensity caused by transverse waves. The dielectric fluctuations now are not caused by density (or pressure) fluctuations, instead, due to the coupling of shear waves to rotation of the molecules which bear more or less some degree of anisotropy. In general, the scattering intensity due to transverse waves is very weak compared to that due to adiabatic density fluctuations. One should also be aware that the previous thermodynamic discussion is only strictly valid for systems in thermodynamic equilibrium.

In complex elastic systems, e.g. systems with elastic inhomogeneities on the scale of the elastic wavelength, wave propagation is far more complicated than in a homogenous isotropic elastic body of infinite size as we have seen in Chapter 2. For propagating modes with different phase velocities, they will be revealed (assuming enough intensity) and distinguished by their different frequency positions in the BLS spectrum. Apparently the Doppler effect is still perfect in explaining the frequency shift. For non-propagating modes (localized due to elastic confinement), it is meaningless to talk about the phase velocity and hence the Doppler effect. In fact, both propagating modes and non-propagating modes are necessary components in synthesizing the complex adiabatic density fluctuations in some complex elastic systems. Obviously the time-dependent localized density fluctuations will be reflected in its Fourier transformation spectrum in the frequency space, as a result they also give rise to the Brillouin doublet at the corresponding frequencies. A simple and vivid way

to appreciate BLS due to non-propagating modes is to again borrow the quantum mechanical concepts. Regardless of the nature of the various modes, either propagating or non-propagating, they can be envisaged as “material vibrations” in analogy with “molecular vibrations” of a molecule. Naturally, the exchange of energy between these “material vibrations” and the incident photons results in frequency shift in the scattered light.

The width of the Brillouin peak reflects the lifetime of the phonon. A number of factors, like sound absorption, phonon scattering, molecular relaxation and so on, can lead to a reduction of the phonon lifetime [81]. The final peak width is an overall effect of all these contributions. Therefore an accurate description of the width requires complete information on all these factors, which is hardly possible in practice. Only in a few simple cases, where one factor dominates, the Brillouin width can be reasonably well captured theoretically. For example, in a Newtonian fluid where the Navier-Stokes equation holds, the Brillouin width Γ is found to be proportional to the square of the scattering wavevector \mathbf{q} [74], that is, $\Gamma \sim q^2$. In general, the spectra obtained experimentally are a convolution of the real spectrum and the instrumental function. In this dissertation, BLS is employed as a tool to reveal the various elastic excitations in the systems of interest, and it is the frequency shift that primarily concerns us. For this reason, in the experimental data analysis deconvolution with the instrumental function is not necessary as the peak frequency is in the first order unaffected.

3.4 Surface BLS

So far we have discussed BLS due to the interaction of the incident photons with the bulk phonons of a material. The scattering mechanism applies as well when coming to the surface (assuming a flat boundary) since the surface phonons do not show essential difference from bulk phonons in terms of their modulation of the local dielectric constant in the near surface region. In this context it is often referred to as the elasto-optic effect. However, there exists another additional mechanism responsible for BLS intensity at the surface. In Chapter 2, we have seen that surface waves, like Rayleigh waves, have a displacement component perpendicular to the surface. This leads to ripples on the surface, and these ripples form a grating which can diffract light. Considering the propagating nature of the surface waves, the grating is indeed a “moving” grating and the Doppler effect is responsible for the frequency shift.

Theoretical calculations show that in general for transparent substances, the elasto-optic effect dominates the scattering intensity by surface phonons, while for opaque substances, the “surface ripple” mechanism takes over [58,82]. Moreover, for opaque samples, the incident light is exponentially attenuated with distance into the substrate and hence has a very small penetrating depth. The momentum conservation condition in BLS is then relaxed, and only the component of the scattering wavevector \mathbf{q} along the surface is conserved [83]. Usually when “surface BLS” is mentioned, it implicitly refers to the scattering from opaque substances in which the “surface ripple” mechanism becomes important.

The work done in this dissertation is only marginally linked to “surface BLS”, or to “surface ripple” scattering. The brief treatment of it is to keep the integrality of the introduction of BLS, and further discussion of it will be excluded.

Chapter 4

Brillouin light scattering instrumentation

4.1 Introduction to Fabry-Perot interferometer

The frequency shift involved in Brillouin light scattering (BLS) generally ranges from 10^9 to 10^{11} Hz. This is rather small compared to the incident laser frequency in the visible spectrum which is on the order of 10^{14} Hz. To achieve such a high spectroscopic resolution the frequently encountered diffraction grating spectrometers widely used in Raman scattering and fluorescence spectroscopy do not suffice. Spectrometers based on the Fabry-Perot (FP) interferometer have to be used. The FP interferometer, providing extremely high resolving power, is the most crucial element of the whole BLS experimental setup. A solid understanding of how a FP interferometer works is necessary to carry out a successful BLS experiment.

4.1.1 Multiple beam interference

The working principle of a FP interferometer is based on multiple beam interference. Consider the simple case of a transparent parallel plate of dielectric material with a refractive index n_f and a thickness d as shown in **Fig. 4.1a**. Suppose that the film is nonabsorbing and let the refractive indices on both sides of the film be equal, namely, $n_1 = n_2$. An incident beam with the amplitude E_0 impinges on the plate at an incident angle θ_i . The amplitude-transmission coefficients are represented by t , the fraction of the amplitude of a wave transmitted on entering into the film, and t' , the fraction transmitted when a wave leaves the

film. The corresponding amplitude-reflection coefficients are denoted by r and r' respectively. In the absence of energy dissipation, we have [84]

$$r = -r' \text{ and } tt' + r^2 = 1. \quad (4.1)$$

Indeed, whenever the amplitude-reflection coefficients, the r 's, are not small, multiple reflections inside the plate will become significant and the final transmission or reflection intensity is determined by the interference of those multiply transmitted or reflected rays. The optical path length difference L between adjacent rays can be easily computed by referring to **Fig. 4.1b**,

$$L = n_f[(\overline{AB}) + (\overline{BC})] - n_1(\overline{AD}). \quad (4.2)$$

By simple trigonometric manipulation and using Snell's law, the expression for L finally becomes

$$L = 2n_f d \cos \theta_t, \quad (4.3)$$

with θ_t being the refractive angle. Accordingly, the phase difference δ between adjacent rays is simply given by $\delta = k_0 L$, where k_0 is the wavenumber of the incident light in vacuum. The total reflected scalar wave E_r is the summation of the externally reflected wave E_{1r} and the large number of higher-order internally reflected waves, $E_{2r}, E_{3r}, E_{4r} \dots$, namely,

$$E_r = E_{1r} + E_{2r} + E_{3r} + \dots + E_{Nr}. \quad (4.4)$$

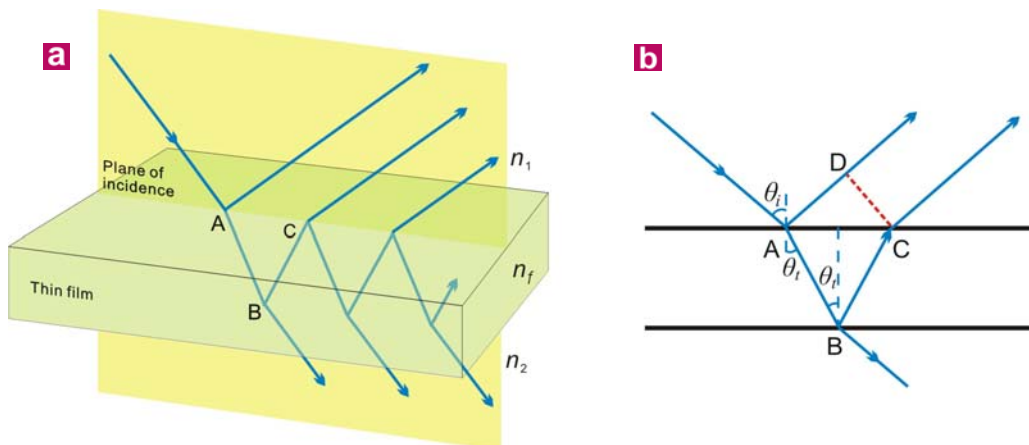


Figure 4.1 Multiple beam interference. **a**, Multiple reflections and transmissions which happen when an light beam is incident onto a dielectric thin film. **b**, Illustration of the optical path length difference between adjacent reflected beams in the plane of incidence.

Assuming $E_0 e^{i\omega t}$ to be the incident wave, the reflected waves, with consideration of the corresponding phase shift, are then given by

$$\begin{aligned} E_{1r} &= E_0 r e^{i\omega t}, \quad E_{2r} = E_0 t r' t' e^{i(\omega t - \delta)}, \quad E_{3r} = E_0 t r' t'^3 t' e^{i(\omega t - 2\delta)}, \dots \\ E_{Nr} &= E_0 t r' t'^{(2N-3)} t' e^{i[\omega t - (N-1)\delta]}. \end{aligned}$$

The addition of these reflected waves ultimately yields,

$$E_r = E_0 e^{i\omega t} \left[\frac{r(1 - e^{-i\delta})}{1 - r^2 e^{-i\delta}} \right]. \quad (4.5)$$

The reflected beam intensity I_r is then $I_r = E_r E_r^* / 2$. Eventually, we obtain

$$I_r = I_i \frac{[2r/(1-r^2)]^2 \sin^2(\delta/2)}{1 + [2r/(1-r^2)]^2 \sin^2(\delta/2)}, \quad (4.6)$$

where $I_i = E_0^2 / 2$ represents the incident beam intensity. Following similar procedures, the transmitted beam intensity is found to be

$$I_t = I_i \frac{1}{1 + [2r/(1-r^2)]^2 \sin^2(\delta/2)}. \quad (4.7)$$

With the definition of the coefficient of finesse F , such that

$$F \equiv \left(\frac{2r}{1-r^2} \right)^2, \quad (4.8)$$

Eq. (4.6) and Eq. (4.7) can be rewritten as

$$\frac{I_r}{I_i} = \frac{F \sin^2(\delta/2)}{1 + F \sin^2(\delta/2)} \quad (4.9)$$

$$\text{and} \quad \frac{I_t}{I_i} = \frac{1}{1 + F \sin^2(\delta/2)}. \quad (4.10)$$

The term $\left[1 + F \sin^2(\delta/2) \right]^{-1} \equiv A(\vartheta)$ is known as the Airy function. It represents the transmitted light intensity distribution as a function of the phase difference between adjacent beams and is plotted in **Fig. 4.2**.

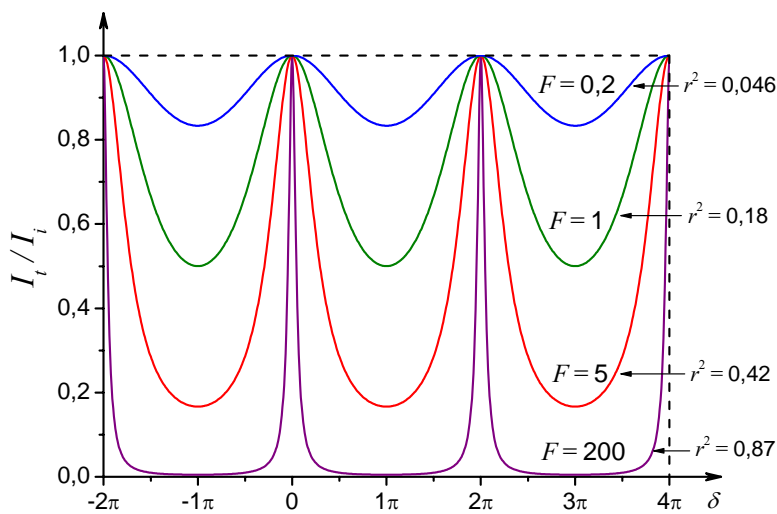


Figure 4.2 Airy function.
Examples of Airy functions with different F values. Sharp transmission happens only with large F .

It is clear that as F increases, the transmitted light intensity decreases. When r , the amplitude-reflection coefficient, approaches 1, F approaches infinity. The transmitted intensity then becomes very small, except within the sharp spikes centered about the points $\delta/2 = m\pi$, $m = 1, 2, 3, \dots$. In fact, this very strict condition (for large F) for transmission lays the theoretical foundation for constructing devices utilizing multiple beam interference to attain high spectroscopic resolving power.

4.1.2 Standard Fabry-Perot interferometer

The FP interferometer is a multiple beam interferometer of considerable contemporary interest, first constructed by Charles Fabry and Alfred Perot in the late 1800s. Besides being a spectroscopic device of extremely high resolving power, it serves as the basic laser resonant cavity. The simplest configuration consists of two plane, parallel, and highly reflected surfaces separated by some distance d as shown in **Fig. 4.3**. If the enclosed gap (usually air) can be mechanically varied by moving one of the mirrors, it is referred to as an interferometer. When the mirrors are held fixed and adjusted only for parallelism, it is called an etalon (although the latter is still an interferometer in the broad sense).

In practice, two semisilvered or aluminized glass optical flats form the reflecting boundary surfaces. The introduction of a thin metal layer is to increase the reflectivity, as we have seen already that high resolving power can only be achieved with large r . In the

absence of light absorption, the equation $tt' + r^2 = 1$ holds. Since in most cases it is the reflected and transmitted beam intensity that are concerned, another two useful parameters are defined, the reflectance R , the reflected fraction of the incident intensity, and the

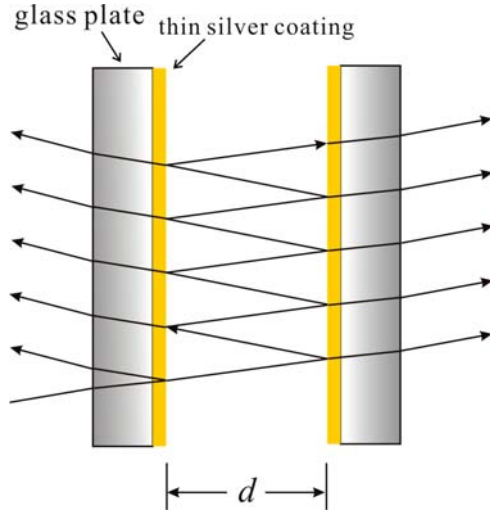


Figure 4.3 Fabry-Perot etalon.

transmittance T , the transmitted fraction of the incident intensity. It can be easily shown that $R = r^2$. Following the energy conservation, obviously we have $R + T = 1$. In reality, there is always some loss of energy, e.g. transformation to heat. If the absorbed fraction, referred to as the absorptance, is denoted by A , the above relation then becomes $R + T + A = 1$.

The appearance of A will not change the essential physics of multiple beam interference discussed in the last section, yet it affects the transmitted intensity. With the

presence of A , Eq. (4.10) is changed to

$$\frac{I_t}{I_i} = \left[1 - \frac{A}{(1-R)} \right]^2 A(\mathcal{G}). \quad (4.11)$$

Apparently, if $A=0$, the above equation reduces to Eq. (4.10); if A is nonzero, the transmitted intensity maxima $(I_t)_{\max}$ will always be somewhat smaller than I_i . However, the relative transmitted intensity is still determined by the Airy function, since

$$\frac{I_t}{(I_t)_{\max}} = A(\mathcal{G}). \quad (4.12)$$

Of great importance is the sharpness of the transmitted “peak” in **Fig. 4.2**, that is, how rapidly the intensity drops off on either side of the maximum. This is described by γ , the width at half-maximum, as indicated in **Fig. 4.4**. The value of γ can be readily calculated, e.g. by considering the peak centered at $\delta_{\max}=0$, in this case, $\gamma = 2\delta_{1/2}$, where $\delta_{1/2}$ is the value of δ when $(I_t)_{\max}=2I_t$. It follows that $\delta_{1/2} = 2\sin^{-1}(1/\sqrt{F})$. Since F is generally rather large, $\sin^{-1}(1/\sqrt{F}) \approx 1/\sqrt{F}$, hence

$$\gamma = 4/\sqrt{F}. \quad (4.13)$$

This width, to a very good approximation, represents the smallest phase increment separating two resolvable peaks, which actually determines the resolving power of a FP interferometer. Another quantity of particular interest is the ratio of the separation of adjacent maxima to the peak width at half-maximum, known as the finesse \mathcal{F} . Obviously, $\mathcal{F} = 2\pi / \gamma$, from Eq. (4.13),

$$\mathcal{F} = \frac{\pi\sqrt{F}}{2}. \quad (4.14)$$

Over the visible spectrum, the finesse of most ordinary FP instruments is about 50. In practice, the finesse cannot be made much greater than about 100 due to

limitations on the quality of mirror substrates and coatings, as well as deviations of the mirrors from plane parallelism. Note that as the finesse increases, the width at half-maximum decreases. Thus the resolving power becomes higher, but at the expense of the transmission intensity.

The FP interferometer is used as a high resolving power spectrometer by varying the spacing d (**Fig. 4.3**) between the two mirrors so as to select light transmission at different wavelengths. Recall that the maximum transmission happens at $\delta/2 = (k_0 L/2) = m\pi$, $m = 1, 2, 3, \dots$. Referring to Eq. (4.3), we have

$$m\lambda_0 = 2n_f d \cos \theta_t, \quad (4.15)$$

where $\lambda_0 = 2\pi/k_0$ is the wavelength of light in vacuum. For nearly normal incidence, $\cos \theta_t = 1$, then

$$m\lambda_0 = 2n_f d. \quad (4.16)$$

We realize immediately that for a given spacing d , the transmitted light does not necessarily have the same wavelength because the change in wavelength can be compensated by the corresponding change in the integer number m . This makes an unambiguous interpretation of the spectrum impossible, unless it is known a priori that the spectrum of interest entirely falls

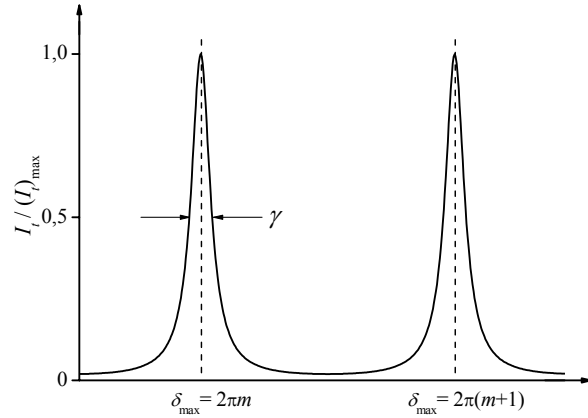


Figure 4.4 Fabry-Perot fringes and the finesse.

into a certain wavelength span $(\Delta\lambda_0)_{\text{FSR}}$, the so-called free spectral range (FSR). For a fixed d , differentiating Eq. (4.16) leads to

$$\frac{(\Delta\lambda_0)}{\lambda_0} = -\frac{\Delta m}{m}. \quad (4.17)$$

The minus is irrelevant since it means only that the order increases when λ_0 decreases. The separation between the two adjacent transmission maxima (**Fig. 4.4**) is 2π , and the corresponding change of m is 1, namely, $\Delta m=1$. Therefore, Eq. (4.17) becomes

$$\frac{(\Delta\lambda_0)_{\text{FSR}}}{\lambda_0} = \frac{1}{m}. \quad (4.18)$$

In combination with Eq. (4.16), we have

$$(\Delta\lambda_0)_{\text{FSR}} = \lambda_0^2 / 2n_f d, \quad (4.19)$$

or in terms of frequency

$$(\Delta f)_{\text{FSR}} = c / 2n_f d, \quad (4.20)$$

where c is the speed of light in vacuum. The FSR is a very important instrumental parameter to be set before using the FP interferometer for spectroscopic purposes.

4.1.3 Tandem Fabry-Perot interferometer

It was early recognized in the field of Brillouin scattering that the standard FP interferometer has too low a contrast to allow weak Brillouin signals to be observed in the presence of normally extremely intense elastically scattered light. This problem was not really solved until 1971 when the high contrast, multipass FP interferometer was introduced by Sandercock [85]. However, a multipass FP interferometer, like the simple configuration, still suffers from the overlapping of neighboring interference orders, which makes the interpretation of the measured spectra somewhat ambiguous, especially for rich or broad spectral features.

One solution to suppress this effect is to use a tandem arrangement, i.e. two FP interferometers (FP1 and FP2) in series with slightly different FSR. In this case, the neighboring order transmission peaks of the two FP interferometers cannot coincide due to the slight difference in their FSR as illustrated in **Fig. 4.5**. As a result, the adjacent

interference orders of one of the two interferometers are blocked by the other, leading to a significant suppression of interference higher order transmission. In order for the tandem interferometer to function as a spectrometer, the wavelengths transmitted by the two FP combinations must satisfy the following two equations simultaneously for all wavelengths within the relevant FSR,

$$\begin{aligned} m_1 \lambda_0 &= 2n_f d_1 \quad (\text{for FP1}), \\ m_2 \lambda_0 &= 2n_f d_2 \quad (\text{for FP2}). \end{aligned} \quad (4.21)$$

This implies that the scanning of the two FP interferometers has to be synchronized, such that,

$$\frac{\Delta d_1}{\Delta d_2} = \frac{d_1}{d_2}. \quad (4.22)$$

However, for quite a long time, this seemingly simple relation remained the biggest obstacle to the practical realization of the tandem FP interferometer. This difficulty was removed in the 1980s by Sandercock [86] who proposed a very simple but elegant solution based on a novel design of the scanning stage. The principle of the tandem scan is demonstrated in **Fig. 4.6**. The first interferometer FP1 is arranged to lie in the direction of the translation stage movement. One mirror sits on the translation stage, the other on a separate angular orientation device. The second interferometer FP2 lies with its axis at an angle φ to the scan direction. One mirror is mounted on the translation stage and the other mirror on an angular orientation device which can also allow a small translation of the mirror for adjustment purposes. The relative spacings of the mirrors are set so that a movement of the translation stage to the left would bring both sets of mirrors into simultaneous contact. A movement of the translation stage to the right then sets the spacings to d_1 and $d_1 \cos \varphi$. Moreover, a scan Δd_1 of the translation stage produces a change of spacing Δd_1 in FP1 and $\Delta d_1 \cos \varphi$ in FP2. In other words, Eq. (4.22) is satisfied.

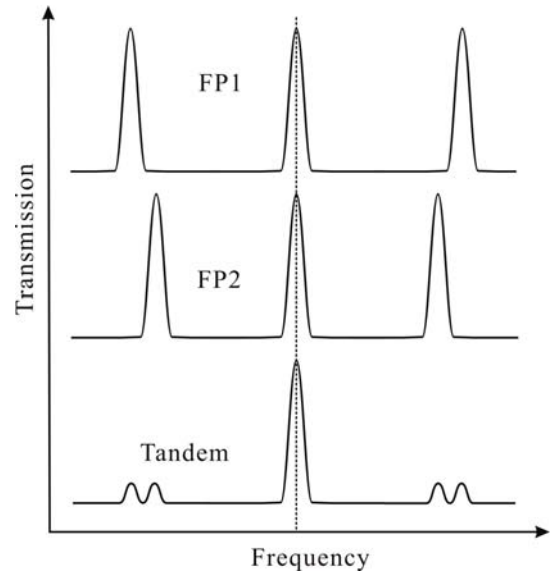


Figure 4.5 Suppression of higher order transmission in a tandem Fabry-Perot.

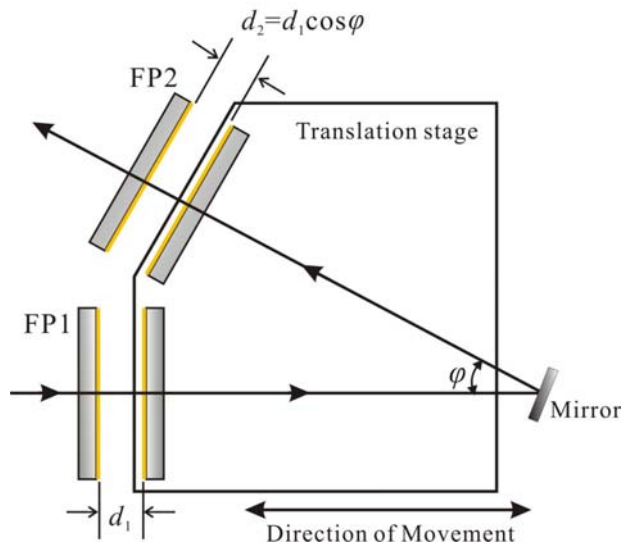


Figure 4.6 Principle of the tandem scanning of a tandem Fabry-Perot.

In my experiment, a six-pass tandem Fabry-Perot was used and the related tandem optics is briefly sketched in **Fig. 4.7**. The scattered light enters the system at the adjustable pinhole P1. Mirror M1 reflects the light towards the lens L1 where it is collimated and directed via mirror M2 to the first interferometer FP1. Then the light hits mirror M3 and is directed to the second interferometer FP2. After transmission through FP2 the light strikes the 90° prism PR1 where it is reflected downwards and returned parallel to itself towards FP2. Upon the reflection by M3 it continues to pass through FP1, after transmission through lens L1 it travels underneath mirror M1 and is focused on to mirror M4. This mirror returns the light through lens L1 where it is again collimated and directed through FP1. The combination of lens L1 and mirror M4 lying at its focus acts as a spatial filter which filters out unwanted beams such as the beam reflected from the rear surfaces of the interferometer mirrors. After the final pass through FP2, the light strikes mirror M5 where it is directed to the prism PR2. This prism, in combination with the mirror M6, the lens L2 and the output pinhole P2, forms a bandpass filter with a width determined by the size of the pinhole.

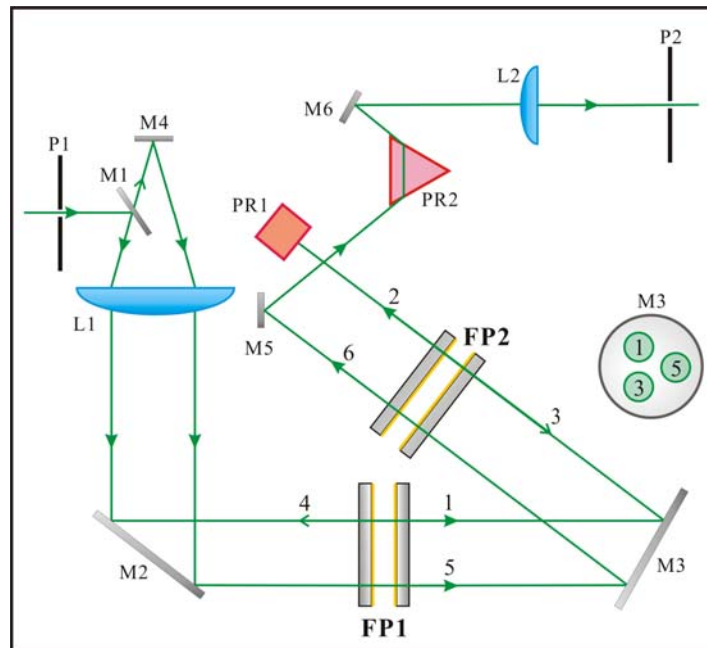


Figure 4.7 Optics inside a six-pass tandem Fabry-Perot interferometer. *The scattered light enters the tandem system via the pinhole P1 and leaves via the pinhole P2. Before it finally reaches the photodetector, the scattered light passes the two interferometers (FP1 and FP2) six times.*

4.2 Experimental setup

The whole BLS experimental setup is schematically shown in **Fig. 4.8**. A solid state diode pumped, frequency-doubled Nd:YAG laser (Coherence) with an output power of 100 mW (532 nm) is mounted on the rotatory arm of a goniometer (Huber). After passing through a Glan polarizer, the outgoing laser beam with polarization (V) perpendicular to the scattering plane (horizontal plane) is focused into the center of the goniometer where the sample is located. The focusing size is around 200 μm in diameter. The scattered light along a well-defined direction is collected by an aperture and focused into the entrance pinhole of the tandem Fabry-Perot (JRS Scientific Instruments) after successive transmission through two lenses. A Glan-Thompson analyzer is inserted between the two confocal lenses to allow the selection of the scattered light with polarization either perpendicular (V) or parallel (H) to the scattering plane. After passing through the tandem Fabry-Perot which acts as a spectrometer, the scattered light is detected by a single-photon avalanche photodiode (APD). The resulting electronic signal is processed by a multi-channel analyzer (MCA). A tiny

fraction of the incident laser intensity is separated from the incident beam and introduced as a reference beam via an optical-fiber into the tandem Fabry-Perot to achieve a long period (up to several weeks) stabilization of the interferometer. The experimental change of the scattering angle θ , hence the scattering wavevector \mathbf{q} , is accomplished by rotating the goniometer with an electronically controlled motor, which can cover a broad θ range, roughly from 8° to 160° .

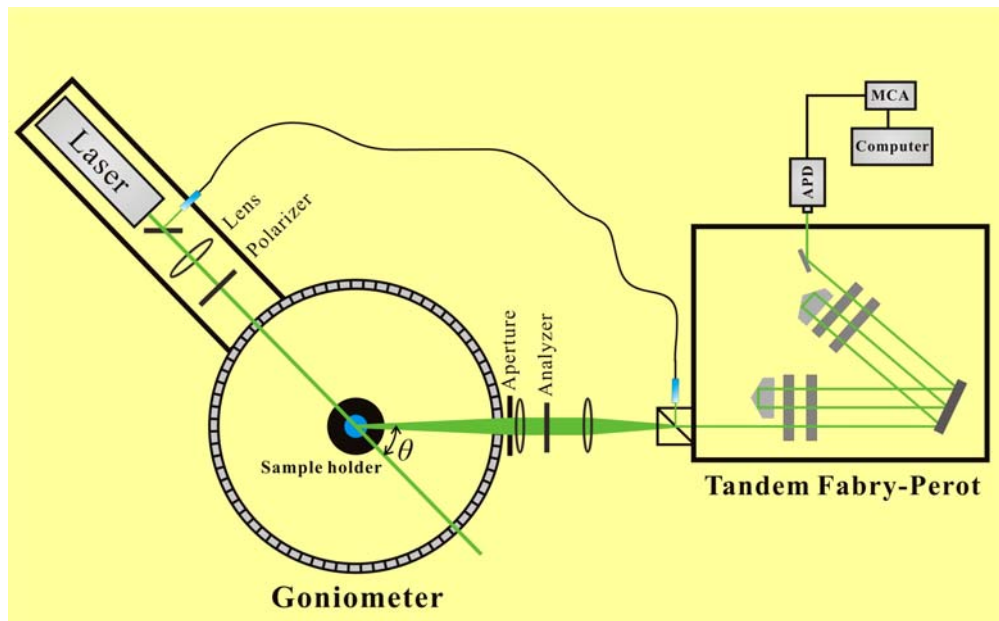


Figure 4.8 Scheme of the BLS setup. *The sample is sitting at the center of the goniometer, the variation of the scattering angle θ is realized by rotating the laser mounted on the goniometer. The scattered light is collected by two lenses into the six-pass tandem Fabry-Perot interferometer.*

The sample holder used allows BLS measurements at elevated temperatures up to 453 K. This feature is important for investigating the temperature dependence of BLS in some polymer samples, especially effects related to the glass transition. As seen in **Fig. 4.9**, the holder is cylindrical-shaped and has a metallic body. A flat, wide-open slit with a width of 1 cm is made out of the body at the appropriate height, allowing the transmission of the incident laser beam and the emanation of the scattered light. A transparent, round quartz wall with intimate contact to the inner wall of the metallic body is inserted inside the holder to make the inside a closed system necessary for good temperature control. With a special adapter, the sample is brought to a proper height in the center of the holder, and a cover lid is used to enclose the interior. The system is electrically heated, with a Pt100 temperature

sensor embedded in the metallic body to regulate the heating behavior. Another Pt100 sensor is placed in close proximity to the sample to read the sample temperature. The temperature of the system is stabilized within ± 0.2 K.

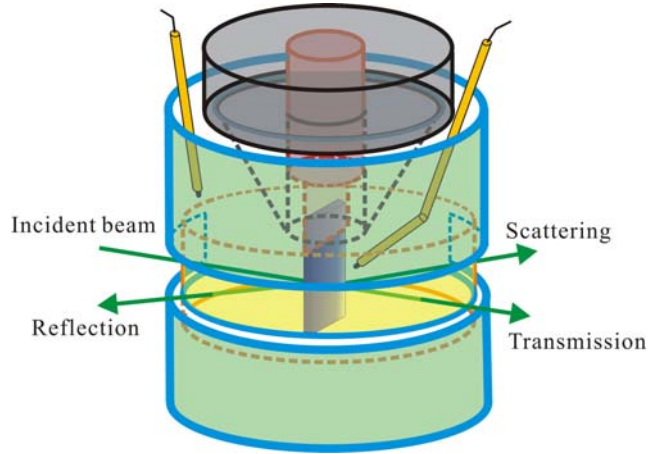


Figure 4.9 The sample holder allowing BLS experiment to be performed at elevated temperatures.

4.3 Scattering geometry

The scattering geometry is another important BLS experimental issue deserving special attention. In fact the scattering geometry is to a large extent determined by the geometrical characteristics of the sample. Usually two well-defined sample forms are utilized in BLS experiments: the cylinder and the film. In the following discussion of the scattering geometry, we confine ourselves to the situation that the rotation axes of the cylinder and the film plane are perpendicular to the scattering plane.

1. scattering geometry for a cylindric sample

This is the simplest scattering geometry encountered in a BLS experiment. Samples of such a form are generally liquids filled in transparent cylindrical glassware, e.g. a NMR tube. The scattering wavevector \mathbf{q} has a magnitude $q = \frac{4\pi n}{\lambda_0} \sin \frac{\theta}{2}$, as evidenced in **Fig. 4.10**, where n is the refractive index of the scattering medium.

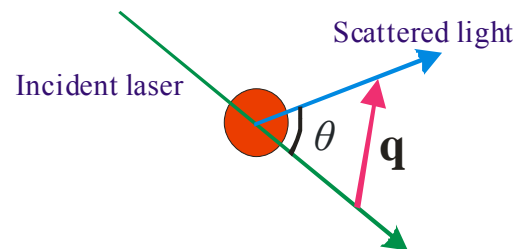


Figure 4.10 BLS scattering geometry for a cylindric sample.

2. scattering geometry for a film sample

When dealing with solid samples, in most cases a film with a refractive index n is used, either free-standing or supported. In this case, complication in the calculation of \mathbf{q} comes from the refraction at the sample surface. Depending on the relative position of the incident beam and the scattered beam with respect to the film plane, the scattering geometry for a film can be further divided into two classes: the transmission geometry, in which the incident and the scattered beam lie at different sides of the film plane, and the reflection geometry, in which the incident and the scattered beam are on the same side of the film plane.

The transmission geometry is shown in **Fig. 4.11a**. For a defined scattering angle θ , the scattering wavevector \mathbf{q} is not yet well defined since the orientation of the film can be varied. In other words, the incident angle α still has freedom to change. What really matters in determining \mathbf{q} are the wavevectors of the incident and the scattered beams inside the film, both of which are functions of θ and α . After simple trigonometric manipulation and applying Snell's law, one obtain

$$q = \frac{4\pi n}{\lambda_0} \sin \left[\frac{1}{2} \left[\text{Arc sin} \left(\frac{1}{n} \sin(\theta + \alpha) \right) - \text{Arc sin} \left(\frac{1}{n} \sin \alpha \right) \right] \right] \quad (4.23)$$

$$\text{and } q_{\text{para}} = \frac{4\pi n}{\lambda_0} \cos \left[\frac{1}{2} \left[\text{Arc sin} \left(\frac{1}{n} \sin(\theta + \alpha) \right) + \text{Arc sin} \left(\frac{1}{n} \sin \alpha \right) \right] \right]. \quad (4.24)$$

in which θ ranges from 0° to 180° and α is between -90° and 90° . Note that α is negative when the rotation from the surface normal to the incident beam is clockwise as in **Fig. 4.11a**. The quantity q_{para} is the component of \mathbf{q} along the film plane, the ratio of q_{para}/q reflects the relative direction of \mathbf{q} with respect to the film plane. It can be shown that this ratio in most cases is more than 0.9. Therefore when the transmission geometry is adopted, BLS is mainly used to study phonon propagation parallel to the film plane.

The reflection geometry is depicted in **Fig. 4.11b**. Following similar simple trigonometric procedures, q and q_{para} can be found to be

$$q = \frac{4\pi n}{\lambda_0} \cos \left[\frac{1}{2} \left[\text{Arc sin} \left(\frac{1}{n} \sin(\theta + \alpha) \right) + \text{Arc sin} \left(\frac{1}{n} \sin \alpha \right) \right] \right] \quad (4.25)$$

$$\text{and } q_{\text{para}} = \frac{4\pi n}{\lambda_0} \sin \left[\frac{1}{2} \left[\text{Arc sin} \left(\frac{1}{n} \sin(\theta + \alpha) \right) - \text{Arc sin} \left(\frac{1}{n} \sin \alpha \right) \right] \right]. \quad (4.26)$$

It is remarkable that the expression of q in the reflection geometry is the same as the expression of q_{para} in the transmission geometry, and vice versa. However, for a given combination of θ and α , there can be only one scattering geometry. The transmission and the reflection scattering geometries cannot exist simultaneously. Therefore when using the above expressions for the calculation of \mathbf{q} , care has to be taken to first identify which scattering geometry is used. The most distinct feature of the reflection geometry is that the direction of \mathbf{q} is very close to the film normal, thus this geometry is chosen when phonon propagation along the film normal needs to be studied.

3. A special scattering geometry

In my experiment, transparent solid samples in the form of a film were almost exclusively used. Of the two scattering geometries for film samples, the transmission geometry was the one selected for most of the studies because the reflection geometry can only provide a very small range of q so that the dispersion relation of the phonon propagation cannot be attained. For the transmission geometry, when $\alpha = -\theta/2$, that is, the incident angle is half of the scattering angle (notice the sign convention for the incident angle), Eq. (4.23) can be simplified to

$$q = \frac{4\pi}{\lambda_0} \sin \frac{\theta}{2}. \quad (4.27)$$

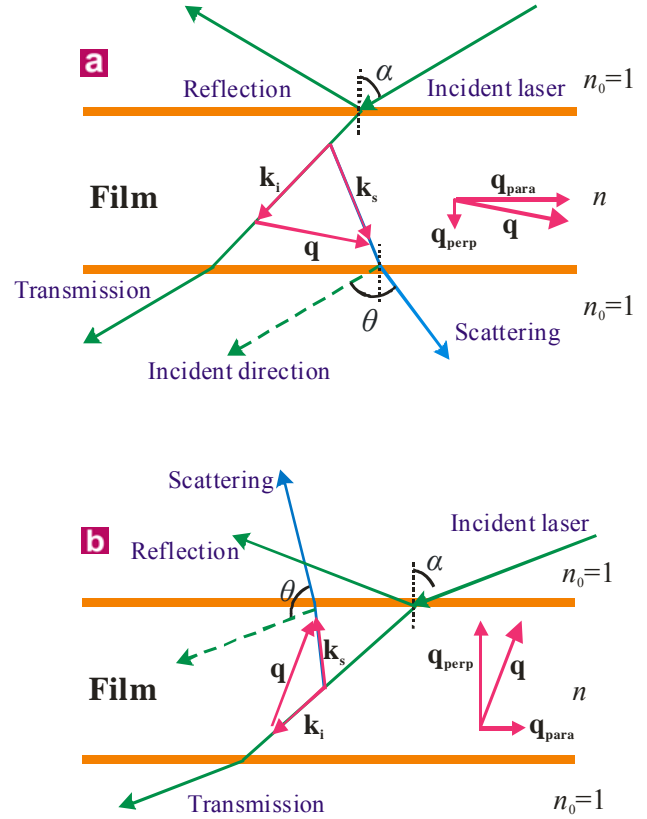


Figure 4.11 BLS scattering geometry for a film sample. **a**, Transmission case. **b**, Reflection case.

We can see that q is now independent of the refractive index n , a quantity which is not always available. Moreover, under such a condition the ratio q_{para}/q is equal to 1. Hence q is

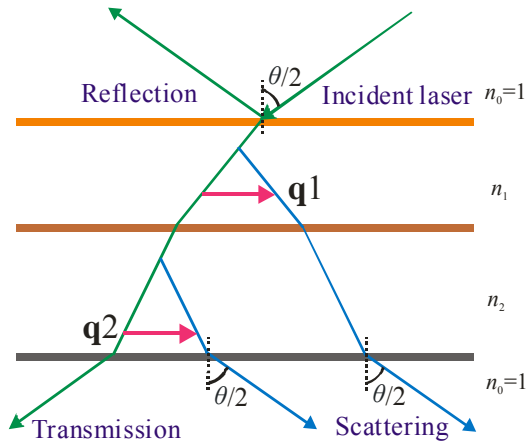


Figure 4.12 A special BLS scattering geometry for a bilayer film. The incident angle with respect to the film normal is half of the external scattering angle, and q does not depend on the refractive indices of the layers.

strictly parallel to the film plane, which is ideal for the investigation of in-plane phonon propagation. It is easy to verify that Eq. (4.27) holds not only for a single film but also for bilayer and even multilayer films, making this special scattering geometry of great practical importance since very often we deal with films with many layers. For example, a supported single film is actually a bilayer system considering the presence of the substrate. In **Fig. 4.12**, this special scattering geometry applied to a bilayer film is schematically sketched. Despite the

refractive index difference between the two constituent layers, the scattering wavevectors q_1 and q_2 in the two layers are equal. The generalization to more layers is straightforward.

Chapter 5

Elastic excitations in supported thin polymer films

5.1 Introduction

Brillouin light scattering (BLS) capable of probing elastic wave propagation has been demonstrated to show great potential to extract the elastic information of thin polymer films. For supported thin layers, no noticeable change in elastic moduli has been found with thickness down to about 150 nm [24]. Although a substrate is also present, its influence on the elastic wave propagation is well defined, in contrast to some other nanomechanical methods like nanoindentation or atomic force microscopy (AFM). Moreover, due to the strong dependence of the speed of elastic waves on the elastic moduli of the film, which in turn are sensitive to the free-volume of the polymer, temperature-dependent BLS has been successfully applied to extract the T_g of free-standing thin polymer films [11,18]. In fact, original information about the dimension-dependent T_g of free-standing thin polymer films was exclusively obtained by BLS. Despite the apparent virtue of BLS of being able to obtain the elastic properties and T_g simultaneously, the determination of T_g by BLS has been so far only restricted to free-standing thin films. The hindrance of applying BLS to supported thin films for this purpose comes from the negative impact from the substrate. For opaque substrates, e.g. silicon wafers which are often used, there is an appreciable laser heating effect which complicates the determination of T_g [11]. On the other hand, it has been pointed out that large amount of light scattering from bulk phonons in transparent substrates would obscure the much weaker signal from the film-guided acoustic modes [11]. As a result,

the few existing BLS measurements on the mechanical properties of thin supported films were all conducted with the use of opaque substrates [24,26].

It is the supported thin films that are widely used technologically. In addition, the overwhelming majority of the T_g measurements on thin polymer films using different techniques are dealing with supported films [10,12-15,17,19]. Therefore it is highly desirable to integrate, for supported thin polymer films, the determination of the elastic constants and T_g . In this chapter, it will be shown that with the use of the previously introduced high-resolution six-pass tandem Fabry-Perot interferometer (Section 4.1.3) and by employing a transmission scattering geometry (Section 4.3), one can overcome the above-mentioned difficulties and successfully extend the BLS determination of the elastic constants to thin polymer films on transparent substrates. A systematical check of the elastic constants of thin supported polymer films was made over a large thickness range, from about 40 nm to 500 nm. As a natural consequence of this progress, BLS measurement of the T_g of supported thin polymer films was demonstrated to become feasible, further enriching the tools for studying the glass transition under confinement conditions.

5.2 Experimental

5.2.1 Sample preparation

The thin supported films were prepared by my collaborator Anna V. Kiyanova at University of Wisconsin. Two glass-forming polymers, polystyrene (PS) and poly(methyl methacrylate) (PMMA) with narrow molecular weight distribution, were used in this study. PS ($M_w=61800$, $M_w/M_n=1.03$) and PMMA ($M_w=62500$, $M_w/M_n=1.04$) were purchased from Polymer Source Inc. Microscope cover slides made by optical borosilicate glass were used as substrate (Fisherbrand 25CIR1D), and cleaned before use by oxygen plasma in PE-200 Oxygen Plasma Surface Treatment and Etching System (Plasma Etch) at 50 cm³/min oxygen flow and 250 W radio frequency power for 10 min.

Thin supported films of PS and PMMA were fabricated by spin-coating of their solutions in toluene on glass substrates at 2000 round/min for 1 min. Thin films with thickness in the range of about 40-500 nm were prepared by using different polymer solution concentrations (1-8 wt%), as listed in Table 5-I. The solutions were filtered through 0.2 μ m

pore size filters prior to spin-coating. After spin-coating, all films were annealed in a custom-made vacuum furnace at 423 K for 10 h. Nominal residual gas pressure in the furnace was about 133 Pa, and the cooling rate after annealing was about 20 K/h.

Table 5-I: sample information

Polymer film	wt% polymer concentration	Spinning speed (round/min)	Spinning time (min)	Film thickness h (nm)	Deviation (nm)
PS-39	1.03	2000	1	39.3	0.3
PS-110	2.35	2000	1	109.8	0.9
PS-322	5.23	2000	1	322.2	2.3
PS-514	7.22	2000	1	514.5	12.3
PMMA-41	1.15	2000	1	40.9	0.3
PMMA-110	2.43	2000	1	110.3	1.2
PMMA-320	5.93	2000	1	320.4	2.7
PMMA-492	7.94	2000	1	491.7	9.8

5.2.2 Film characterization

Film thickness was measured by a three-wavelength nulling ellipsometer (AutoELII-NIR-3) on samples fabricated using the same procedure and sample solutions as stated above, except that piranha solution (4:1(v/v) of 98% H₂SO₄/30% H₂O₂) cleaned silicon wafers were used in place of glass slides. The ellipsometric results were verified by X-ray reflectometry and scanning confocal microscopy on the very samples on glass substrate for the BLS measurement. The thickness values and estimated deviations are listed in Table 5-I. X-ray reflectometry (surface XRD-TT3003 diffractometer, SEIFERT) was used to measure the films with thickness below 120 nm. The thickness can be obtained by fitting the measured reflectivity curve that shows oscillatory decay due to Bragg reflection, as shown in **Fig. 5.1a** for the PS-39 film. For films with thickness above 120 nm, a scanning confocal microscope (Nanofocus AG μ Surf) equipped with rotating Nipkow disk was employed to directly measure the depth of a scratch on the film made by a sharp needle tip, as illustrated in **Fig. 5.1b** for the PMMA-492 film. The depth profile in **Fig. 5.1b** corresponds to the cross section indicated by the red line in the inset, and the thickness was obtained by averaging over the whole sampled area. The surface quality of these films is high, as indicated by the tapping mode AFM (Digital instruments Dimension 3100) image for the PMMA-41 film in **Fig. 5.1c**.

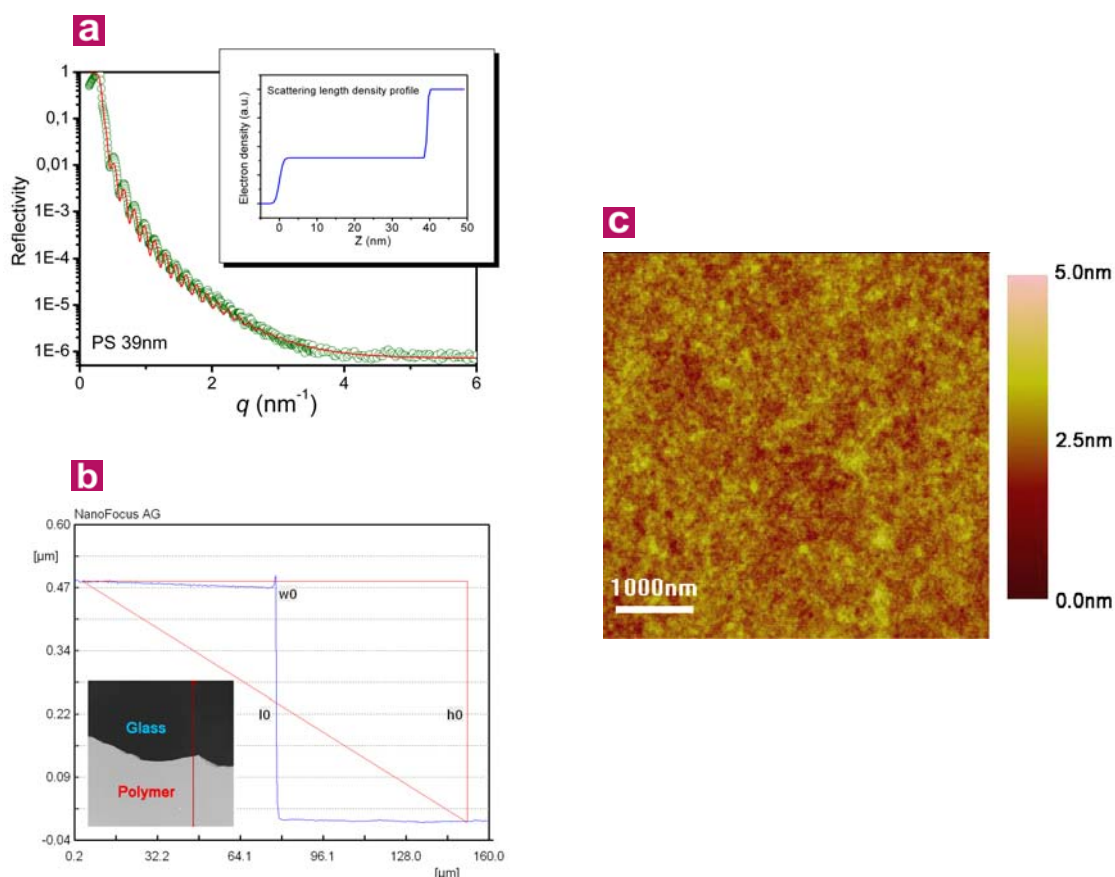


Figure 5.1 Film thickness and surface quality characterization. **a**, The reflectivity curve measured by X-ray reflectometry for the PS-39 film. The green open circles are the experimental points and the red curve is the fit, the corresponding scattering length density profile is given in the inset. **b**, The thickness measurement of the PMMA-492 film using scanning confocal microscopy. The depth profile is along the direction indicated by the red line in the inset, clearly revealing the sudden jump in height due to the scratch made by the needle tip. **c**, Tapping mode AFM image of the PMMA-41 film manifests rather smooth film surface.

For the BLS measurement, the special transmission scattering geometry (**Fig. 4.12**) discussed in Section 4.3 was used. The accumulation time for one spectrum was film thickness dependent, typically 1 h for the thickest film and 10 h for the thinnest film in order to achieve good signal-to-noise ratio. At room temperature, for each film spectra at different q were recorded to map the dispersion relation. The T_g measurement was performed at a fixed q in air with the use of the sample holder described in **Fig. 4.9** and the temperature was increased by multiple steps from room temperature to about 403 K. The effective heating rate was 1 K/min, and the sample was kept for 10 min at each temperature before starting the BLS measurement.

5.3 Results and discussion

5.3.1 Elastic constants

Figure 5.2a and **b** display the room temperature polarized BLS spectra of the PS and PMMA films with two extreme thicknesses, recorded at $q=0.0167 \text{ nm}^{-1}$. The spectra are shown in logarithmic intensity scale to reveal better both the strong and weak spectral features. For a better visualization, the central elastic feature due to the reference beam was omitted over the frequency range $\pm 3.0 \text{ GHz}$ around $f=0 \text{ GHz}$. The very intense peak centered at about 15 GHz in all spectra is due to the strong light scattering from the bulk longitudinal phonon with wavenumber $q=0.0167 \text{ nm}^{-1}$ in the glass substrate. The frequency of the glass peak could act as an internal standard for the scattering wavevector \mathbf{q} . The excellent reproducibility of the glass peak frequency in **Fig. 5.2a** and **b** indicates the well-defined scattering geometry in my experiment. Besides the intense glass peak, other weaker spectral features are also clearly present in the spectra, even for the film thickness down to 40 nm, which are due to the scattering of light by the film-guided phonons propagating parallel to the film-substrate interface. The presence of these film-guided modes clearly indicates that the study of elastic excitations in thin supported polymer films on transparent substrate by BLS is possible in spite of the existence of strong light scattering from the substrate.

The spectra in **Fig. 5.2a** and **b** were recorded with FSR (free spectral range) 30 GHz. Often higher resolution FSR was used to better resolve some closely spaced spectral features. For example, the spectrum of the PMMA-492 film measured at $q=0.0167 \text{ nm}^{-1}$ using 15 GHz FSR reveals five peaks as indicated in **Fig. 5.2c**, but only three peaks are resolved in the spectrum of **Fig. 5.2b** with 30 GHz FSR. In general, the identification of the various modes needs to follow their frequency dependence on phonon wavenumber, namely, the dispersion relation (f versus q). **Figure 5.2d** gives an example of the experimental dispersion relation for the PMMA-492 film. The frequency values were obtained by fitting the peaks with Lorentzian functions with a program developed in house. As expected, these film-guided modes are dispersive, in other words, a simple linear q dependence of the phonon frequency $f = cq/2\pi$ is not satisfied, here c is the frequency-independent phonon phase velocity. Their frequencies roughly fall between the frequencies of the transverse phonons in bulk PMMA and glass, as indicated by the two dashed lines in **Fig. 5.2d**.

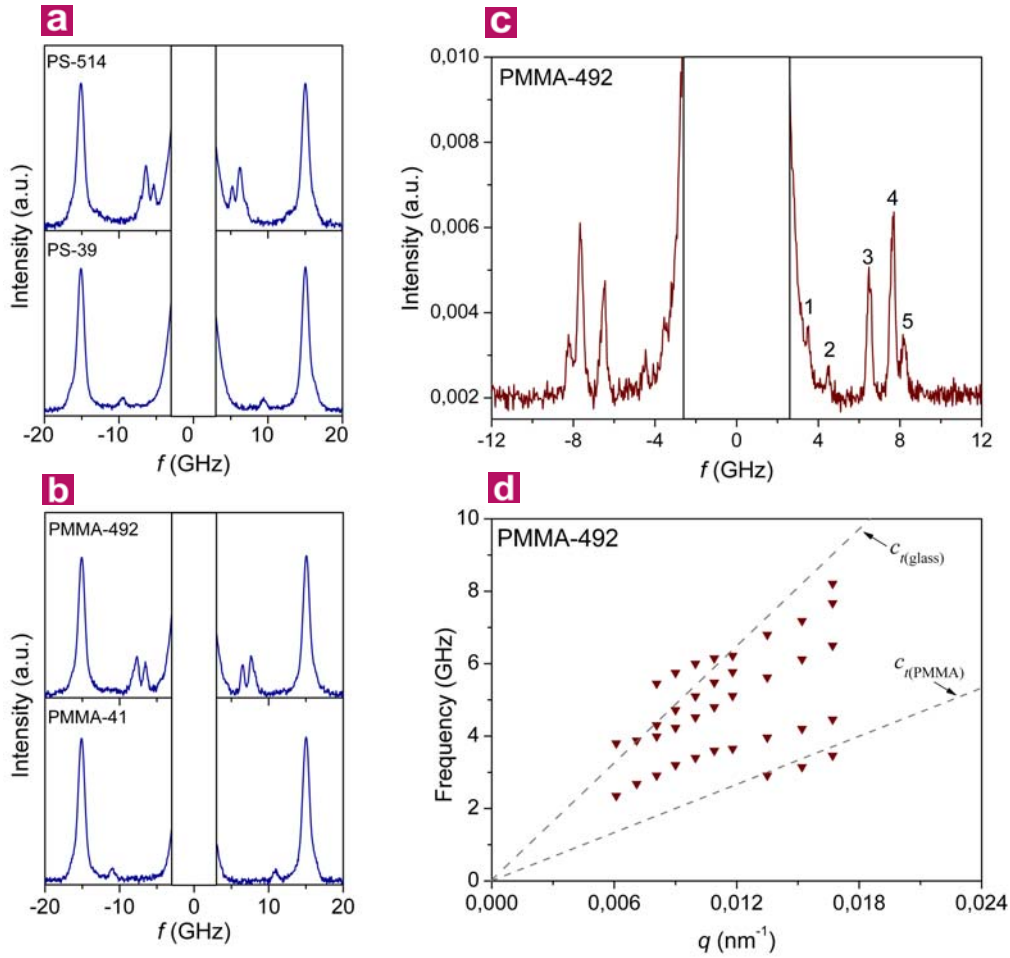


Figure 5.2 BLS spectra of glass substrate supported PS and PMMA thin films. **a,b**, BLS spectra of the PS-514 and PS-39 films (**a**) and of the PMMA-492 and PMMA-41 films (**b**), measured at $q=0.0167 \text{ nm}^{-1}$ with 30 GHz FSR. The intense peak centered at around 15 GHz corresponds to the longitudinal phonon in the glass substrate. The logarithmic intensity scale is used for better revealing both the strong and weak spectral features. **c**, BLS spectrum of the PMMA-492 film measured at $q=0.0167 \text{ nm}^{-1}$ using 15 GHz FSR. This high-resolution spectrum resolves five peaks denoted by the numbers on top of the peaks, in contrast to the three discernable peaks in (**b**). **d**, An example of the measured dispersion relation for the PMMA-492 film, where a linear f dependence on q is lacking. The two dashed lines indicate the transverse phonons in bulk PMMA and glass, respectively.

In the case of thin films, it is customary to demonstrate the dispersion relation in terms of phase velocity c versus qh , the product of the phonon wavenumber and the film thickness. This is because for a certain material combination, the phase velocity of a given mode is only a function of qh , as pointed out in Section 2.3. **Figure 5.3a** and **b** present the measured dispersion relations (the square and circle symbols) in terms of $c \sim qh$ for all the prepared four PS and PMMA films, respectively. At the same qh value, data points measured from different films show very good superposition in the $c \sim qh$ plot, suggesting the very close

elastic properties of these thin films. To theoretically identify the nature of the observed modes, the newly developed layer-multiple-scattering method (LMS) mentioned in the end of Chapter 2 was employed. In the next paragraph, we digress for a moment to briefly introduce this method.

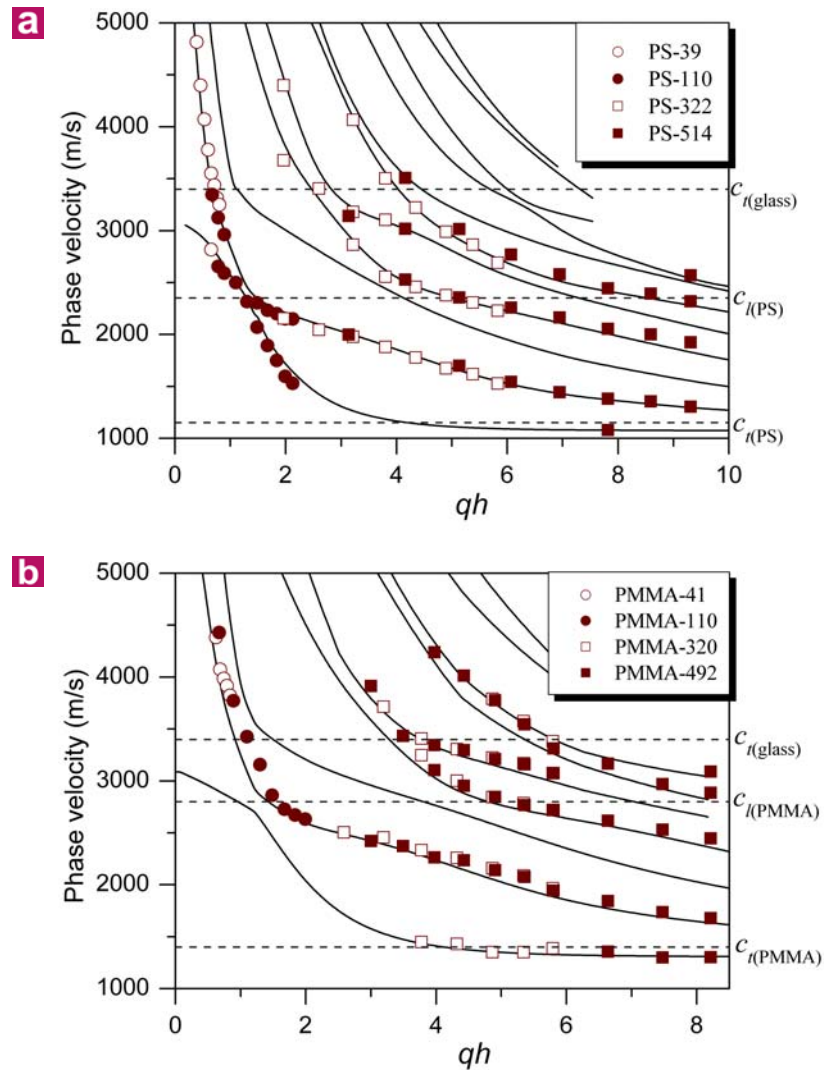


Figure 5.3 Dispersion relations of film-guided elastic waves in the supported PS and PMMA thin films. **a,b,** *Experimental and theoretical dispersion curves presented in the plot of phase velocity c versus qh for both the PS (a) and PMMA (b) thin films. The solid and open symbols are the experimental points. The solid lines are the theoretical predictions of the Lamb modes based on the layer-multiple-scattering (LMS) method with the use of the bulk elastic parameters (in Table 5-II) for both polymers. The horizontal dashed lines indicate the longitudinal and transverse sound velocities of the bulk polymer material, and the transverse sound velocity of the glass substrate.*

Table 5-II: bulk elastic parameters for theoretical calculation

	Longitudinal sound velocity c_l (m/s)	Transverse sound velocity c_t (m/s)	Density ρ (g/cm ³)
PS	2350	1150	1.05
PMMA	2800	1400	1.18
Glass substrate	5665	3340	2.50
Air	340	0	0.00123

This method constitutes a powerful tool for an accurate evaluation of the elastic properties of composite systems consisting of a number of different layers having the same two-dimensional periodicity in the x - y plane (parallel to the layers). An advantage of the method is that it does not require periodicity in the z direction (perpendicular to the layers). For each layer, the method calculates the transmission and reflection matrices, \mathbf{Q}^I and \mathbf{Q}^{III} respectively, for a plane wave incident on the layer with given frequency and $\mathbf{k}_{||}$ (the component of the wavevector in the x - y plane) from $z \rightarrow -\infty$ (i.e. with $k_z > 0$), as well as the corresponding matrices \mathbf{Q}^{IV} and \mathbf{Q}^{II} for incidence from $z \rightarrow \infty$ (i.e. with $k_z < 0$). Explicit expressions for these \mathbf{Q} matrices can be found in Ref. [72]. The transmission and reflection matrices of the composite system are calculated from those of the constituent layers. In the specific case considered here, we deal with the simple situation where a planar interface between two different homogeneous media is considered. The transmittance, reflectance, and absorbance of a (composite) slab, as well as the corresponding density of states of the elastic field, are obtained from the transmission and reflection matrices of the slab [72,87]. The eigenfrequencies of possible guided modes are evaluated from the condition to have a wave field localized within the slab. Dividing the slab into a left and a right part, this condition leads to the secular equation: $\det[\mathbf{I} - \mathbf{Q}^{II}(\text{left})\mathbf{Q}^{III}(\text{right})] = 0$. On the other hand, quasiguided modes of the slab manifest themselves as various types of resonance structures in the corresponding transmission spectrum and as lorentzian-shaped resonances in the density of states [88].

The theoretical calculation was done by my collaborator Dr. R. Sainidou at University of Athens. The simulation of the dispersion relation was performed with the use of bulk material properties for the film and the substrate, i.e. the longitudinal and transverse sound velocities and the density. For the glass substrate, the two sound velocities were obtained

directly from the measured longitudinal and transverse phonons in the glass substrate. The bulk elastic parameters used are listed in Table 5-II. As introduced in Section 2.3, there exist two kinds of film-guided modes distinguished by their polarizations, the Lamb modes polarized in the sagittal plane and the Love modes polarized in the film plane. The theoretical dispersion curves for the Lamb modes are indicated by the solid lines in **Fig. 5.3a** and **b**. Very good agreement between theory and experiment is obtained without using any adjustable parameter. On the contrary, the calculated dispersion curves (not shown) for the Love modes show strong deviation from the experimental data, further demonstrating that the experimentally observed modes are Lamb modes. The fact that a single set of bulk elastic parameters can capture well all the observed modes for all the films (both PS and PMMA) strongly indicates that these thin supported polymer films (down to 40 nm) can be well treated as isotropic and their elastic properties exhibit no obvious deviation from the corresponding bulk values. This finding is consistent with some few earlier BLS experiments on thin supported films or nanostructures down to the size of around 100 nm [24,25].

The dashed horizontal lines in **Fig. 5.3a** and **b**, from the bottom to the top, denote the transverse sound velocity c_{tp} and the longitudinal sound velocity c_{lp} of the film and the transverse sound velocity c_{ts} of the substrate, respectively. At large qh , the phase velocity of the Rayleigh mode (the first Lamb mode) becomes slightly below c_{tp} and approaches asymptotically to the surface Rayleigh velocity of the film material. This is due to the much shorter phonon wavelength compared to the film thickness at large qh . It is noteworthy that many experimental data points are above the threshold c_{ts} , especially for the thinnest film. Lamb modes above this substrate transverse velocity threshold, instead of decaying rapidly, show strong energy leakage into the substrate, therefore are quasilocalized as mentioned in Section 2.3. In principle, the energy leakage into air is also possible, but the huge acoustic impedance difference makes this leakage negligible.

Note that in the present experiment, the intensity of the Rayleigh mode, e.g. the peak *I* marked in **Fig. 5.2c**, is rather weak compared to some higher order Lamb modes and even not always discernable, in sharp contrast to the very strong Rayleigh mode observed in supported films on opaque substrate [24,26,89]. This disparity should be related to the difference in the relevant scattering mechanisms in the two cases. From Section 3.4, we know that there are two mechanisms responsible for Brillouin light scattering from surface

waves: the elasto-optic mechanism and the surface ripple mechanism. In general, for opaque substrate the surface ripple effect dominates due to the very small light penetration depth, while for transparent substrate, the elasto-optic effect takes over [58,82]. Hence the scattering intensity in my experiment should overwhelmingly come from the elasto-optic mechanism, as also manifested by the observed thickness dependent scattering intensity (the thicker the film, the stronger the intensity). This strong elasto-optic contribution is believed to be also responsible for the many observed leakage modes which are seldom observed on opaque substrates [24,26,89]. It is surprising that for all the films, the third Lamb mode is not observed experimentally, possibly due the very weak elasto-optic coupling strength for this mode.

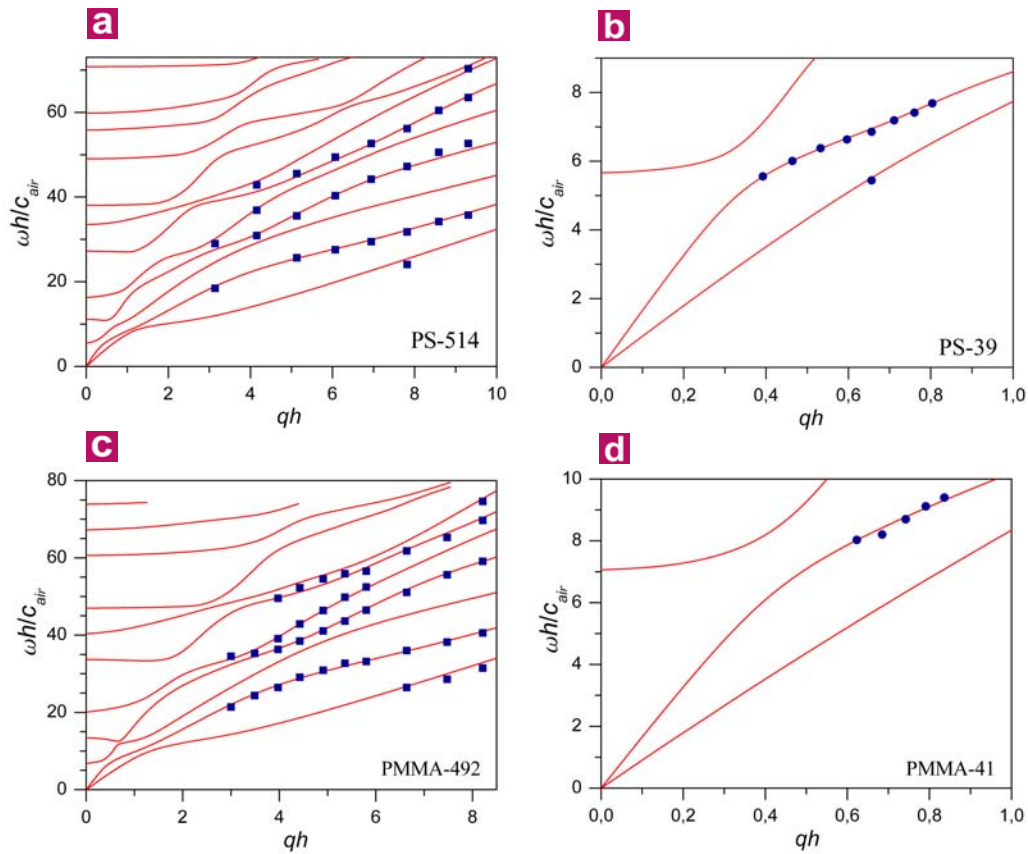


Figure 5.4 Optimal theoretical fitting for the thickest and thinnest PS and PMMA thin films. Dispersion relations presented in the plot of reduced frequency versus qh for both the PS and PMMA films with two extreme thicknesses: PS-514 (a), PS-39 (b), PMMA-492 (c) and PMMA-41 (d). The solid symbols are experimental points and the red lines are the theoretical fits. The elastic parameters for the fits are listed in Table 5-III for each film, respectively.

Table 5-III: elastic parameters for the optimal fitting

	c_{lp} (m/s)	c_{tp} (m/s)		c_{lp} (m/s)	c_{tp} (m/s)
PS-514	2409	1179	PMMA-492	2912	1456
PS-39	2350	1219	PMMA-41	2800	1512

Although the overall agreement between theory and experiment in **Fig. 5.3a** and **b** is very good, a more accurate estimation can be achieved by allowing variations of the elastic parameters from the bulk values and fitting the data points for different films separately. In the following, the Lamb modes for the thickest and the thinnest supported PS and PMMA films will be examined. In this case, the comparison between experiment and theory is better shown on the frequency (see **Fig. 5.2d**) than on the phase velocity dispersion diagrams (see **Fig. 5.3**). The strategy is to vary c_{lp} and c_{tp} relatively to the bulk values and seek for the best agreement with the experiment. For the thinnest films, the experiment probes the beginning of the lower branches of the Lamb modes, and it is found that these branches are rather insensitive to moderate variations of c_{lp} . Consequently for the thinnest films, we kept c_{lp} to the bulk value and adjusted c_{tp} to achieve the best agreement between theory and experiment. On the contrary for the thickest films, in addition to the lower branches, higher branches are also probed experimentally. It turns out that the latter are sensitive to the change of c_{lp} , thus the fitting procedure is more delicate since now both c_{lp} and c_{tp} must be adjusted for a good fit of both the lower and higher branches.

Figure 5.4a and **b** refer to the optimal fitting results for the PS-514 and PS-39 films respectively. Note that in **Fig. 5.4** the reduced frequency axis ($\omega h/c_{air}$) and wavenumber axis (qh) are used emphasizing the importance of the quantity qh , where $\omega=2\pi f$ is the angular frequency of the phonon. For the ultra-thin PS-39 film, the best capture of the two lowest branches can be achieved by increasing c_{tp} by 6% relative to the bulk PS value. The five branches observed for the PS-514 film can be well represented by allowing c_{lp} and c_{tp} 2.5% higher than the bulk values. Similar results are obtained for the PMMA films, the fits are shown in **Fig. 5.4c** and **d**. In the case of the PMMA-41 film, an 8% higher c_{tp} is used, while for the PMMA-492 film an increase of both c_{lp} and c_{tp} by 4% is necessary. The sound

velocities of these films determined from the fits are listed in Table 5-III. The experimental results show that the high-frequency mechanical properties, within 5% errors, remain the same in the glassy state for both supported thin PS and PMMA films in the thickness range of about 40-500 nm. In other words, no notable change in mechanical properties has been found in these thin supported polymer films with thickness down to at least 40 nm. The current phenomenological picture of the glassy state leads to [90] the relation $c_p \propto (v_0/v_f)^{1/3}$, where v_f is the free volume defined by $v_f = v - v_0$, the difference between the specific volume v and the closest packing volume v_0 . The closeness of c_p for the two different thicknesses for both polymers would imply either the same packing or the same ratio v_0/v_f in these annealed glassy thin films.

5.3.2 Glass transition

Let's first consider the possible novel aspects related to the glass transition phenomenon in thin polymer films. The 1D confinement imposed by the thin film geometry causes two major effects on the dynamics of polymer chains: the finite-size effect and the interface effect. Based on the cooperative-motion theory developed by Adam and Gibbs [91], a cooperative rearrangement of neighboring particles at low temperatures is necessary in order for any motion to occur. The smallest independent regions to permit such a cooperative motion are called cooperatively rearranging regions (CCR). When the size of the sample becomes comparable to the size of CCR which is inversely proportional to the configurational entropy of the system, the finite-size effect may start to appear. For polymers, there is an additional relevant length scale, that is, the size of a single polymer chain, e.g. the end-to-end distance R_{EE} which depends on the molecular weight. A number of experiments on thin PS films show that decrease in T_g occurs at sample thickness much larger than the size of CCR (typically a few nm [92,93]) and for free-standing films the reduction in T_g is molecular weight dependent. These observations suggest that the T_g reduction is not directly related to cooperative rearrangement, and the finite-size effect is reflected on the confinement of polymer chains.

Many experimental findings imply that the existence of a free surface or a substrate-film interface has a larger effect on the mobility of polymer chains [9]. The presence of a free

surface is believed to be able to enhance the chain mobility near the surface region and have an effect in reducing T_g [15,94,95]. In fact, T_g reduction is always observed for free-standing thin films. The extent of reduction is sensitive to the chemical structure, e.g., PS shows a much more pronounced drop in T_g than PMMA for the same film thickness and molecular weight. On the other hand, for supported thin films the existence of a substrate in general restricts the chain motion at the solid interface. This is manifested in the much less significant reduction in T_g for supported PS thin films than for a free-standing form of the same thickness. Moreover, if there is a strong interaction between the molecules and the bounding surface which exceeds the free-surface effect, an increase in T_g relative to the bulk value can be anticipated as suggested by theoretical simulations [96]. Increase of T_g with decreasing film thickness has been observed for PMMA films on silicon wafer with a native silicon oxide layer [19,97], whereas a decrease in T_g has also been found, e.g. on Au [97] or Al surface [98]. The increase in T_g has been attributed to the possible formation of hydrogen bond between PMMA and the silicon oxide surface [97]. By controlling the interfacial energy, P. Nealey et al. [99] have shown that the T_g of supported thin PS and PMMA films can be either higher or lower than the corresponding bulk values, further emphasizing the importance of the interface effect on the glass transition of thin films.

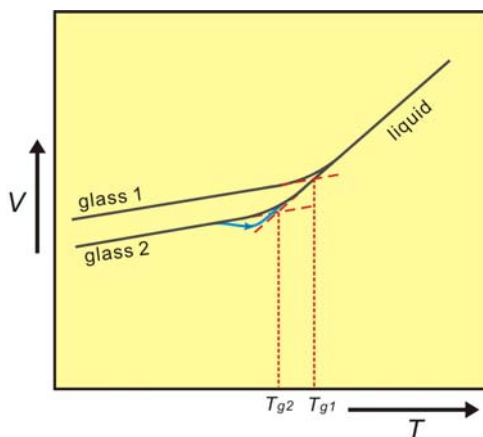


Figure 5.5 Volume V versus temperature T for a glass forming material. Two cooling rates are considered, Glass 1 has been cooled faster, resulting in a higher T_g than the more slowly cooled glass 2. Upon heating glass 2, a too small heating rate will lead to a notable decrease of the volume at temperatures close to the T_g , as indicated by the blue path.

When BLS is applied to study the glass transition, T_g can be estimated from the distinctly different temperature dependence of sound velocities in the glassy and rubbery regime. For thin films, in which propagation of pure longitudinal or transverse sound wave is not allowed, one can follow the temperature dependence of the phase velocity of any Lamb mode, as demonstrated for the free-standing thin films [11,18]. These Lamb modes have mixed polarizations with both longitudinal and transverse components and will exhibit the

characteristic “discontinuous” phase velocity change at the same temperature, namely, the T_g . The successful detection of the Lamb modes makes the study of the glass transition of thin supported polymer films by BLS possible. In this case the complication brought about by the substrate heating effect is no longer present.

A noteworthy aspect is that glass transition bears a strong kinetic nature [100], time, in general, becomes an important factor. This can be easily appreciated from the well-known volume V versus temperature T plot in **Fig. 5.5**. Suppose a cooling process from the melt, with a fast cooling rate the transition will take place at a higher temperature due to the insufficient time for structure relaxation compared to a slow cooling rate. As a result, the glass line is shifted up and a higher T_g (T_{g1}) is obtained as indicated in **Fig. 5.5**. The accumulation time in my experiment for one spectrum is relatively long (on the order of several hours) and varies with film thickness. Hence it is necessary to first consider the possible influence of time in the determination of T_g . It is not preferred to use the cooling run

to determine T_g because this would easily lead to the above mentioned non-well-defined glassy state and make the comparison of T_g of different films somewhat ambiguous. On the contrary, the choice of the heating run is able to minimize the heating rate dependent T_g effect, which takes advantage of the extremely slow relaxation rate in the glassy state. Note that this approach has a precondition, namely, the starting glassy state must be well defined. This condition was obviously satisfied with our sample preparation procedure in which all the films underwent the same well-defined thermal history. Upon heating, physical aging could in principle happen in the glassy state, especially when the heating rate is very small. A direct consequence of this structure relaxation is that the specific volume of the polymer will deviate from the previously defined glass line (e.g. glass 2 in **Fig. 5.5**) and gradually decrease. This would lead to a lower T_g as indicated by the blue curved path in **Fig. 5.5**. However, if the physical aging becomes significant only in the

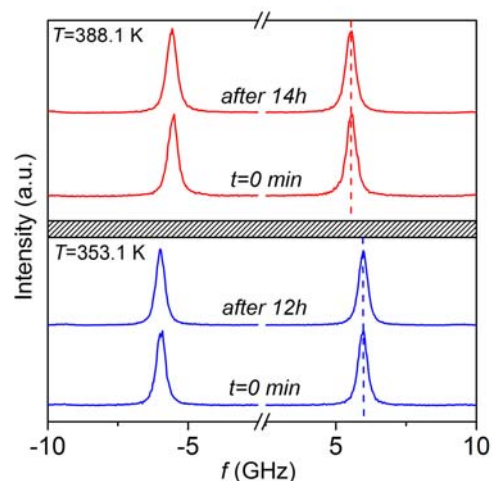


Figure 5.6 Time-dependent BLS spectra of a bulk PS sample. *Two BLS spectra from a bulk PS sample were measured at two different times with a time interval more than 12 h, at 353.1 K and 388.1 K, respectively. The accumulation time for all spectra was about 1 min.*

close vicinity of T_g , it will have negligible impact on the accuracy of the determined T_g in the present experiment because its value is identified by the intersection of the glass line and the liquid line which are free from the influence of the complex structure relaxation near T_g . In fact, this is believed to be the case, and the heating approach has been previously used to determine T_g of thin free-standing films by BLS [18] and the results were confirmed by later transmission ellipsometry measurements [101] on much shorter time scale.

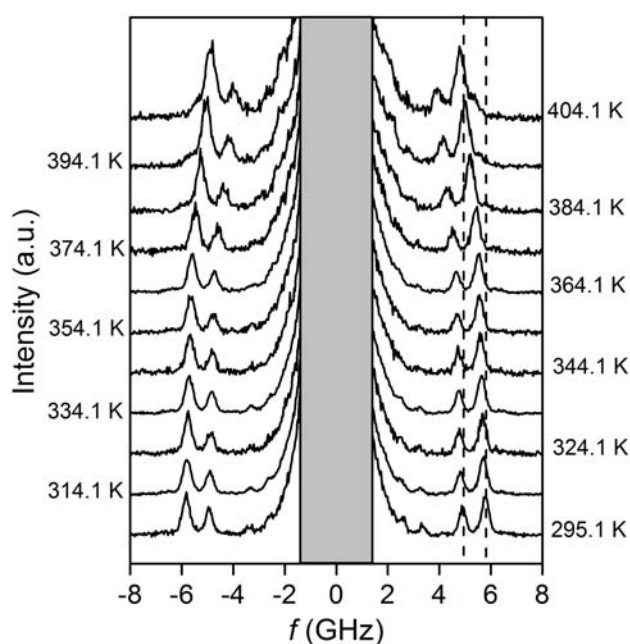


Figure 5.7 Temperature dependent BLS spectra for the PS-514 film. The spectra were measured at eleven different temperatures below and above the T_g , at the fixed $q=0.0152 \text{ nm}^{-1}$. The glass transition can be studied by monitoring the change of peak frequencies with temperature.

To further support this view, a reference experiment on a bulk PS slice (thickness 1.2 mm, $M_w=284000$, $M_w/M_n=2.6$, Goodfellow Ltd.) was performed and the results are shown in **Fig. 5.6**. This bulk PS sample was heated (10 K/min) from room temperature to 353.1 K, and kept for 5 min before the BLS measurement started. A short accumulation time (~ 1 min) was adequate for this bulk sample benefiting from the very strong scattering intensity. To check the possible structure relaxation effect, two spectra were recorded at two different times. Despite the large time interval (more than 12 h), the two spectra are essentially identical (within 0.2% errors) when the peak frequency and width are concerned. This clearly corroborates the assumption that structure relaxation in the glassy state can be well ignored in the experimental time window for the thin film T_g measurement. A similar check was also performed at 388.1 K above T_g and the same result was obtained. This is evident as in the liquid state the system can reach its thermal dynamic equilibrium very quickly.

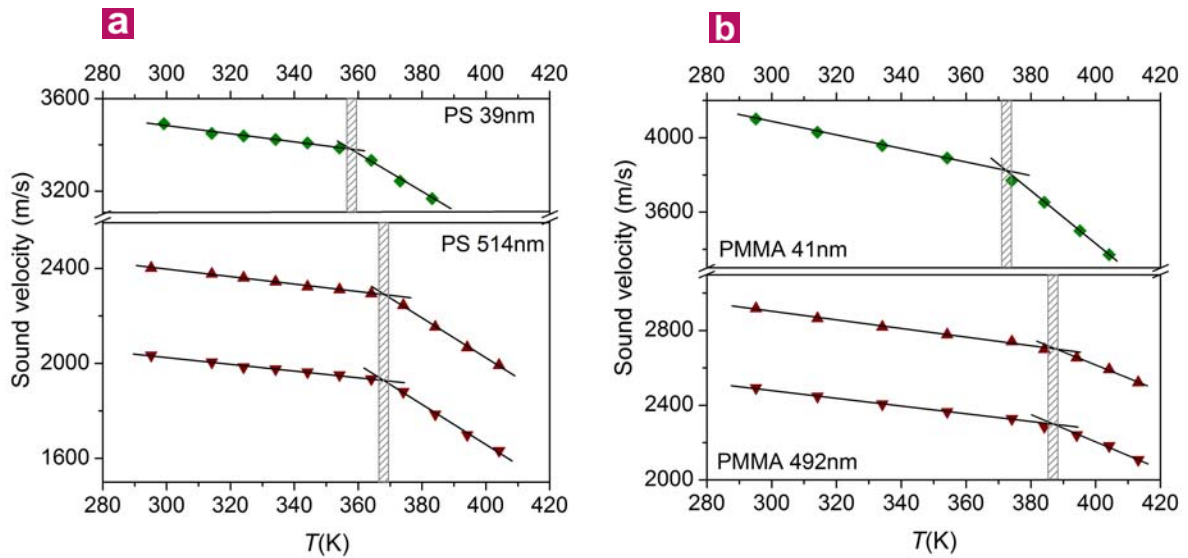


Figure 5.8 T_g determination of thin supported PS and PMMA films by BLS. The phase velocities of the Lamb modes at a given q are plotted as a function of temperature for the thickest and thinnest PS (a) and PMMA (b) films. The different temperature dependence of the phase velocity in the glassy and liquid state leads to the characteristic kink at T_g . The symbols are the experimental points and the solid lines are the least-square fitting results. The T_g value is determined by the intersection of the glass line and the liquid line, as indicated by the shadowed region. For the thicker films, the two strong Lamb modes are chosen for the determination of T_g , and for the thinner films, the only observable Lamb mode is utilized. For both PS and PMMA, a reduction in T_g for the ultra-thin film is observed.

In the present experiment, the T_g of the thickest and thinnest films for both polymers were measured to check the possible confinement effect. The reason for this choice was twofold. First, many existing experimental results suggest that deviation of T_g from the bulk value starts to appear when the film thickness becomes below 100 nm [9]. Second, the main purpose of the present work, instead of conducting a systematic BLS measurement of T_g , aimed to illustrate, for the first time, the ability of BLS in probing the glass transition of thin supported polymer films. By plotting the frequency (or phase velocity) of the Lamb modes as a function of temperature, based on the glass line and liquid line, the T_g can be determined. **Figure 5.7** displays the BLS spectra of the PS-514 film at $q=0.0152 \text{ nm}^{-1}$, at eleven different temperatures. The two dashed lines indicate the frequencies of the two strong modes at room temperature. The result is shown in **Fig. 5.8a** from which one can clearly recognize the different temperature dependence of the phase velocity of a given Lamb mode in the glassy and rubbery state. The symbols are the experimental data points, and the solid lines are the least square fit of the experimental data in the glassy and rubbery regime, respectively. The T_g is defined by the intersection of the glass and liquid lines, as highlighted by the shadowed

region in **Fig. 5.8**. For this PS-514 film, the determined T_g is about 368 K, agreeing with the commonly encountered literature value 373 K [102] for bulk PS. The results for other films are also presented in **Fig. 5.8**. A clear T_g suppression is observed in both ultra-thin films (around 40 nm) irrespectively of their different chemical nature.

This notion of softening of thin films at lower temperatures compared the bulk materials is corroborated by the values of the elastic constants of the ultra-thin films at temperatures near but above T_g . For example, at 374.1 K, using the data for the PS-39 and PS-514 films, c_{lp} and c_{tp} are found to, compared to their respective room temperature values, decrease by about 28% and 13% for the PS-39, and 22% and 6% for the PS-514. The stronger softening for the PS-39 film is in conformity to its lower T_g . The reduction in T_g (from 368 K to 358 K) for the PS-39 film agrees with many existing experimental results. In fact, for PS thin films negative deviation of T_g is almost always observed whatever kind of substrate is used, indicating the weak interaction between PS and the substrate. For the PMMA-41 film, the clearly observed decrease in T_g (from 387 K to 372 K) did not follow our expectation, as the formation of the hydrogen bond between PMMA and the silicon oxide surface is supposed to lead to a higher energy barrier for the chain motion and therefore to an increase in T_g . It should be mentioned that the PMMA system is much less extensively investigated than the PS, no reliable conclusion can be made so far and contradictory results exist [21,22]. For PMMA thin films, it is found that the tacticity also plays a role. For example, Grohens et al. [103] observed strong decrease in T_g for isotactic PMMA on Si substrate but significant increase for syndiotactic PMMA on the same substrate. To compare the results from different techniques, it is important to know what kind of physical property is used to determine T_g . For example, in the ellipsometry and X-ray reflectometry experiments [19], the film thickness h is measured as a function of temperature. In the BLS experiment, the phase velocity for a given phonon is measured as a function of temperature, and this velocity is directly related to the adiabatic compressibility β_s of the material. When the temperature varies and passes T_g , both thermal expansion coefficient and temperature dependence of β_s show a near discontinuous change, signifying the glass transition. Practically, the intersection of the glass and the liquid lines are extensively used to define the T_g value.

The observed negative deviation of T_g for the PMMA ultra-thin film supported on glass substrate seems to suggest the insufficiently strong interaction between PMMA and the substrate surface. This should be related to the detailed sample preparation process as well as

the surface properties of the substrate. On the other hand, other factors such as chain conformations, thermal history, or entanglements may also be responsible for this observation. A detailed investigation is beyond the aim of this work, however it is highly desirable to check the glass transition on the same sample using other techniques under similar experimental conditions, e.g. in the same time window. A challenge is that the widely used ellipsometry fails to effectively work with transparent substrate. There is no direct correlation between the room temperature elastic properties of these thin films and the change in their T_g . Even for free-standing thin PS films, no deviation from bulk elastic parameters has been found for a reduction in T_g as much as 65 K [104]. In my experiment the probed elastic parameters and T_g are the average values across the entire film thickness. Despite the even more demanding experimental challenges, future investigation should also consider measurements of the distribution of elastic properties and T_g values across the thickness of the film, as suggested by the recent work by Torkelson et al [105-108].

Chapter 6

Elastic excitations in 1D polymeric photonic structures

6.1 Introduction

Recently Weber et al. at 3M [109] successfully created broadband omnidirectional dielectric stack mirrors based entirely on polymer multilayer architectures. This invention eliminates a long-standing limitation in constructing a mirror by using a multilayer stack as restricted by Brewster's law, according to which the reflection of p-polarized light at a material interface decreases with increasing angle of incidence and ultimately vanishes at a critical angle (Brewster's angle). These multilayer mirrors consist of hundreds or thousands of thin layers of two different polymers in strictly alternating fashion with at least one constituent being highly birefringent. Each birefringent layer is either uniaxial, with equal in-plane (x, y) refractive indices or biaxial with different refractive indices along all three directions (x, y, z). In addition, the in-plane refractive indices of adjacent polymer layers differ, which gives rise to so-called giant birefringent optics accompanied by surprising and useful optical effects [109].

Being so much attracted by the novel optics of these multilayer mirrors, much less attention has been paid to their elastic properties. The giant birefringence is not only an indication of optical but also of mechanical anisotropy. The periodic variation of the refractive index along the film thickness direction is accompanied by a corresponding variation of the elastic constants and layer densities. When the elastic and/or density contrast between adjacent layers is sufficiently large, the film may behave as a one-dimensional (1D)

phononic crystal [36,46] with stop bands at certain frequencies for elastic waves propagating along the z -direction. On the other hand, waves propagating in the sample plane (x - y plane) are also significantly affected by the elastic properties of individual layers, especially when their wavelengths are comparable to the individual layer thickness h , as already encountered in the case of supported thin films in the last chapter. Consequently, elastic excitations in these multilayer structures can be complex and capable of carrying valuable information about the system, i.e. the elastic properties and the structural periodicity.

So far the only BLS experiment on polymer films with a multilayer structure was performed by J. Forrest et al. [26] on supported one to five alternating polystyrene/polyisoprene (PS/PI) spin-coated homopolymer thin films. They did not succeed, however, to mechanically resolve the individual homopolymer layers (20-80 nm thick) despite the large mechanical contrast between the glassy PS and the rubbery PI at room temperature. The above mentioned polymeric multilayer films composed of many periodically stacked thin layers obviously serve as a better model system for the investigation of elastic wave propagation in the presence of multilayers. First, although the individual layer is very thin (tens of nm to hundreds of nm), the large number of layers makes the final film rather thick (tens of μm), which greatly enhances the light scattering signal in BLS experiments. More important, the thick film in a free-standing form eliminates the substrate interference and also makes the free-surface effect negligible, therefore simplifying the boundary conditions that may influence the wave propagation as only the layer interfaces are involved. In this chapter, elastic excitations in a polymeric multilayer (1D periodic) film will be studied.

6.2 Film characterization

The sample analyzed is a multilayer polymer mirror film manufactured by 3M and kindly provided by Dr. A. J. Ouderkirk (3M Company). Despite its high reflectivity of light, this film with purple color allows sufficient transmission for the BLS measurement. The film is a stack of over 200 identical bilayer units composed of poly(methylmethacrylate) (PMMA) and poly(ethyl terephthalate) (PET) layers, 78 nm and 118 nm thick respectively. The layer thickness values are deduced from transmission electron microscope (TEM)

images of the film cross section as shown in **Fig. 6.1**. PMMA layers are optically and mechanically isotropic, while PET layers possess uniaxial anisotropy with $n_x = n_y \neq n_z$ and $E_x = E_y \neq E_z$. Here n_x, n_y, n_z and E_x, E_y, E_z are refractive indices and Young's moduli along the x, y , and z directions, respectively. The degree of birefringence in PET layers was estimated from ellipsometry and polarized reflectometry measurements to be $\Delta n \approx 0.15$. For TEM examination, thin sections of about 60 nm were prepared using a Leica EMUC6 ultra-microtome employing a diamond knife at room temperature. TEM experiments were carried out on a JEOL 2010F equipped with a post-column Gatan Imaging Filter (GIF). The zero loss energy filtered images were taken with an energy window of 15 eV.

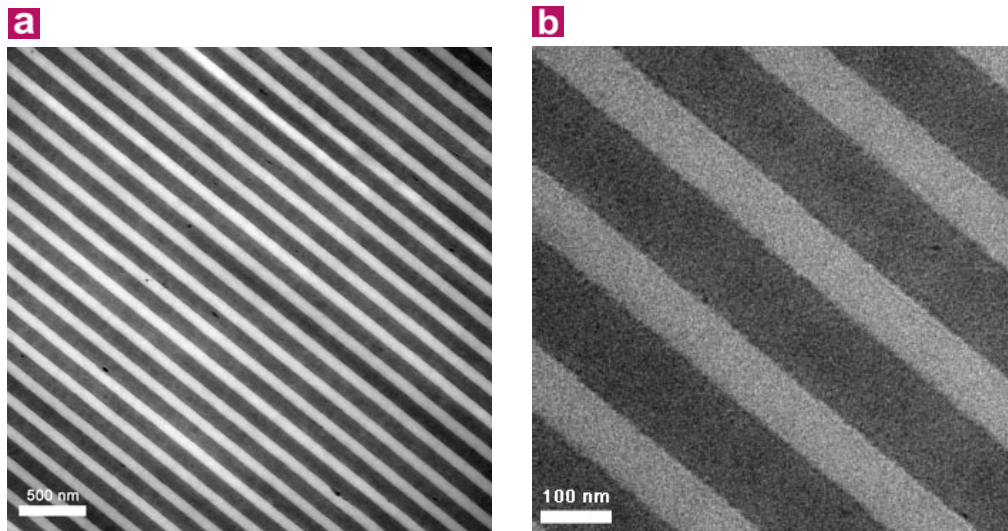


Figure 6.1 TEM images of the cross section of the PMMA-PET multilayer film. **a**, Low magnification. **b**, High magnification. PMMA layer thickness is 78 nm and PET layer thickness is 118 nm.

6.3 Results and discussion

6.3.1 Dispersion relation for in-plane phonon propagation

As for the supported thin films in the last chapter, the special scattering geometry with q parallel to the film plane is used. **Figure 6.2** shows typical polarized BLS spectra measured at two different q values (0.0116 and 0.0150 nm⁻¹) at ambient conditions. The film displays

up to six modes, which are well resolved in the spectra of **Fig. 6.2a** and **b**. These modes are successively labeled from 1 to 6 in order of increasing frequency. At $q=0.0116 \text{ nm}^{-1}$ (**Fig. 6.2b**), three distinct Brillouin doublets (2-4) are observed, with mode (4) being the most intense. At higher frequencies two additional spectral features (mode (6) and G) can be identified. Albeit barely discernible in the linear intensity scale, their existence is clearly visualized by plotting the intensity logarithmically, as shown in the inset of **Fig. 6.2b**. The faint peak marked as G is identified as the ghost of the strong mode (4) due to higher order interference effects in the tandem Fabry-Perot interferometer. At higher q values (**Fig. 6.2a**) two other modes are resolved: the weak low-frequency mode (1) and the high-frequency mode (5) with intensity comparable to mode (4). Moreover, an additional shoulder-like spectral feature appears on the high frequency side of mode (5). Note that this shoulder-like spectral feature should not be confused with mode (6).

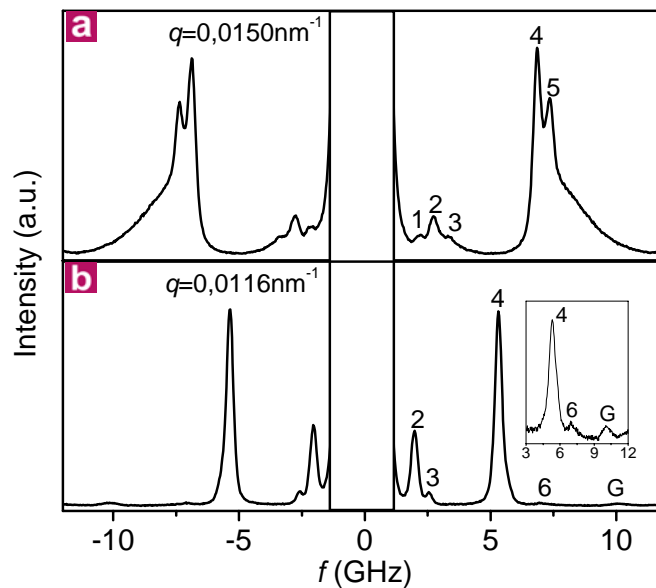


Figure 6.2 Typical BLS spectra at two different q values. **a**, Spectrum at $q=0.0150 \text{ nm}^{-1}$. The numbers denote the distinct phonons and the strong central Rayleigh line is shielded for clarity. **b**, Spectrum at $q=0.0116 \text{ nm}^{-1}$. The inset emphasizes the weak mode (6) by choosing logarithmic intensity scale. The small feature G is the interferometer ghost of the strong mode (4).

Figure 6.3 illustrates the dispersion relation for the in-plane phonon propagation in this polymeric multilayer system. The six modes are labeled in accordance with the six numbered peaks in **Fig. 6.2**. At low q values, due to the proximity of their velocities, not all six modes are resolved, as shown in **Fig. 6.2b**. In fact, the identification of these modes can

only be made by referring to the dispersion relation. The observation of up to six modes is strikingly different from what would be expected if the film (with total thickness of $\sim 40 \mu\text{m}$) behaved as a mechanically homogeneous isotropic medium, where only two bulk modes (longitudinal and transverse) are anticipated. Their existence unambiguously suggests the explicit contribution of the individual constituent layers to the elastic excitations in this multilayer film. The result is in clear distinction from the earlier BLS study by J. Forrest et al. [26], where the dispersion relation of the PS/PI multilayer film was well described by an effective medium approach even though the mechanical contrast between the glassy PS and rubbery PI is large at room temperature.

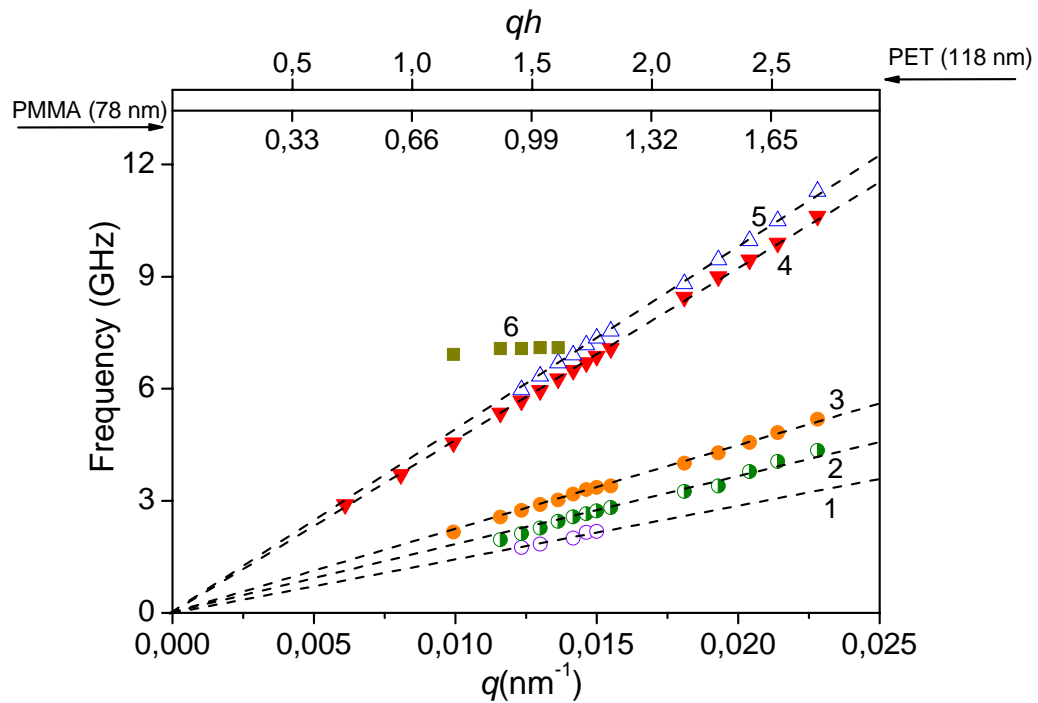


Figure 6.3 Dispersion relations of in-plane propagating phonons. *The different symbols represent different modes observed experimentally, the dashed lines are the linear fits to the five observed acoustic-like modes. Mode 6 is insensitive to the variation of q . The upper abscissas show the corresponding qh ranges for the two constituent layer thicknesses.*

It is evident from the dispersion relation that five out of the six observed modes are strictly acoustic-like. In other words, their frequency increases linearly with q , which results in a constant (q -independent) phase velocity, in sharp contrast to surface dispersive modes discussed in the last chapter. According to the two upper abscissas in **Fig. 6.3** displaying the qh values for the two constituent layers, qh falls roughly between 0.5 and 2.5. In this range,

the elastic wavelength and the layer thickness are comparable and under such conditions, dispersive modes, e.g. Rayleigh and Lamb waves, are expected for either free-standing or supported films [24,26,110,111]. All these dispersive modes possess both transverse and longitudinal components of the displacement fields, travel parallel to the film surface and are polarized in the sagittal plane. In this self-supporting polymeric film, except for the two outmost layers, every constituent layer A of the same type can be regarded as located in the same microenvironment, namely, sandwiched by another two identical layers B . For each layer the mechanical boundary conditions encountered are similar to those in supported thin films, thus similar in-plane phonon propagations with dispersive characteristics are anticipated. The five observed non-dispersive modes suggest that other types of elastic excitations are active in this PMMA/PET multilayer film. The phase velocities of the five acoustic-like modes are listed in Table 6-I.

Table 6-I: Elastic parameters

Mode	1	2	3	4	5
Sound velocity (m/s)	890±20	1175±23	1415±25	2905±30	3085±30
$\alpha_T(T < T_g) \times 10^4$ (K ⁻¹)	—	3.9±0.2	8.6±0.4	9.0±0.4	5.8±0.3
$\alpha_T(T > T_g) \times 10^3$ (K ⁻¹)	—	1.46±0.05	1.50±0.06	1.3±0.03	1.23±0.03

6.3.2 Finite element analysis (FEA) modeling

To provide an interpretation for the observed in-plane propagation modes, the theoretical phonon dispersion relation using finite element analysis (FEA) was computed. The computation was carried out by my collaborator Taras Gorishnyy at MIT (Boston). A two-dimensional (2D) eigenvalue model was created and solved using the COMSOL MULTIPHYSICS 3.2 FEA package based on the linear elastic plain-strain approximation. Since the film is periodic along the z direction, it is sufficient to model a single unit cell consisting of one PMMA and one PET layer and use Bloch boundary condition $\vec{u}(x,0) = \vec{u}(x,d) \cdot \exp(iq_z d)$ for the boundaries parallel to the x axis. Here q_z is the z -component of the phonon wavevector and d is the bilayer thickness. The film is homogeneous and infinite (the sample size is much larger than the phonon wavelength)

along the x and y directions and the phonon wavevector is taken to be parallel to the x axis. Thus, we look for the wave equation solution in the form $\vec{u}(x, z) = \vec{u}(z) \cdot \exp(iq_x x)$, which leads to the second boundary condition, $\vec{u}(0, z) = \vec{u}(l, z) \cdot \exp(iq_x l)$ for the cell boundaries parallel to the z axis. Here l is a length of the modeling domain along the x direction. This periodicity along the x axis is artificially introduced in order to apply the FEA, and the solution independent of the actual value of l is used in further analysis. The model meshing and solver accuracy were previously validated by computing phonon dispersion relations for a homogeneous material and for 2D hexagonal phononic crystals and comparing the results with the analytical solutions (homogeneous material) and independent numerical computations (2D phononic crystals) [38,41]. In both cases an excellent match was observed.

The amorphous PMMA layer is modeled as an isotropic medium with Young's modulus $E_{\text{PMMA}} = 6.26$ GPa, Poisson ratio $\nu_{\text{PMMA}} = 0.341$ and density $\rho_{\text{PMMA}} = 1200$ kg/m³. These values for elastic constants are based on independent measurements of the speed of hypersound in pure PMMA films. On the other hand, the PET layer, due to the crystallization ability of PET, has to be taken as anisotropic (uniaxial). Its elastic constants depend on the degree of anisotropy, which is in turn determined by the history of the sample processing. As a result, it is very difficult to prepare pure PET films with exactly the same elastic constants as in our sample for hypersound velocity measurements. For this reason, we were unable to determine elastic constants of anisotropic PET layers independently and instead we used them as fitting parameters to ensure the best match between experimental and theoretical dispersion relation. Rich features of the dispersion relation allow the identification of a single combination of elastic constants that provides good agreement between theory and experiment. In particular, it was found that the transverse sound velocity was determined almost entirely by shear modulus G_{xz} , the longitudinal sound velocity was influenced primarily by Young's moduli E_x and E_z and Poisson ratios ν_{xy} and ν_{xz} , while the position of the q -independent mode (**Fig. 6.3**) was a function of shear modulus G_{xz} and Young's moduli E_x and E_z . Accordingly, the PET layer was modeled as a transverse isotropic medium with $E_{x_PET} = E_{y_PET} = 6.0$ GPa, $E_{z_PET} = 4.0$ GPa, $\nu_{xy_PET} = 0.40$, $\nu_{xz_PET} = 0.48$, $G_{xz_PET} = 2.2$ GPa and $\rho_{\text{PET}} = 1380$ kg/m³; here G_{xz_PET} is the shear modulus in the xz plane. These values are consistent with previous studies of elastic constants of anisotropic PET [112-114].

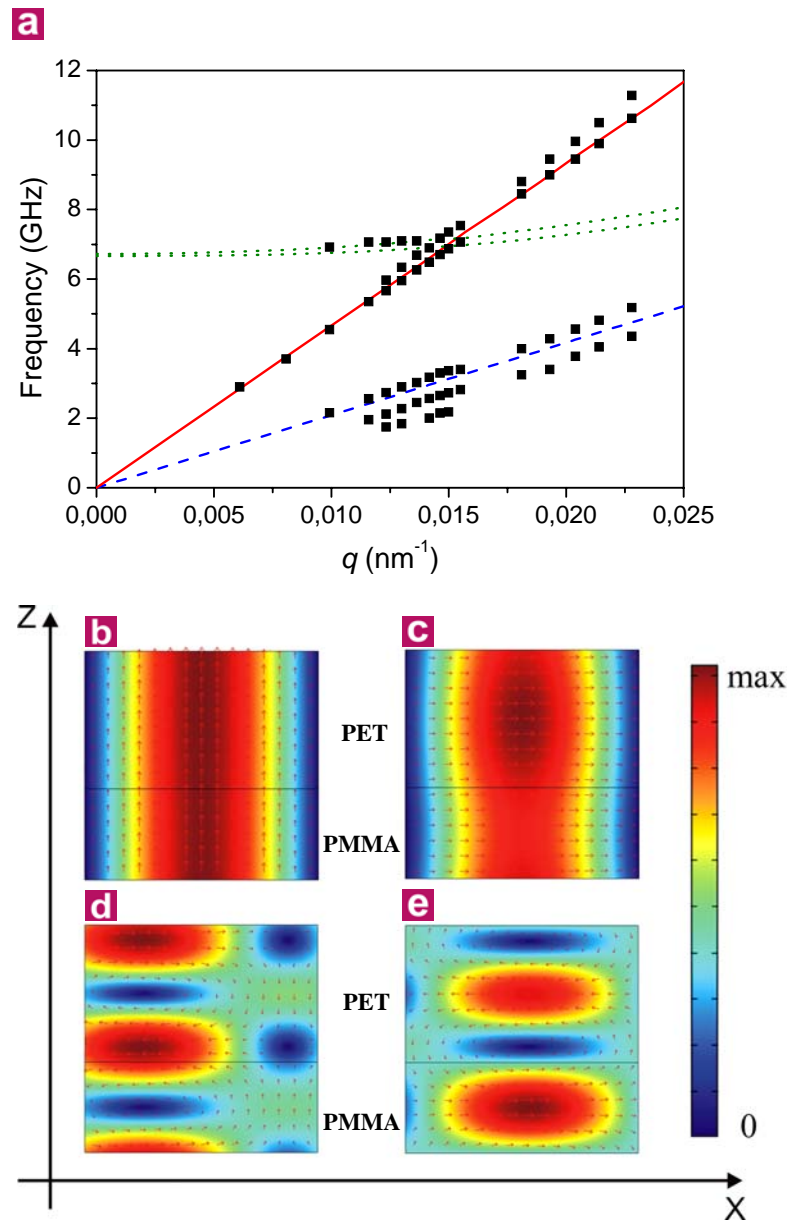


Figure 6.4 Finite element analysis of in-plane phonon propagation. **a**, The various lines represent theoretical dispersion relations: solid line — longitudinal mode, dashed line — transverse mode, dotted lines — mixed modes. For the ease of comparison, experimental data denoted by black squares are also included. **b**, Elastic displacement field for a transverse mode at $q=0.01257 \text{ nm}^{-1}$. **c**, Elastic displacement field for a longitudinal mode at $q=0.01257 \text{ nm}^{-1}$. **d,e**, Elastic displacement fields for the mixed anti-parallel modes at $q=0.01257 \text{ nm}^{-1}$.

The theoretical phonon dispersion relation is shown in **Fig. 6.4a**. For the ease of comparison, experimental data are also plotted on the same graph (black rectangles). Four modes are expected according to the model prediction – a transverse mode (dashed lines), a longitudinal mode (solid lines) and two closely spaced high frequency quasi-longitudinal

guided modes (dotted lines). The details of their displacement fields at $q=0.01257 \text{ nm}^{-1}$ are shown in **Fig. 6.4b-e**. Note that for both the longitudinal (**Fig. 6.4c**) and transverse (**Fig. 6.4b**) waves, the regions of high deformation are not confined to any individual layer, but rather are spread such that their displacement vectors are only weakly dependent on z , especially for the transverse wave. In contrast, for the high frequency quasi longitudinal waves there are two regions of high deformation with the displacement vectors anti-parallel to each other, as shown in **Fig. 6.4d-e**. These regions are localized within individual layers.

The positions of all modes are in good quantitative agreement with the experimental data. However, the model does not predict the splitting of the transverse and longitudinal lines into three and two components, respectively, as observed experimentally. It is well known that optical birefringence or diffraction [115] may lead to the splitting of Brillouin lines due to the possible generation of light beams propagating in directions other than the main beam. However, for the present experiment, these possibilities can be safely ruled out. For $\Delta n = 0.15$, the birefringence induced splitting (ordinary and extraordinary rays) would be an order of magnitude smaller than what we have observed and cannot be resolved experimentally. The small periodicity (compared to the laser wavelength) as well as the weak refractive index contrast also excludes optical diffraction interference, as confirmed by the failure of observing any abnormal optical beams in the present experiment. Therefore one must search for the cause of additional modes within the framework of elastic wave propagation.

There are two relevant length parameters in our problem, the bilayer thickness $d=h_{PMMA}+h_{PET}$ and the phonon wavelength λ . Their ratio $\xi = d / \lambda$ will determine how the propagating waves interact with the layered medium, i.e., if they experience it as a homogeneous medium or if they are sensitive to the structure of the individual layers. The larger the ξ , the more one can expect waves to be localized within individual layers. In the extreme case when $\xi \gg 1$, waves propagating in each layer become completely insensitive to the presence of the other layers.

Figure 6.4b-e shows a weak z -dependence for the transverse and longitudinal modes, but not for the two high-frequency q -independent modes. This behavior corresponds to the regime, where phonon propagation is starting to be influenced by the multilayer structure of the film. It is helpful then to examine now how wave propagation changes upon further

increase in ξ paying special attention to acoustic-like modes. **Figure 6.5** shows the theoretical dispersion relation for the transverse-like (dashed lines) and longitudinal-like (solid lines) modes, as well as the extrapolation of the experimental data (dotted lines) based on sound velocities of modes (2)-(5) for q in the range from 0.05 nm^{-1} to 0.07 nm^{-1} . Interestingly, the existence of three transverse-like and three longitudinal-like modes is now predicted by the model. The phase velocities of these modes match the experimental values quite well. Unlike the case of lower q values, the displacement fields of these modes exhibit strong z dependence and are contained either in PET or in PMMA layers. This result suggests that the five acoustic-like modes observed experimentally may relate to localized longitudinal-like and transverse-like phonons propagating within individual layers. It is not entirely clear why the theory predicts the line splitting for somewhat higher values of q than observed experimentally. Imperfections at interfaces, such as interfacial roughness and strain fields, as well as certain degree of uncertainty about elastic constants of anisotropic PET layers may be responsible for this difference.

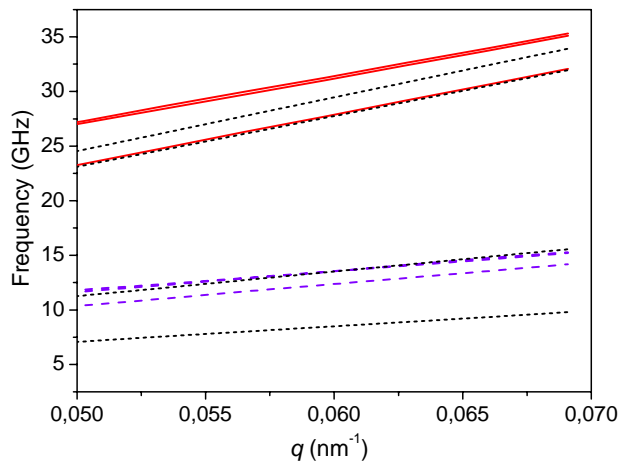


Figure 6.5 Phonon dispersion relation for $q=0.50\text{--}0.68 \text{ nm}^{-1}$. Red solid lines – theoretical longitudinal modes, violet dashed lines – theoretical transverse modes, black dotted lines – extrapolation of experimental data based on sound velocities for modes (2)-(5).

6.3.3 Temperature dependence of the elastic constants

In the preceding section, the observed acoustic-like phonons were associated with the individual layers. Since PET and PMMA possess different glass transition temperatures T_g , the variation of the phase velocities of these acoustic-like phonons with temperature is anticipated to display the characteristic kink at T_g , which should occur at distinctly different temperatures. This would be a direct confirmation of their association to the individual layers. For the temperature dependent measurement, the sample was heated from room

temperature to about 413 K by multiple steps. At each temperature the sample was stabilized for about 10 min before the beginning of the measurements. Then BLS data were acquired for about 40-60 min for each scan.

In **Fig. 6.6**, the phase velocities of the 4 modes (modes (2)-(5)) are plotted as a function of T . Clearly, the harder layer (PMMA) exhibits a higher T_g (about 373 K) than the softer layer (PET) with a T_g about 353 K. It is also evident from **Fig. 6.6** that modes (2) and (4) should be associated with PET layers and modes (3) and (5) with PMMA layers since they exhibit the same values of T_g , respectively. These results are in accordance with our attempt to associate these modes with the two types of individual layers. The sound velocity of the weak, low frequency mode (1) shows a very small variation with T that renders the identification of the kink feature ambiguous, and it is therefore excluded from **Fig. 6.6**.

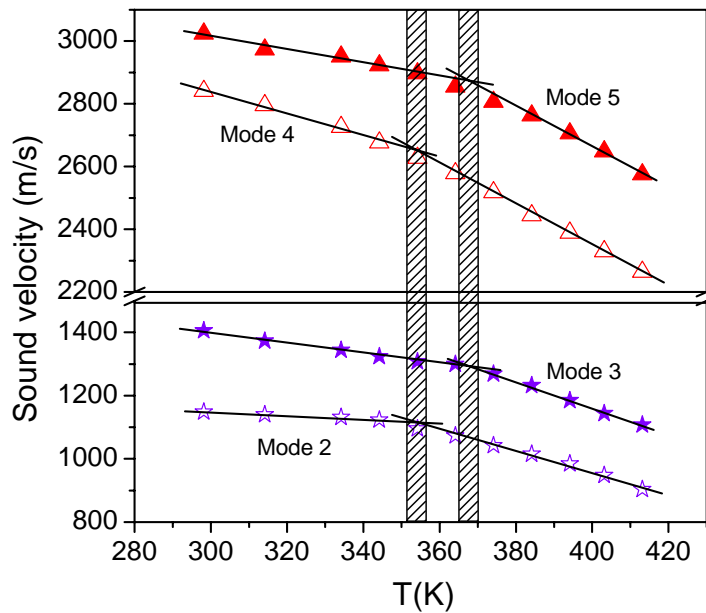


Figure 6.6 Temperature dependence of the phonon phase velocities. The phase velocities of the four main acoustic-like modes (see Fig. 6.3) are plotted as a function of temperature. The shaded regions demote the region of the respective glass transition temperatures of the two component polymers. The T_g is determined by the intersection of the glass line and the liquid line as represented by the solid lines which are obtained from the least square fit to the experimental data before and after glass transition. Data points in the vicinity of T_g were excluded from fitting.

The dependence of phase velocities of these modes at temperatures above and below T_g can be well described by the linear relation $c(T) = c(0)(1 - \alpha_T T)$ with $c(0)$ being the extrapolated velocity in the particular polymer at 0 K, and α_T is the proportionality

coefficient which describes how rapidly the sound velocity of a particular mode changes with temperature. Since the longitudinal sound velocity is related to the adiabatic compressibility β_s of the material, α_T of the two longitudinally featured modes (4) and (5) in different layers characterize the temperature dependence of β_s of the two component materials. In addition, the high frequency low strain tension/compression and shear moduli are directly determined by the longitudinal and transverse velocities respectively. Therefore α_T (Table 6-I) for the four modes also provides the information about the temperature dependence of these two very important material properties in the glassy ($T < T_g$) and the rubbery ($T > T_g$) regime. These values were obtained by performing a linear fit of the experimental sound velocities before and after the glass transition. Data points in the vicinity of T_g were excluded from the fit. In this context, it should be mentioned that the DSC, a non-local technique sensitive to the specific heat change at T_g , was unable to detect the higher T_g , displaying only a single $T_g \sim 348\text{-}353$ K. Therefore, BLS that measures the adiabatic compressibility of the system could in principle be utilized to probe the T_g at different layer thicknesses in this sandwiched multilayer arrangement.

For the transverse mode (2) and (3) in the PET and PMMA layer respectively, the coefficient α_T is somewhat larger than for the longitudinal modes in the rubbery regime. This is expected, since the shear modulus should eventually decrease to zero in the liquid state in contrast to the tension/compression modulus. In the glassy regime, these material properties reflect different deformations of the matter and a prediction on the relative magnitude of α_T for the two moduli is not possible.

6.3.4 Mechanical anisotropy

The existence of mechanical anisotropy in this polymeric multilayer film is quite probable based on the birefringent nature of the PET layers. Indeed, the mechanical anisotropy has already been recognized in the previous modeling of the PET layer in FEA. The reason that the main focus of this work is on phonon propagation parallel (q_{\parallel}) instead of normal to the layers (q_{\perp}) is due to the geometrical restriction that allows access to only a very narrow range of q_{\perp} . Therefore, it is impossible to record a complete dispersion relation $\omega = \omega(q_{\perp})$, as was done for the case of in-plane phonon propagation.

Nonetheless, the mechanical anisotropy can still be revealed with a single measurement at a particular value of q_{\perp} , without having to resort to the dispersion relation. In contrast to the presence of six modes (**Fig. 6.3**) for the in-plane phonon propagation, only a single longitudinal phonon is resolved in the spectrum of **Fig. 6.7** with q perpendicular to the layers. Note that for this scattering geometry (inset to **Fig. 6.7**), the value of q and hence the phase velocity $c_l=2\pi f/q$ of the phonon depends on the refractive index n of the film (see Eq. 4.25). Since $n_{\text{PMMA}}=1.49$ and $n_{\text{PET}}=1.57$ (noncrystalline, isotropic), it is quite safe to assume the lowest limit of n of the film (even after stretching) is 1.5, which yields $q=0.035 \text{ nm}^{-1}$.

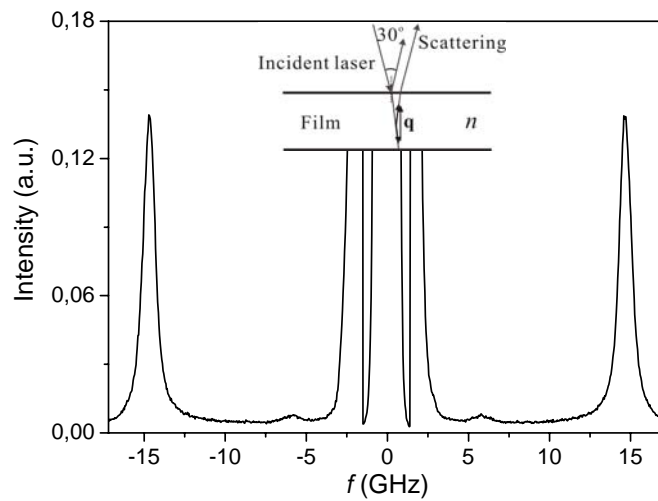


Figure 6.7 Brillouin spectrum for out-of-plane phonon propagation. At the scattering angle 150° and the reflection angle close to 15° , q ($=0.035 \text{ nm}^{-1}$) is almost perpendicular to the plane of the film. The scattering geometry is indicated in the inset. The peak at about 14.7 GHz corresponds to the longitudinal phonon propagating along the surface normal. The weak feature at about 6 GHz is the ghost of the strong longitudinal peak.

This q value corresponds to a phonon with a wavelength of about 180 nm, which should be short enough to distinguish (180 nm vs 196 nm) the mechanically different two layers. However, the single phonon spectrum of **Fig. 6.7** displaying a longitudinal wave propagating with a phase velocity in an effective medium appears to contradict the layered structure of the film. This apparent contradiction with the in-plane phonon propagation (**Fig. 6.2** and **6.3**), where the two layers do exhibit distinct in-plane sound velocities, is easily removed by assuming a sufficiently low elastic contrast between the two layers in the direction of the film normal. For the out-of-plane phonon propagation, one is actually dealing with a 1D phononic crystal. The phononic band structure of this 1D phononic crystal can be calculated

by FEA with the use of the same sets of elastic constants for PMMA and PET, which however reveals negligible small Bragg gaps at the first Brillouin zone boundary, $q_{\perp} = 0.0196 \text{ nm}^{-1}$. To a good approximation, the phonon propagation along the film normal is isotropic, in accordance with the single experimental phonon spectrum (**Fig. 6.7**). The experimental and theoretical phase velocities of this single phonon are 2650 m/s and 2580 m/s, respectively. The small difference is not significant considering the uncertainty of the experimental velocity due to the assumption of $n=1.5$. An increase of n would further narrow this disparity. The absence of the anticipated transverse phonon in the spectrum of **Fig. 6.7** is rationalized by the weak elasto-optic coupling at this large scattering angle ($I \sim \cos^2(\theta/2)$, θ is the scattering angle) [74], which leads to very low scattering intensity from transverse waves.

Chapter 7

Elastic excitations in dry colloidal crystals

7.1 Introduction

In Chapter 5 and 6, we have seen complex elastic excitations in thin polymer layers. In the next two chapters, we switch to another class of commonly encountered, yet very important composite material systems, the colloidal crystals. As a result of the presence of numerous spherical inclusions, traveling acoustic waves in colloidal crystals usually suffer from strong multiple phonon scattering in addition to the interference effect brought about by the periodic structure, leading to rather complicated wave propagation behavior. In colloidal suspensions or polycrystalline crystals, BLS has revealed the presence of various excitations related to particle eigenmodes [116,117], “Bragg” modes and mixed modes [117] due to acoustic phonons/particle eigenmodes hybridization. Despite the significance of the particle eigenmodes in affecting wave propagation in colloidal systems, a clear and direct observation of the eigenmodes of colloidal particles was only achieved until recently. In a suspension of monodisperse spherical copolymer micelles, using BLS Fytas et al. observed the vibration mode localized within the individual micelles [118]. A succeeding big step was made when BLS was applied by Kuok et al. to synthetic opals consisting of close-packed, monodisperse silica nanospheres (in air), where they observed various localized particle eigenvibrations [119,120]. However, in the case of silica, due to its high compressibility, the intensity of the inelastically scattered light is weak and the quality of the spectrum is less satisfactory, hence probably many eigenmodes are still missing and some fine spectral features cannot be well recognized. In addition, the elastic parameters deduced from the

fitting of the experimental data [119,120] show dramatic deviations from that of bulk fused silica which exceed what would be expected from any confinement effect at this scale. The authors attribute this to the inhomogeneities of the particles, preventing, however, a vigorous comparison between theory and experiment.

To explore thoroughly the fundamental particle vibrations, BLS was applied to dry (in the sense that the particles are immersed in air) colloidal crystals made of soft PS particles anticipating stronger scattering intensity intrinsic to the higher compressibility of the much softer particles. Furthermore, using newly synthesized amorphous CaCO_3 powders as an example, it will be shown that the detection of eigenmodes with the use of BLS is a very effective method for extracting elastic properties and even size distribution of submicrometer particle aggregates.

7.2 PS colloidal crystal film preparation

The PS dry colloidal films used in this work were kindly furnished by my collaborator Jianjun Wang at MPIP. There are two steps to making a colloidal film: the particle synthesis and the self-assembly of the particles into colloidal crystal film. These steps are briefly described below.

The PS particles were prepared by emulsion polymerization in ultra-pure water (Milli-Q system) with the styrene (distilled under reduced pressure before use), sodium 4-styrene sulfonate and acrylic acid monomers and the initiator ammonium peroxodisulfate being purchased from Aldrich. After mixing the components according to the desired particle size (details see Ref. [121,122]) the polymerization was run while stirring in a nitrogen atmosphere for 24 h at 348 K. The particles were purified from large agglomerates by filtration through a standard paper filter followed by six cycles of centrifugation and redispersion to remove low molecular weight impurities.

To obtain the colloidal crystal film, a recently developed vertical lifting deposition method [121,122] was employed, in which a clean glass substrate, 1.5 cm \times 3 cm, was lifted from the colloidal suspension (0.5%-2.5% w/v) by a home made dipping device at 308 K with a typical lifting speed of about 1 $\mu\text{m/s}$. This is schematically shown in **Fig. 7.1a**. The thickness of the film depends largely on the concentration and on the lifting speed. In our

work, a thickness typically in the range of 4-10 μm was obtained. The resulting colloidal crystal has an fcc structure which can be well identified from the top and side view SEM (scanning electron microscope) images of fractured native samples (non-sputtered), as shown in **Fig. 7.1b** and **c** for the film consisting of particles with diameter $d=856$ nm. Similar SEM images were obtained for films made from particles of other sizes. The SEM images were taken on a low-voltage SEM with a LEO Gemini 1530 at acceleration voltages of 0.2-1 kV. The low-voltages, hence low energy electrons, were adopted to minimize possible damage to soft polymer materials. Before the BLS measurement, the freshly prepared colloidal film was kept in the fume hood for 24 h for completely drying.

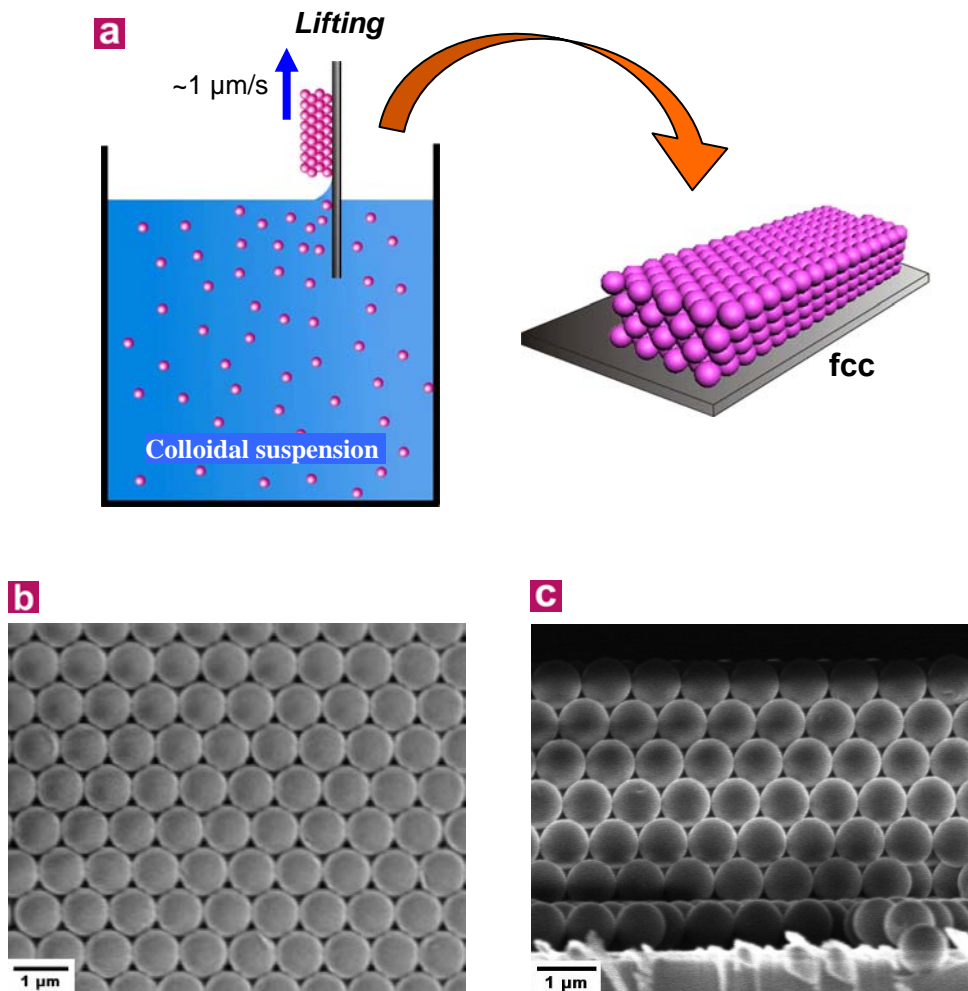


Figure 7.1 Fabrication of PS colloidal crystal films. **a**, Schematic picture of the vertical lifting deposition method. **b,c**, SEM images of a synthetic colloidal crystal film consisting of seven ordered layers of monodisperse PS spheres with diameter $d=856$ nm, top view (**b**) and side view (**c**).

The particle sizes adopted in this work were measured directly from the SEM images of native colloidal film samples as in **Fig. 7.1**. For a given sample, I measured up to 600-800 particles and the particle size and polydispersity therefore can be reliably deduced from statistic analysis. The particles were found to have good polydispersity for all sizes used (assuming a Gaussian size distribution, the variance $\sigma \leq 15$). An example of the result of the particle size measurement from the SEM images is given in **Fig. 7.2** for $d=856$ nm.

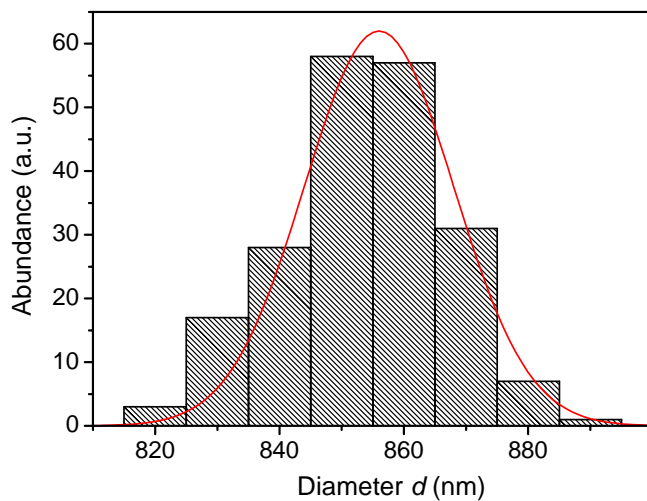


Figure 7.2 Example of particle size distribution. The particle sizes were measured from the SEM images and the size distribution can be described by a Gaussian function centered at $d=856$ nm with variance $\sigma=12$.

7.3 Results and discussion

7.3.1 Brillouin spectra

Five dry opals with different particle diameters between 170 nm and 860 nm were examined and the polarized BLS spectra recorded at a low scattering angle (10°) are shown in a semilog presentation in **Fig. 7.3a**. To encompass a broad frequency range, two spectra recorded at two different FSR (7.5 GHz and 25 GHz) were spliced together with the proper intensity ratio. In this way, the entire spectral features can be well revealed. These spectra exhibit very rich spectral features, which is uncommon in normal BLS experiments even considering the previously encountered thin layer situation where many excitations can exist. For the opals with the largest particle size, up to 21 peaks can be resolved, in contrast to the six modes observed in silica opals [119]. It is noteworthy that the frequencies and the

relative intensities of these peaks do not depend on the scattering angle (or q) and the in-plane orientation of the film.

This finding suggests that the Brillouin peaks in **Fig. 7.3a** arise from localized elastic excitations confined in individual PS particles instead of acoustic waves in the bulk material. Owing to the strong elastic form factor of the individual spheres and their larger optical contrast (refractive index difference) with the surrounding air, these PS opals exhibit strong multiple elastic light scattering. The multiple scattering is so strong that the transmitted beam becomes rather weak and sometimes hardly discernable despite the strong incident laser power (~ 50 mW) onto the sample. Therefore in such a case the scattering wavevector \mathbf{q} is ill defined, preventing the record of dispersion relations of acoustic-like modes that show q dependence.

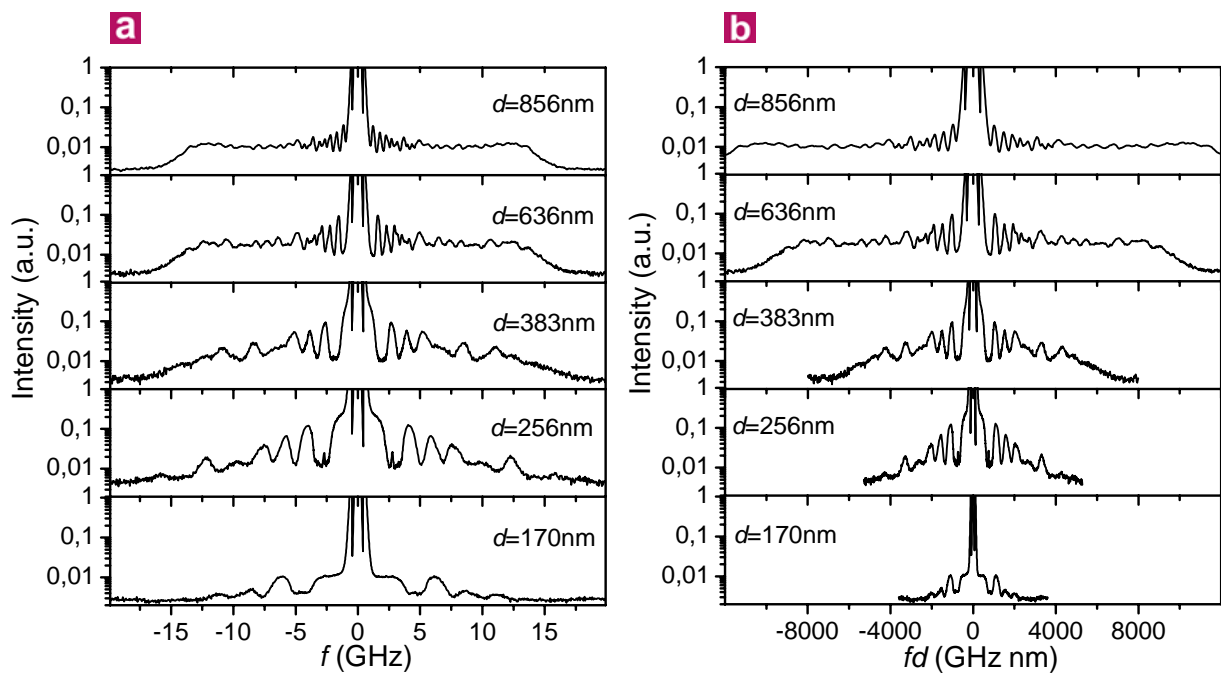


Figure 7.3 BLS spectra of PS dry opals with five different particle diameters. **a**, The original BLS spectra plotted in logarithmic intensity scale for better visualization of all spectral features. **b**, The same spectra re-plotted in reduced frequency scale, fd , the product of frequency and the particle diameter d .

It is easy to notice in **Fig. 7.3a** the similarities between the BLS spectra from opals with different particle sizes. The intrinsic connection between these spectra becomes even more evident when plotting them in reduced frequency scale as shown in **Fig. 7.3b**, where the

particle size is incorporated in the “frequency”. Although not all spectra display the same number of peaks, the resolved ones, common to all, appear at the same position in the reduced frequency scale, implying the frequency of a given mode is inversely proportional to the particle diameter, a feature characteristic of sphere vibration resonances.

There is a salient background underneath the observed peaks in the spectra of the opals with larger particle size. The background ends up at a frequency corresponding to that of the acoustic mode in bulk PS observed in back-scattering geometry, which suggests that it originates from the convolution of acoustic modes in the current PS sample at a number of different q values caused by the strong multiple light scattering. For the relatively large particles ($d=636$ and 856 nm), the particle size exceeds by a notable amount the smallest probing wavelength (~ 180 nm) of acoustic waves in the BLS experiment. Therefore to a certain degree acoustic waves can still be excited in these particles. The cutoff frequency of the background provides useful information, that is, the longitudinal sound velocity in the investigated PS particles which is found to be $c_l=(2350\pm 40)$ m/s, agreeing well with the reported sound velocity in bulk PS [123].

7.3.2 Eigenmodes identification

To identify the observed modes with the particle eigenfrequencies, the latter was computed from the “single-phonon scattering-cross-section” calculations (Section 2.5.2).

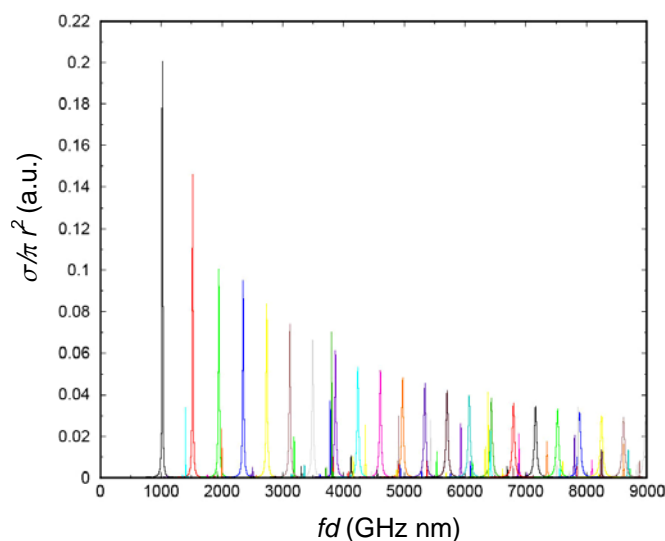


Figure 7.4 Single phonon scattering cross section of a PS sphere in air. The sharp peaks represent the strong resonances which correspond to the various particle eigenmodes. Elastic parameters: for PS, $\rho=1.05$ g/cm³, $c_l=2350$ m/s, $c_t=1210$ m/s, and for air, $\rho=0.05$ g/cm³, $c_l=340$ m/s, $c_t=0$.

The computation was performed by my collaborator Dr. R. S. Raluca at University of Crete.

A plane sound wave is considered to propagate in air and impinging onto a single PS sphere in air. As a result of the large acoustic mismatch between PS and air, the incident sound wave will be strongly scattered and sharp resonance peaks will appear in the plot of scattering cross section versus frequency as shown in **Fig. 7.4** where the reduced frequency fd is used. To reveal more clearly the resonances, the contribution from a rigid sphere of equal size has been subtracted from the calculated scattering amplitude. These resonance peaks then correspond to the eigenmodes of the PS sphere since the elastic field energy is very well localized inside the sphere. To avoid the possibility of losing a peak in the calculations (due to its almost δ -function shape), a larger mass density of 0.05 g/cm^3 was artificially used instead of the air mass density (0.00123 g/cm^3) for the surrounding medium. This introduces a broadening of the peaks but without altering their frequency position.

The computation of the single phonon scattering cross section in **Fig. 7.4** requires the knowledge of the elastic parameters of the PS sphere. We use the experimentally determined longitudinal sound velocity for the PS particle, while the value of the transverse sound velocity $c_t=1210 \text{ m/s}$ is determined by the optimal fitting of the calculated frequencies to

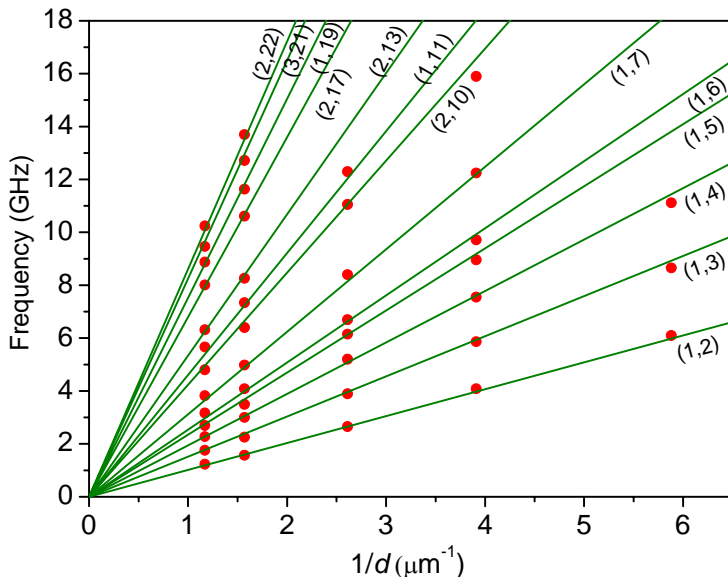


Figure 7.5 Peak frequencies of the Brillouin spectra as a function of the inverse diameter. Up to thirteen experimental frequencies (red dots) are shown to obey the theoretical $f \sim d^{-1}$ scaling (green lines). The paired numbers (i, l) denote the l th harmonic of the i th mode.

the experimental ones, which is in good accordance with the bulk PS value [123]. These theoretical calculations with a single adjustable parameter describe the experimental vibration eigenfrequencies very well as demonstrated in the frequency versus inverse diameter plot in **Fig. 7.5**, where the green solid lines are theoretical fits and the red solid dots are experimental frequencies. The comparison between the theoretical and experimental

reduced frequencies $f(i, l)d$ is given in Table 7-I, with the experimental reduced frequencies

being obtained by the least-square fit of the solid dots in **Fig. 7.5**. The q -independent nature of these modes and the excellent theoretical capture of their frequencies finally allow us to draw the conclusion that what we observed is indeed the eigenmodes of the PS spheres. As already introduced in Section 2.5.1, here each eigenmode is specified by two paired integer numbers defining the l th spherical harmonic of the i th radial mode, in analogy to atomic orbitals.

All the observed eigenmodes in our BLS experiment are spheroidal modes in as much as the purely transverse nature of torsional modes cannot couple effectively with the incident light field. The observed mode $(1, 2)$ in fact represents the lowest energy spheroidal mode for the PS elastic sphere. Based on symmetry arguments, Duval [124] has shown that, the

Table 7-I: Vibration modes of PS spheres in air

	$f(i, l)d$ (nm GHz) ^{Experimental}	$f(i, l)d$ (nm GHz) ^{Theoretical}	(i, l)
1	1040	1017	$1, 2$
2	1480	1518	$1, 3$
3	1900	1945	$1, 4$
4	2310	2348	$1, 5$
5	2480	2538	$1, 6$
6	3140	3119	$1, 7$
7	4100	4237	$2, 10$
8	4700	4607	$1, 11$
9	5290	5340	$2, 13$
10	6780	6797	$2, 17$
11	7450	7523	$1, 19$
12	8100	8247	$3, 21$
13	8730	8609	$2, 22$

only Raman-active modes of an elastic sphere are the symmetric $l=0$ and quadrupolar $l=2$ spheroidal modes, with the former producing polarized and the latter depolarized scattering light. Obviously, this theoretical prediction contradicts our experimental results. The disparity might arise from the dipole approximation assumption in the theory that the particle size is much smaller compared to the wavelength of light. Regarding the polarization of the scattered light, a direct examination is not possible in the present experiment due to the strong multiple light scattering that scrambles the polarization of both the incident and scattered light. Therefore identical (in terms of peak frequency and relative intensity)

polarized and depolarized spectra were observed. Nonetheless we tend to believe that these spheroidal particle eigenmodes lead to polarized light scattering, as the origin of the inelastic light scattering, the dynamic optical inhomogeneities, should be overwhelmingly caused by density fluctuations due to the stretching motions of the spheroidal modes which mainly modulate the diagonal elements of the dielectric tensor.

7.3.3 Particle size distribution

In addition to the frequencies of the particle vibration eigenmodes, the experimental BLS spectrum also provides information about the size distribution of these particles. The latter is reflected in the shape and width of the observed peaks. Recalling **Fig. 3a**, one can easily notice that the width of the lowest frequency peaks shows strong dependence on particle size. Moreover, the shape of the peak is asymmetric, which is more evident for the low l modes and in the spectra of the smaller particles. On the other hand, this particle size dependence is clearly diminished in the reduced frequency plot of **Fig. 3b**.

For an isolated particle at a temperature well below the T_g of PS, it can be treated to a good approximation as a perfect elastic sphere without internal losses. The absence of elastic energy dissipation should lead to very narrow spectra indistinguishable from the instrumental function. The observed broad and asymmetric line shape of the experimental peaks, in particular for the low l modes, should most probably be attributed to the finite particle size polydispersity. To verify this conjecture, I approximate the instrumental function with a Lorentzian line shape and represent the measured scattering power spectrum of a given mode by a convolution of a Gaussian distribution function of the particle size and a Lorentzian line representing the instrumental function,

$$I(\omega) = \int dx A(x) \frac{\Gamma(x)}{(\omega - \omega(x))^2 + \Gamma(x)^2} \frac{\exp[-(x - D)^2 / 2\sigma^2]}{\sqrt{2\pi}\sigma} \quad (7.1)$$

where $A(x) \approx A_0$, $\omega(x) = 2\pi c_1 / x$ is the peak frequency of the Lorentzian line and the relevant half-width at half maximum $\Gamma(x)$ is a constant obtained from the measured instrumental line width which corresponds to ideal monodisperse particles without internal losses.

The lowest-frequency mode (1, 2) is most intense and also well separated from other modes. Hence it was chosen to demonstrate the point. The experimental line shape for the mode (1, 2) of the smallest (170 nm) and largest (856 nm) PS spheres can be well reproduced by Eq. (7.1) as shown in **Fig. 7.6**, using a fixed $c_1=1020$ GHz nm (the slope of the solid line in **Fig. 7.5**) and the variance σ as the only adjustable parameter besides the amplitude A_0 . The different experimental line shape of the mode (1, 2) for these two diameters is the result of the combined effect of the $f \sim 1/d$ dependence and the different particle size polydispersity ($\sigma=14$ and 10) with the larger particle possessing a lower σ . The obtained values of the variance conform to the size distribution extracted from the SEM images. The polydispersity induced broadening of the peak has been further confirmed by a recent BLS experiment on a single silica sphere [125]. Albeit the particle size distribution is found to be the most important reason responsible for the experimental line shape and width, there are other possibilities that could also broaden the peak. In reality, the particles are never ideally isolated and with a stress-free boundary. Weak energy leakage could happen, possibly leading to a broader intrinsic line width than the instrumental width. This effect should be more pronounced for the smaller size particle due to the larger surface-to-volume ratio, which may explain the resulting polydispersity of the 170 nm particles being slightly larger than that from the SEM images.

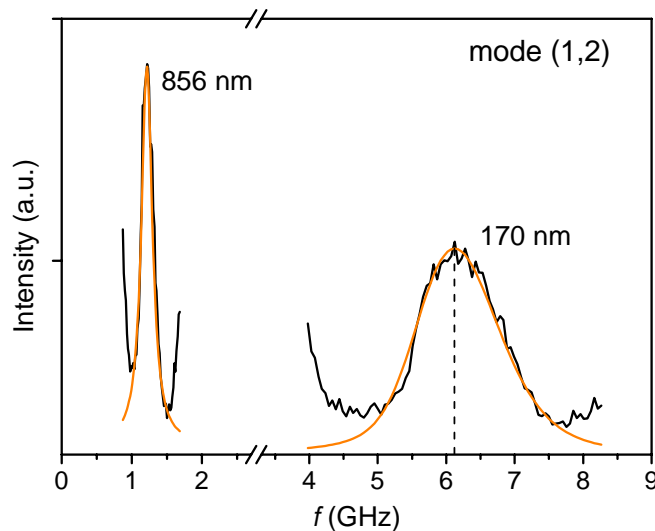


Figure 7.6 Representation of the experimental spectrum of the mode (1, 2). The lowest-frequency mode (1, 2) for the smallest and largest PS spheres are represented by Eq. 7.1 with the variance $\sigma=14$ and 10, respectively. The orange lines are the theoretical fits. For the smallest spheres, a vertical dashed line is used to make the asymmetry of the peak more apparent.

7.3.4 The low-frequency continuum

Another important spectral feature we have not been addressed so far is the existence of a low-frequency continuum in the measured BLS spectra, e.g. those from $d=170$ nm and $d=256$ nm, in **Fig. 7.3**. Like the eigenmodes, this low-frequency continuum also exhibits a particle size dependence, as the width is approximately proportional to the inverse particle diameter. This rationalizes the vanishing of this continuum for the larger particles. Two possible reasons might be responsible for this unexpected spectral feature: slow lattice dynamics and/or the “eigenmodes” of small particle aggregates.

The lattice dynamics postulation originates from the realization of possible coupling forces between adjacent spheres, e.g. the capillary neck-based restoring forces owing to the presence of a condensed thin water film between particles or some polar and chargeable groups on the surface of these particles, which could in principle lead to overdamped shear lattice mode. However, to match the experimental observation, the lattice dynamics must be very fast, still in the GHz range. This frequency is unrealistically high based on the measured high frequency shear modulus from colloidal crystals [126,127] which suggests that the frequency of the lattice vibration is of the order of tens of KHz. As we will see in the next chapter, this low-frequency continuum disappears after introducing a viscous fluid into the interstices of these particles, again disfavoring the lattice dynamics contribution.

It seems reasonable that the “eigenvibration” of some particle aggregates could be the origin of this unexpected dynamics. In the present colloidal systems, two or more particles might “stick together” due to forces between them and form larger “particles”. These “heavier particles” can vibrate like a single particle but with expectedly lower eigenfrequencies, which naturally accounts for the size-dependent effect. In addition, a temperature-dependent (up to PS $T_g \sim 373$ K) measurement shows that the intensity of this low-frequency continuum is intimately related to the intensity of the numerous single-particle eigenmodes, which contradicts the expectation if the presence of the continuum is caused by the lattice dynamics relying on the condensed thin water layer between the particles.

7.4 An application of the particle eigenfrequencies

7.4.1 Introduction

The BLS detection of particle vibration eigenmodes and the subsequent theoretical capture of the eigenfrequencies by the “single-phonon scattering-cross-section” calculations, allow for the determination of unknown material elastic parameters. The continuing advancement of nanofabrication has boosted the emergence of a variety of nanoobjects with well-defined shape and monomodal size distribution. Their micromechanical characterization usually remains a challenge, which however can be addressed by the novel optical approach developed here. In the following let’s see an example of an elegant application of this method for the determination of the mechanical strength of amorphous CaCO_3 .

Amorphous CaCO_3 has been identified as a precursor to its crystalline modifications calcite, vaterite, and aragonite in biomineralization [128,129]. Even some life forms have been found that preserve glassy CaCO_3 as part of their skeleton. Little is known about the physical properties of amorphous CaCO_3 since a reproducible synthesis that produces a regular particle shape became available only very recently. This synthesis in which dialkyl carbonate in dilute aqueous solution serves as a source of CO_2 that is homogeneously formed in the medium produces spherical particles (droplets) of amorphous CaCO_3 of monomodal size distribution with diameters in the range between 400 and 1500 nm. The precise diameter is subject to control parameters such as temperature of formation, rate of CO_2 production, and whether surfactants are added to stabilize droplets of smaller size. Amorphous CaCO_3 as produced exists in a metastable glassy state and contains water. The approximate composition as obtained from reaction is $\text{CaCO}_3 \cdot 0.5\text{H}_2\text{O}$ [130]. Residual water can be removed by careful drying, and water-free glassy CaCO_3 particles in the form of colloidal powders are obtained that are stable against recrystallization up to temperatures around 553 K. At this temperature, calcite starts to form. CaCO_3 powders obtained from calcite play an important role as fillers and modifiers in poly(olefine) composites and in pharmaceutical preparations. One could imagine that amorphous CaCO_3 that is easily synthesized directly in a monomodal particle size distribution could become an important material in these areas of application.

7.4.2 Results

The CaCO_3 particles used in this work were prepared by my collaborator Micheal Faatz at MPIP. To make the BLS measurement possible, freshly prepared powder of CaCO_3 particles was dispersed on a glass slide to form a thin white layer of colloidal spheres. A typical SEM image is shown in **Fig. 7.7**, and these particles can be reasonably well described as spherical particles in spite of the deviation of from an ideal spherical shape. As in the case of PS particles, the average particle size and the polydispersity can be extracted from the SEM images, and these particles show monomodal size distribution.

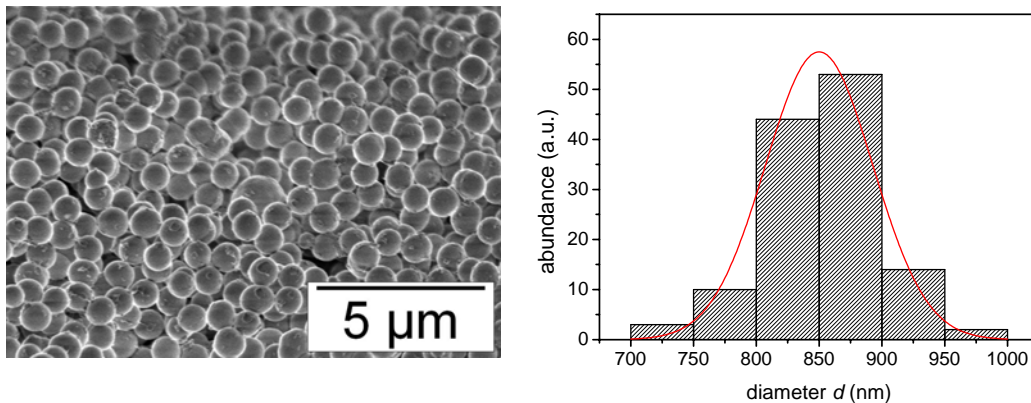


Figure 7.7 SEM image of amorphous CaCO_3 particles. The CaCO_3 particles used for BLS measurements have an approximately spherical shape. The averaged particle size and polydispersity can be extracted from the SEM images as shown here for the $d = 850$ nm sample having a Gaussian size distribution with the variance $\sigma = 43$.

Four samples with different particle sizes in the range of 400~1300 nm were measured, and the resulting BLS spectra display several doublets around the central Rayleigh line as shown in **Fig 7.8a** for the sample with an average particle size $d = 850$ nm recorded at 25 GHz FSR. We already know that these q -independent modes are due to particle eigenvibrations, and the task is then to find out the elastic parameters of these particles by fitting of the experimental frequencies with values derived from theory. Like for the PS opals, the longitudinal sound velocity can be obtained from the cutoff frequency of the background (see Section 7.3.1) which yields $c_l = (5600 \pm 200)$ m/s. The calculations were then run with two floating parameters: the density ρ and the transverse sound velocity c_t . By choosing $\rho = 1.9$ g/cm³ and $c_t = (2700 \pm 100)$ m/s, a very good agreement between theory (solid lines in **Fig. 7.8b**) and experiment (orange solid dots in **Fig. 7.8b**) can be obtained for all observed modes. It is noteworthy that a value for the density of amorphous CaCO_3 of 1.9

g/cm^3 was also found by Ballauf et al. [131] recently who employed a totally different way of preparation. The experimental and theoretical reduced frequency values are listed in Table 7-II. The fact that one transverse velocity suffices to reproduce all observed eigenfrequencies is a strong support of the amorphous state of the CaCO_3 spheres in agreement with the X-ray scattering data [130]. For the crystalline CaCO_3 (calcite), the reported values are 7400 m/s for the longitudinal and 2900 and 4400 m/s for the two transverse sound velocities [132].

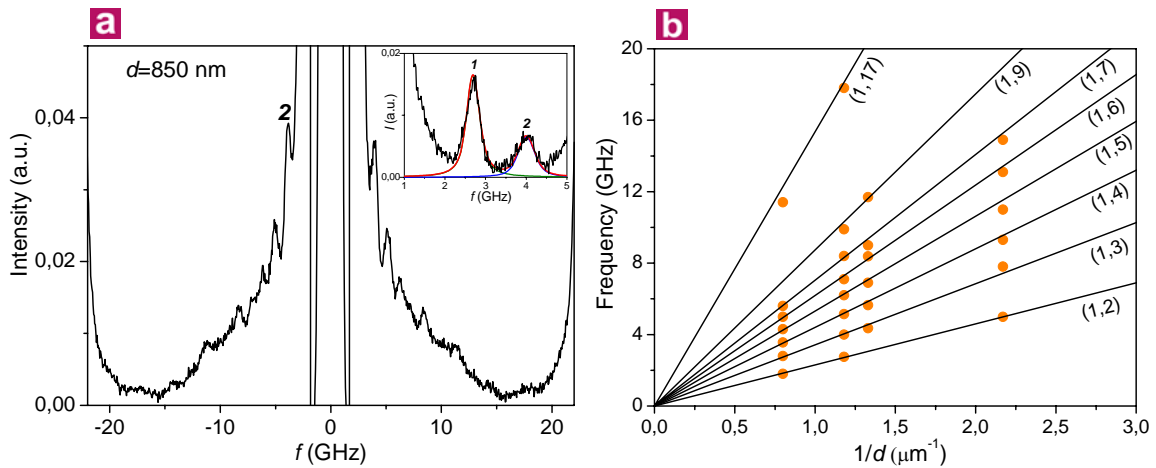


Figure 7.8 BLS measurements of amorphous CaCO_3 particles. **a**, BLS spectrum of amorphous CaCO_3 particles with average particle size $d=850$ nm, recorded at FSR 25 GHz. Mode 1 is buried in the strong elastic Rayleigh wing in the main plot, which however is clearly revealed in the spectrum in the inset recorded at a higher resolution (7.5 GHz) FSR. The two lowest-frequency modes, 1 and 2, are described by convoluting a Gaussian particle size distribution with a Lorentzian natural line shape, as shown in the inset. **b**, The eigenfrequencies of amorphous CaCO_3 particles are plotted as a function of the inverse diameter. The dots are experimental points and the solid lines are simulations.

Table 7-II: Vibration modes of amorphous CaCO_3 spheres in air

	$f(i, l)d$ (nm GHz) ^{Experimental}	$f(i, l)d$ (nm GHz) ^{Theoretical}	(i, l)
1	2310 ± 50	2299	1, 2
2	3550 ± 110	3422	1, 3
3	4270 ± 180	4402	1, 4
4	5060 ± 200	5312	1, 5
5	6050 ± 240	6185	1, 6
6	6850 ± 300	7041	1, 7
7	8640 ± 350	8734	1, 9
8	14960 ± 600	15347	1, 17
9	17920	17807	1, 20
10	21430	21016	2, 24

With the obtained sound velocities, the Poisson ratio $\sigma = (c_l^2 - 2c_t^2) / 2(c_l^2 - c_t^2)$ of these amorphous CaCO_3 spheres is found to be 0.35. The Young modulus $E = \rho c_l^2 (1 + \sigma)(1 - 2\sigma) / (1 - \sigma)$ and shear modulus $G = \rho c_t^2$ can be computed to be 37 GPa and 14 GPa, respectively. The Young modulus is comparable but slightly lower than the range of moduli found for common inorganic glasses (60-150 GPa) [133] and is about 1 order of magnitude larger than the commonly encountered values for glassy polymers (3-5 GPa).

Following the same procedures shown in Section 7.3.3, I could successfully reproduce for the $d=850$ nm sample the experimental line shape of the modes $(1, 2)$ and $(1, 3)$ with the same variance $\sigma=35$ as illustrated in the inset to **Fig. 7.8a**. The resulting variance of 35 coincides reasonably well with the result from SEM images. Note that the spectrum in the inset of **Fig. 7.8a** was measured under the same experimental condition at 7.5 GHz FSR, which allows the resolving of the lowest-frequency eigenmode $(1, 2)$ absent in the main spectrum recorded with a lower resolution (25 GHz) FSR.

Chapter 8

Elastic excitations in wet colloidal crystals

8.1 Introduction

The name “wet colloidal crystals” is used to distinguish from the “dry colloidal crystals” encountered in the preceding chapter, meaning that the colloidal crystals are immersed in a liquid instead of air. The creation of wet colloidal crystals is aimed at searching for possible phononic bandgaps in the hypersonic frequency range. In spite of the great importance of hypersonic phononic crystals as mentioned in Chapter 1, an experimental identification of such a hypersonic gap is not yet achieved. To shift the bandgap to the hypersonic frequency range, the creation of periodic patterns is necessary at the submicrometer scale, thus imposing substantial demand on fabrication and characterization techniques that are currently being developed. For example, holographic interference lithography has recently been used to fabricate polymer-based hypersonic phononic crystals [38,134]. The phononic dispersion relation of such a single-crystalline triangular array of cylindrical holes in an epoxy matrix was recently measured by BLS [38]. These measurements, however, did not reveal the anticipated bandgap, which was probably due to the simultaneous strong optical diffraction.

On the other hand, both the dry and wet colloidal crystals fabricated by self-assembly in principle also represent phononic crystals because of the periodically varied elastic parameters and/or density associated with these systems. The detailed phononic properties depend on the lattice type, filling ratio and elastic combinations. Owing to the strong multiple light scattering, traveling elastic waves in the dry opals cannot be examined with BLS even though the existing large elastic contrast probably leads to a sizeable bandgap. A

way to overcome this difficulty is to infiltrate the dry opals with a fluid having a similar refractive index to the colloidal particles to eliminate the multiple light scattering.

BLS examination of acoustic wave propagation in colloidal systems dates back to the early nineties of the last century, and very uncommon acoustic excitations have been observed. For example, in colloidal suspensions Sheng et al. [116,135] found surprisingly two distinct propagating acoustic modes. In polycrystalline colloidal crystals, Fytas et al. [117,136,137] observed very rich acoustic excitations, including both acoustic-like and optic-like modes. All these unusual observations are related to the fact that the relevant acoustic wavelength is comparable to the colloidal particle size and these spherical particles represent strong resonant units. In the case of polycrystalline crystals, the structure influence is also reflected [117]. However, due to the polycrystalline nature of the system, no clear Bragg gap has ever been observed. Now the progress in colloidal crystal fabrication technique enables the production of large domain single crystalline crystals, e.g. the dry opals we have seen, making a careful examination of Bragg gap effect possible.

In this chapter, the first experimental observation of a hypersonic Bragg gap in fcc PS wet colloidal crystals will be demonstrated. Depending on the particle size and the sound velocity in the infiltrated fluid, the frequency and the width of the gap were successfully tuned. When the elastic contrast between the matrix and the particles is sufficiently large, additional gaps due the hybridization of the acoustic mode and the particle resonances appear, revealing rather complex elastic excitations in such phononic systems.

8.2 Experimental

Using the previously obtained PS dry opals as precursor, the wet colloidal crystals used in this study can be easily prepared. The fabrication process is summarized in **Fig. 8.1**. The dry opal (**I**) film was infiltrated with a viscous, non-evaporative liquid (non-solvent for PS) by pipetting a few drops onto the sample. Any liquid excess was blown off the crystal with an air jet treatment for ~ 4 h to result in the final sample to be measured. In this way a liquid-infiltrated opal (**II**) was obtained. Three different fluids (glycerol, Merck; silicon oil, Wacker-Chemie; poly(dimethylsiloxane) (PDMS), anionic polymerization, MPIP, $M_n=979$) were used in this work. After the infiltration the previously opaque film becomes transparent, and a well-defined scattering wavevector \mathbf{q} can be attained.

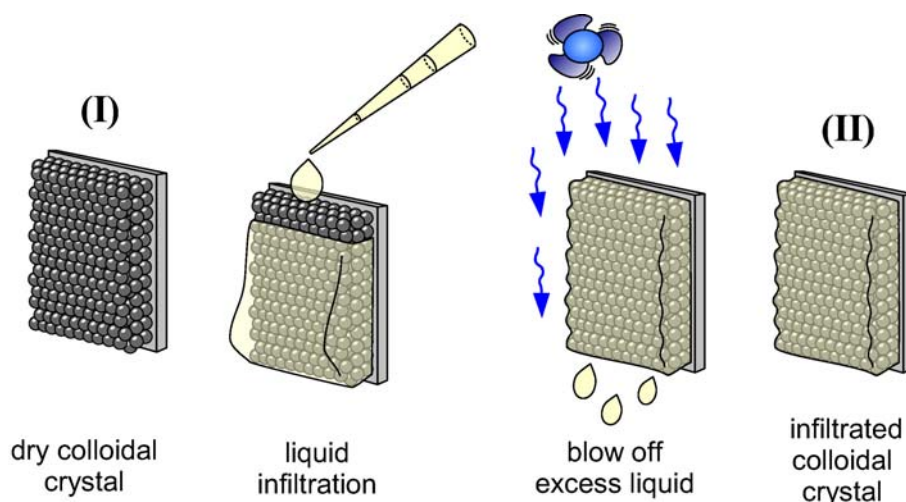


Figure 8.1 Fabrication of wet colloidal crystals. *The wet opal was prepared by infiltrating the dry opal with a fluid and removing the excess liquid with an air jet.*

The scattering geometry adopted here was the same as that used for the thin layer systems where the scattering wavevector \mathbf{q} is parallel to the film plane and its magnitude is independent of the refractive indices of the opal film and the glass substrate. Specific to the fcc colloidal crystal under consideration, the wavevector \mathbf{q} is parallel to the (111) lattice plane of the crystal as indicated in **Fig. 8.2a**. Unlike in homogeneous systems where the momentum conservation condition in the light scattering process is $\mathbf{q}=\mathbf{k}$ with \mathbf{k} being the phonon wavevector, in hypersonic crystals, as requested by the translational symmetry of the lattice, the momentum conservation has to be modified by introducing a

reciprocal lattice vector \mathbf{G} so that $\mathbf{q}=\mathbf{k}+\mathbf{G}$. Since phonons with wavevectors \mathbf{k} and $\mathbf{k}+\mathbf{G}$ represent the same wave according to Bloch's theorem, the phononic properties of a hypersonic crystal can be revealed by recording the dispersion relation $\omega(\mathbf{q})$. In this case, the direction of \mathbf{q} is important because of the presence of the reciprocal lattice vector \mathbf{G} in the momentum conservation.

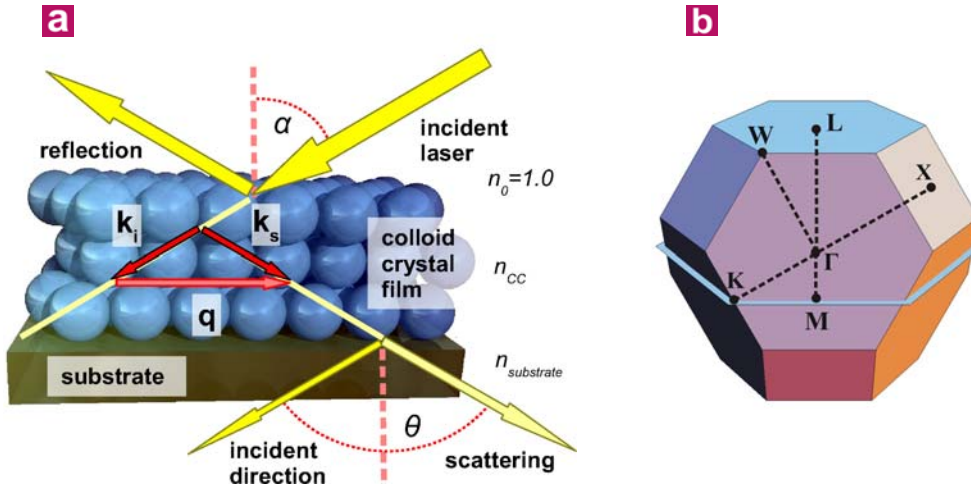


Figure 8.2 Scattering geometry and the first Brillouin zone. **a**, The scheme shows the different light beams (incident, reflected, transmitted and scattered) and the wavevectors (\mathbf{k}_i , \mathbf{k}_s) for the incident laser and the scattered light defining the scattering wavevector \mathbf{q} in the (111) plane of the fcc crystalline colloidal film. **b**, The truncated octahedron with its center at Γ represents the first Brillouin zone (BZ) of the fcc crystal. The plane intersecting the BZ is the plane in which the experimental \mathbf{q} is confined.

It is desirable to probe the dispersion relation $\omega(\mathbf{q})$ along the high symmetry directions in the reciprocal space, since the phononic bandgap is usually manifested in the dispersion diagrams along these directions as seen in Section 2.5. It can be shown that the first Brillouin zone (BZ) of the fcc lattice (of which the reciprocal is bcc) is a truncated octahedron with its center denoted by Γ and the corresponding highest symmetry directions pointing from Γ to the zone face centers, i.e. along Γ -L and Γ -X as shown in **Fig. 8.2b**. In the scattering geometry of **Fig. 8.2a**, all possible experimental \mathbf{q} vectors are confined in a plane, whose intersection with the BZ forms a hexagon (**Fig. 8.2b**). Therefore it is unlikely to follow strictly the phonon propagation along Γ -L or Γ -X. Nevertheless, the direction of \mathbf{q} can be selected close to Γ -L, as along Γ -M, where M denotes the edge center of the hexagon defined here above. In this case, the probed dispersion diagram should show no essential difference

from the Γ -L direction, since on a given zone face the band splitting near the face center is roughly constant, as can be shown by first-order perturbation theory [70].

8.3 Results and discussion

8.3.1 Hypersonic Bragg gap formation

The wet opal made up of close-packed PS spheres (fcc) with the interstices fully occupied by the liquid represents a hypersonic crystal of solid inclusions in a fluid host, as shown in the SEM image in **Fig. 3c** for the opal with $d=256$ nm infiltrated by silicon oil.

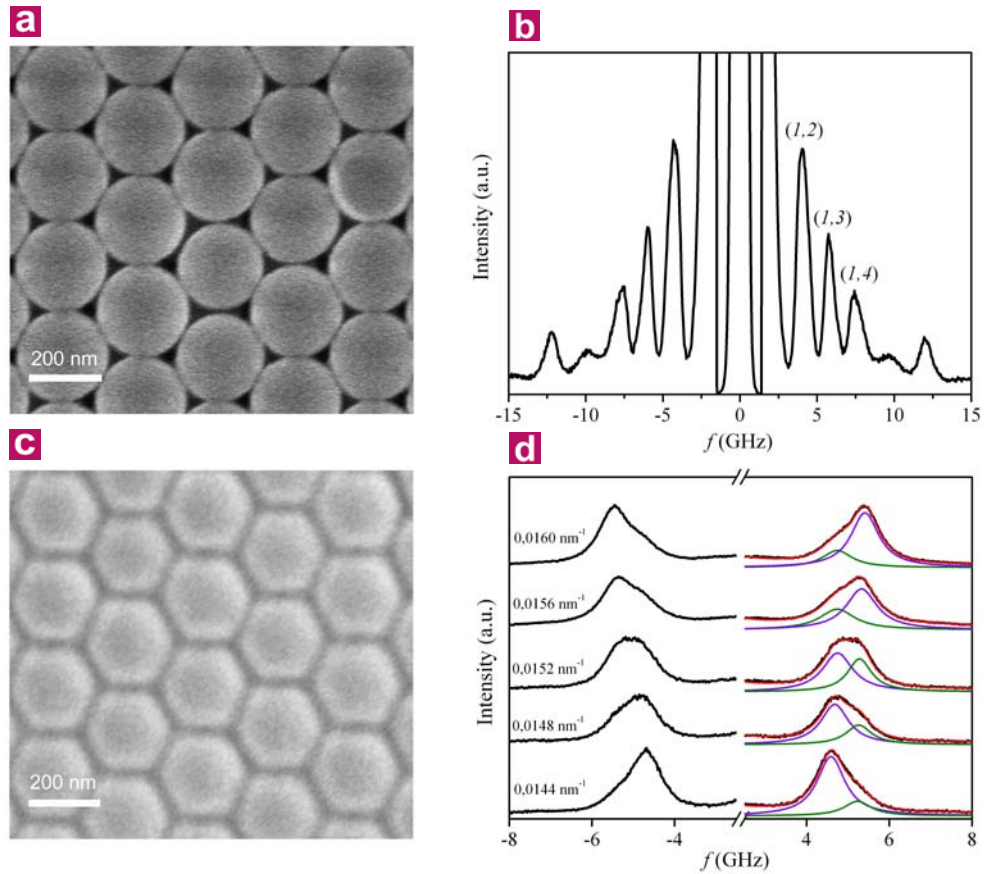


Figure 8.3 Brillouin light scattering spectra of dry and wet opals. **a,c**, SEM top-view images of the fcc dry opal consisting of polystyrene (PS) spheres **(a)** and the corresponding wet opal **(c)** after silicon oil infiltration. The particle diameter is 256 nm. **b**, BLS spectrum of the dry opal exhibiting no q dependence. **d**, BLS spectra of the wet opal at five different q values near the Brillouin zone (BZ) boundary along Γ -M. The observed double peak feature is well reproduced by two Lorentzian shapes.

The resulting BLS spectrum differs greatly from that of both the dry opal where several q -

independent modes appear and the pure silicon oil in which only a single longitudinal phonon exists. For the present silicon oil infiltrated wet opal, at low q a single peak is observed. As q increases and approaches the BZ boundary, a double-peak feature shows up as demonstrated in **Fig. 8.3d** by the polarized BLS spectra taken at five different values of q near the BZ boundary along the Γ -M direction. For comparison, a SEM image of the dry opal before infiltration and the corresponding BLS spectrum are also given in **Fig. 8.3a** and **b**, respectively. Note that the spectrum representing the eigenmodes in **Fig. 8.3b** is now plotted in linear intensity scale.

The observed double-peak feature in **Fig. 8.3d** can be well represented (red lines) by a double Lorentzian line shape (violet and green lines, convoluted with the instrumental function). The violet line indicates the mode with acoustic-like behavior in a sense that this mode will be the only preserved mode whose frequency increases linearly with q if the Bragg-gap effect vanishes. Note that the red lines incorporate also the contribution of a Lorentzian peak centered at $f=0$ GHz responsible for the central Rayleigh wing. The splitting of the single peak feature (not shown in **Fig. 8.3d**) at low q (long wavelength) into double peaks across the BZ boundary is a typical Bragg-gap effect due to the band folding into the first BZ. The observed acoustic phonons are longitudinally polarized, as they disappear in the depolarized BLS spectrum. However, the concurrent absence of the transverse phonons in the depolarized spectrum is consistent with the nature of this phononic system as the infiltrated fluid does not support shear waves.

A more complete knowledge of the phonon propagation can be obtained by referring to the measured dispersion relation $\omega(\mathbf{q})$ as depicted in **Fig. 8.4**. The two dashed gray lines indicate the acoustic phonon propagation in pure PS and silicon oil, measured independently. The slope of these lines yields the sound velocity in the respective medium, and c amounts to (1400 ± 25) m/s in silicon oil. In the hypersonic crystal, only one longitudinal acoustic phonon branch is observed at low frequencies. The corresponding dispersion curve, $\omega(\mathbf{q})$, is linear and thus describes sound propagation in a homogeneous effective medium, as anticipated for long wavelengths exceeding the lattice spacing. The slope of this line yields an effective sound velocity $c_{\text{eff}}=(1950\pm 40)$ m/s, which is intermediate between the sound velocities in the two component materials. As q approaches the BZ boundary, the linear q -dependent frequency growth ceases and the acoustic branch starts to bend, the frequency increase tendency resumes only after some frequency interval. The emergence of such a

frequency interval in fact represents the most striking feature of the dispersion relation, that is, the presence of a clear Bragg gap at frequency 5 GHz with a width about 0.4 GHz for $q \approx 0.015 \text{ nm}^{-1}$ which matches the distance Γ -M. Correspondingly, propagation of hypersonic phonons with frequencies within the marked blue region in **Fig. 8.4** is forbidden in the present wet opal with a sound velocity ratio of about 1.7 between the particle and the fluid. It is remarkable that, after infiltration, no particle eigenmodes are observed (cf **Figs. 8.3b** and **d**), which should relate to the weaker elastic contrast between the constituent media of the wet opals and hence stronger leakage of the elastic field energy into the surrounding liquid. In general, depending on the elastic contrast, the eigenmodes could have significant impact on phonon propagation in colloidal crystals, e.g., lead to a hybridization gap between the continuum acoustic band and the $l=2$ resonance band as predicted theoretically [138]. This kind of acoustic-and-eigenmode hybridization phenomenon will be encountered later.

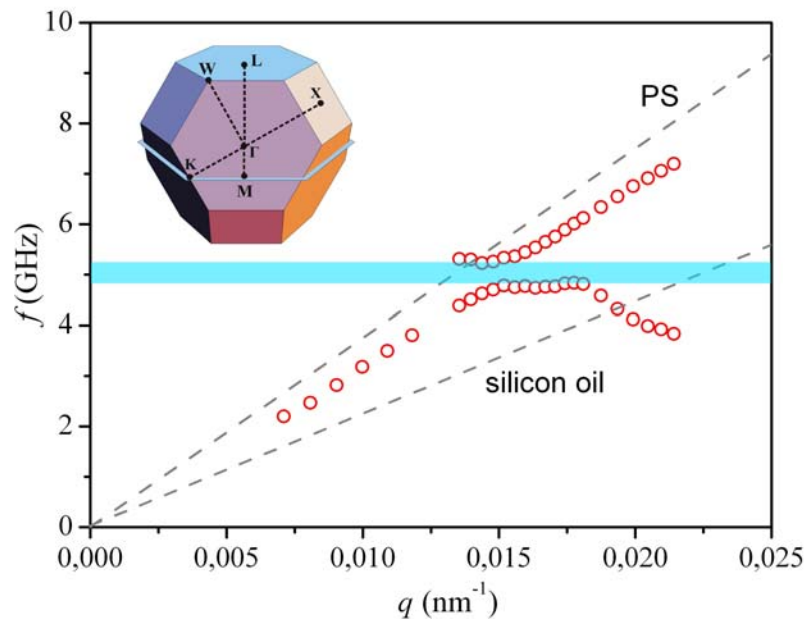


Figure 8.4 Experimental dispersion relation of the longitudinal phonon propagation in the wet opal along Γ -M. The red open circles are experimental frequencies from the wet opal, and the two dashed grey lines denote the acoustic phonon propagation in pure PS and silicon oil. The highlighted blue region indicates the observed hypersonic bandgap. Inset: The truncated octahedron with its center at Γ represents the first BZ of the fcc crystal. The plane intersecting the BZ is the plane in which the experimental \mathbf{q} is confined.

8.3.2 Hypersonic Bragg gap tuning

The width of the phononic bandgap, in general, increases with the difference in the densities and sound velocities of the component materials. In the case of our colloidal

crystals, it is the sound velocity contrast that matters since most soft materials have comparable low densities. Hence, the gap width in **Fig. 8.4** should depend on the elastic contrast between the fluid matrix and the PS particles. In addition to silicon oil, glycerol and

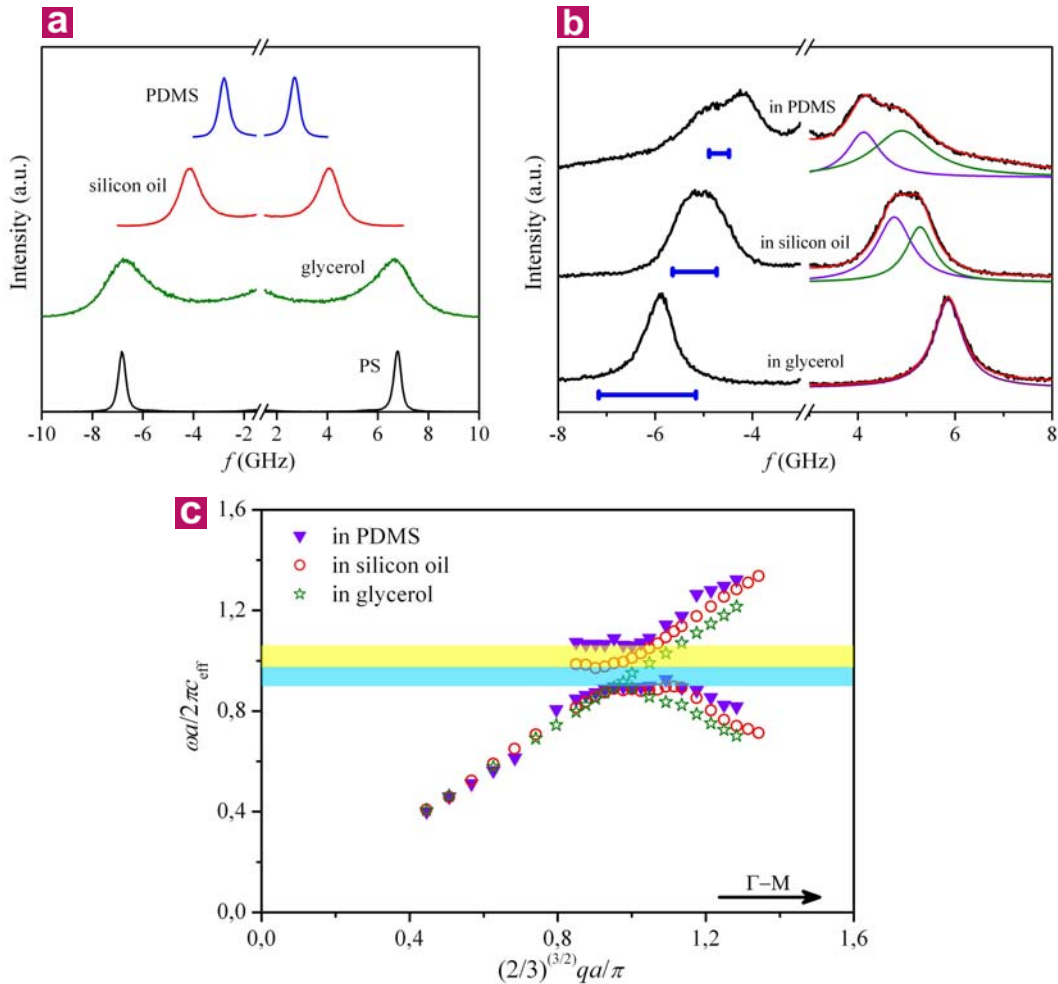


Figure 8.5 Band gap tuning by different infiltration. **a**, Examples of BLS spectra of the pure matrices and bulk PS, recorded at $q \approx 0.017 \text{ nm}^{-1}$. **b**, BLS spectra of three PS fcc wet opals infiltrated by different fluids. All spectra were taken at $q = 0.0152 \text{ nm}^{-1}$, i.e. the BZ boundary along Γ -M. The separation of the two constituent peaks (violet and green lines) of the observed double peak spectral feature reflects the width of the band gap. The blue bars represent the full width at half maximum of the single BLS peak measured at the same q in the corresponding pure fluids. **c**, Dispersion relations in a reduced $\omega a/2\pi c_{\text{eff}}$ vs $(2/3)^{3/2} qa/\pi$ presentation where c_{eff} is the effective medium phase sound velocity for the three PS infiltrated colloidal crystals, a is the lattice parameter and $(3/2)^{3/2} \pi/a$ is the distance Γ -M in reciprocal space. The marked regions indicate the phononic gaps in the silicon oil (blue) and in the PDMS (blue plus yellow) infiltrated opals. There is no discernible gap in the opal infiltrated with glycerol.

low molecular mass PDMS were also used as matrix fluids, both of which have notably different sound velocities from silicon oil. In PDMS, $c = (1050 \pm 20) \text{ m/s}$ is virtually q -independent whereas in glycerol c increases from 2000 m/s at ultrasonic to 2500 m/s at

hypersonic frequencies due to structural relaxation in the GHz frequency range at ambient temperature [139]. The sound velocity in these three matrix fluids was computed from the respective dispersion curve obtained from their BLS spectra, e.g. as shown in **Fig. 8.5a** in which all spectra were recorded at similar q . For comparison, the spectrum of a bulk PS sample is also shown. The unusually high sound velocity in glycerol (comparable to that in PS) is mainly due to its remarkably strong hydrogen-bonding network that slows down the structural relaxation, i.e. from the sub-THz to the GHz domain, thus leading effectively to a solid-like behavior at hypersonic frequencies. The very different phonon attenuation in these fluids is directly reflected in the line width of their BLS spectra and this disparity could help understand and ultimately control the losses in phononic crystals.

The influence of the fluid matrices on the bandgap becomes apparent in the Brillouin spectral shape in **Fig. 8.5b**, recorded at the BZ boundary ($q=0.0152 \text{ nm}^{-1}$) along Γ -M for three phononic crystals with different liquid infiltration. The elastic contrast between PS and the liquid matrices clearly controls the splitting of the two peaks and hence the width of the gap. In the PDMS opal, the two peaks exhibit the largest separation, in contrast to the glycerol opal where only a single peak is discernible suggesting a negligibly small gap. This clear trend follows the elastic contrast between PS and the pure liquids reflected in **Fig. 8.5a**. There is no obvious correlation, however, between the line width in the phononic crystals and that in the corresponding infiltrated liquids, marked by the blue bars, which were measured at about the same q . Instead, the phonon damping in the opal infiltrated by a fluid with strong sound attenuation, e.g. glycerol, is significantly suppressed, and vice versa. Since the attenuation of acoustic waves in glassy PS is very weak, as indicated by the narrow Brillouin peak (**Fig. 8.5a**), the origin of the hypersonic sound attenuation in the phononic crystals and in the pure matrix fluids should be different. In the former, the attenuation of phonons appears to relate to the elastic mismatch between the matrix fluid and PS particles as it increases with the elastic constant contrast. Large elastic contrast leads to strong scattering of phonons at the interface between the component materials. On the other hand, the stronger the scattering of phonons the shorter the mean free path is, and thus the Brillouin line width increases.

The successful tuning of the bandgap in hypersonic phononic colloidal crystals by means of different infiltration media is even more apparent in the combined dispersion relations of **Fig. 8.5c**. These are plotted in reduced scales, $\omega a/2\pi c_{\text{eff}}$ vs $(2/3)^{3/2} qa/\pi$, where

c_{eff} is the effective medium phase sound velocity for the three wet opals, a is the lattice constant of the fcc crystal ($a = \sqrt{2} d$) and $(3/2)^{3/2} \pi/a$ is the distance Γ -M in the reciprocal space. The successful overlap of the acoustic branch at low q in all the three phononic crystals results from the different experimental values of c_{eff} decreasing from (2400 ± 50) m/s in the glycerol to (1670 ± 20) m/s in the PDMS-infiltrated opals. This trend is expected since the disparity between the PS sound velocity and the fluid sound velocity increases from glycerol to PDMS (**Fig. 8.5a**). For the wet opals with distinct elastic contrast between the constituent media, c_{eff} can be captured by the effective medium theory [140] of elastic composites consisting of a fluid host with solid (PS) inclusions. With no adjustable parameter, using the experimental densities and the sound velocities of the constituent media, the computed c_{eff} is about 8% lower than the experimental values. This moderate deviation might relate to the neglect of sound dissipation and possible contacts of the solid inclusions at this high packing density in the theory.

The tuning of the bandgap can be further achieved by changing the periodicity of the phononic crystal while maintaining the elastic parameters of the component materials.

Benefiting from the well-controlled self-assembly of fcc colloidal crystals, this can be easily accomplished by varying the size of the monodisperse PS nanospheres. The measured dispersion relations for longitudinal phonons traveling in two phononic colloidal crystals of two different PS particle diameters along the same crystallographic direction Γ -M are displayed in **Fig. 8.6**. Obviously, the central frequency of the gap f_c as well

as its width Δf can be tuned with the particle diameter. Long wavelength (low q) longitudinal

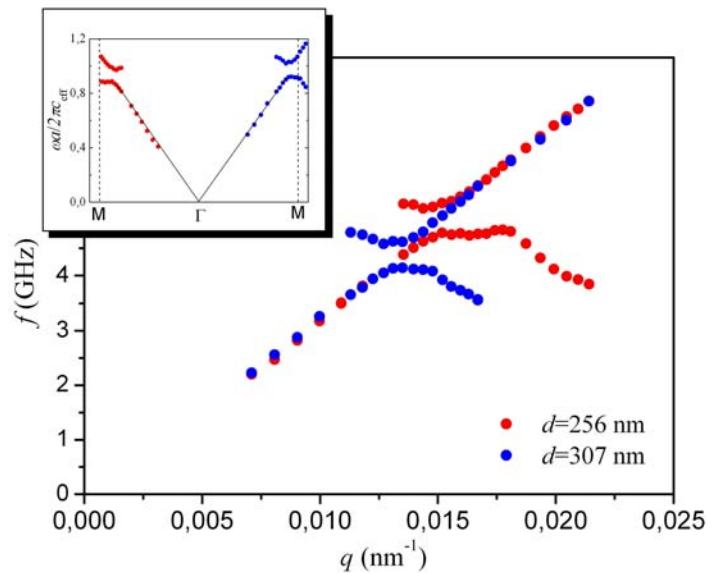


Figure 8.6 Tuning the phononic gap with particle diameter. The dispersion relation, f vs q , for two PS/silicon oil phononic crystals with 256 nm and 307 nm PS particle diameters. Inset: The band structure diagram for the systems of the main plot.

phonons see the same effective medium and thus expectedly propagate with the same phase velocity, $c_{\text{eff}}=(1950\pm 40)$ m/s, in both systems. This value is used to map the experimental dispersion relation of **Fig. 8.6** on the band structure diagram of an fcc phononic crystal. With no adjustable parameter, indeed, both systems exhibit the same bandgap along the same Γ -M direction, suggesting that the frequency f_c and the width of the Bragg gap Δf are inversely proportional to the lattice parameter. Therefore, these phononic crystals forbid wave propagation with wavelengths commensurate to their lattice periodicity. This result is a direct consequence of the invariance of the wave equation of elasticity under the simultaneous transformation of space coordinates and frequency: $\mathbf{r}\rightarrow s\mathbf{r}$ and $f\rightarrow f/s$, where s is an arbitrary scale parameter, for any inhomogeneous system characterized by frequency-independent elastic coefficients.

8.3.3 Hybridization gap effect

In the above, the observed phononic bandgap has been identified as Bragg gap. This is straightforward with the awareness that the gap appears at the BZ boundary and the acoustic-like branch continues its linear q -dependent frequency growth after the gap, as shown in **Fig. 8.6**. Bragg gap formation is a direct consequence of the periodicity of the structure which leads to destructive interference of Bragg diffracted waves, and therefore gaps open up at the BZ boundary. In the current colloidal systems with many spherical inclusions, strong particle resonances, or strong Mie scattering, could happen if the contrast of the acoustic impedance between the sphere and the surrounding medium is large. In this case, the elastic energy is highly localized within these spheres and relatively narrow bands can be formed. When the continuum acoustic bands corresponding to wave propagation in an effective medium meet these narrow bands due to particle resonances, the so-called hybridization gaps [141] may open up.

Usually in phononic crystals with strong resonant units, e.g. spheres and cylinders, the Bragg effect and the hybridization effect coexist, and the final appearance of the band structure is determined by the joint effect of these two contributions [62,138,141-143]. For phononic systems with relatively small elastic contrast, only weak Mie scattering takes place. In this case, the Bragg effect dominates, which usually gives small Bragg gaps at the BZ boundary. The observed gap in the silicon oil infiltrated wet opal is a good example of such

a situation. When the Mie scattering is strong, the hybridization effect often overwhelmingly dominates the gap formation. Indeed, it has been realized that strong Mie scattering is important for the formation of complete phononic bandgap, especially for 3D solid phononic crystals [141] in which both longitudinal and transverse propagating waves are allowed.

Because of the relatively large elastic contrast between PS and PDMS (2350 m/s versus 1050 m/s), stronger Mie scattering is expected to exist in the PDMS infiltrated PS colloidal crystal. Therefore gap formation under the influence of the hybridization effect is likely to happen. In fact, in the dispersion curve for the PDMS infiltrated wet opal (purple triangles) in **Fig. 8.5c**, one could notice some special features different from the silicon oil infiltrated crystal. Specifically, before reaching the BZ boundary (at about 1.0 in the reduced horizontal scale in **Fig. 8.5c**) the propagating longitudinal wave in the effective medium shows some notable deviation from a well-behaved acoustic mode as in the case of the silicon oil infiltrated opal. This is manifested in the sudden jump in the mode frequency at about 0.7 in the reduced horizontal scale, and this discontinuity exceeds the possible experimental reading error related to the broad peak width. In addition, it seems that the same discontinuity happens to the “acoustic-like” branch above the gap.

In the following, it will be shown that despite the observation of a Bragg gap, some important information is still missing in the dispersion curve for the PDMS infiltrated opal in **Fig. 8.5c**. This is mainly caused by the broad width of the peak and the strong Rayleigh wing, which limit the obtainable resolution of some fine spectral features. To achieve better resolution, particles with slightly larger size were used with $d=307$ nm instead of 256 nm. With the use of the same FSR, this could result in narrower peak width due to the red shift of the peak frequencies at the same q . However one should be aware that for even larger particles the resolution will diminish again due to the strong decrease of the phonon frequency. **Figure 8.7** displays representative BLS spectra (normalized to the strongest peak) measured at seven different q values along the Γ -M direction for the PS opal infiltrated by PDMS with particle size $d=307$ nm. The black lines on the right (positive frequency) side are the measured spectra and the red lines on the left side (negative frequency) are the fitting curves synthesized from the individual Lorentzian lines (as indicated on the right side) representing different phonons and a central Lorentzian line accounting for the Rayleigh wing contribution to the spectrum. Clearly, more than two peaks are well-resolved in a large q range, in sharp contrast to the two resolved peaks in the silicon oil infiltrated opal as

shown in **Fig. 8.3d**. At low q , there is only one single phonon detected, in accordance with wave propagation in an effective medium at the long wavelength limit. As q increases, additional modes emerge and the relative intensity of the different modes exhibits rather dramatic changes with the change of q . Generally speaking, these relative intensities reflect the displacement strength of the different phonons, which is connected to the light scattering intensity via the relation $I \sim (\nabla \cdot \mathbf{u})^2$ [63].

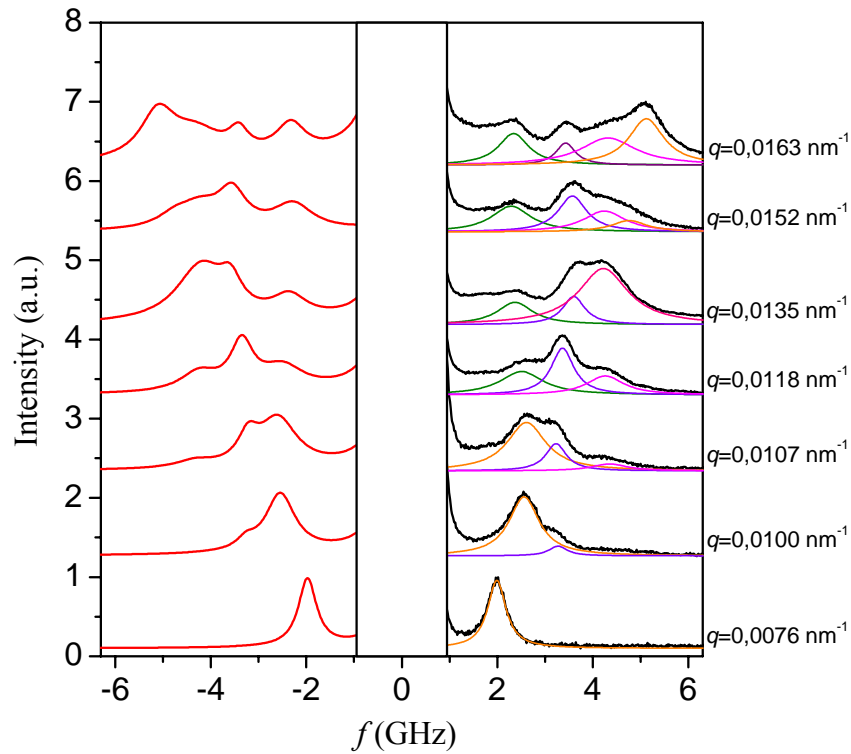


Figure 8.7 BLS spectra for phonon propagation along Γ -M in the PDMS infiltrated PS colloidal crystal. The particle size is $d=307$ nm. The black lines on the positive frequency side represent the experimental spectra recorded at different q values which are normalized to the strongest peak. The red lines on the negative frequency side are the sum of the individual Lorentzian lines shown on the positive frequency side and a central Lorentzian shape responsible for the Rayleigh wing. The Lorentzian peaks in orange on the right side represent the acoustic-like mode, and other Lorentzian lines in the same color fall into the same continuous band in the dispersion curve in Fig. 8.8.

The dispersion relation of the observed phonons is plotted in **Fig. 8.8**, which shows novel features not present in the previous dispersion curve, e.g. in **Fig. 8.6**. The dashed arrows indicate the q positions where the spectra in **Fig. 8.7** were taken for better appreciation of the relation between the spectra and dispersion curve. At low q , very good acoustic behavior is observed, which yields the same effective medium sound velocity

(1670 ± 20 m/s) as obtained before. However, this acoustic branch stops its linear frequency increase at $q \approx 0.010 \text{ nm}^{-1}$, much earlier than the BZ boundary. Accompanying this acoustic stoppage is the appearance of a frequency gap (yellow region) centered at about 2.75 GHz with a width about 0.5 GHz. With further increase of q , the phonon branch below this frequency gap tends to a flat mode, while the branch right above the gap shows a bending frequency increase trend until it reaches the BZ boundary and then starts to fold down, a typical zone folding effect. It is remarkable that there is a second frequency gap (blue region) centered at around 3.95 GHz with a width about 0.7 GHz. By referring to the dispersion curve for the PDMS infiltrated system in **Fig. 8.5c**, it becomes clear that this second gap corresponds to the Bragg gap observed there and the existence of the lower gap explains the non-well-resolved frequency discontinuity in **Fig. 8.5c** mentioned earlier. Note that the acoustic-like mode reappears after the frequency gaps.

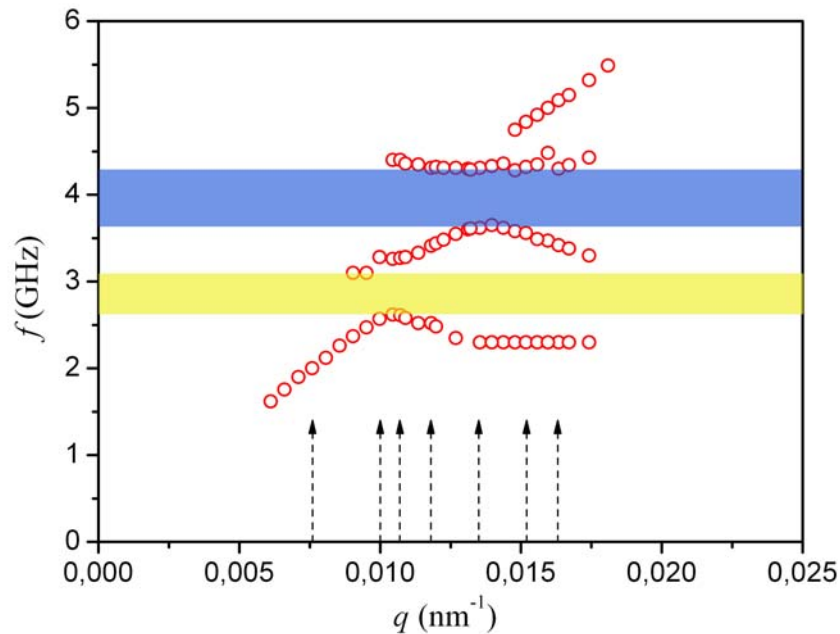


Figure 8.8 Dispersion relation for phonon propagation along Γ -M in the PDMS infiltrated PS colloidal crystal. The yellow region indicates the hybridization gap and the blue region indicates the Bragg gap. The dashed arrows mark those q values at which the spectra in Fig. 8.7 were taken. The PS particle size is $d=307$ nm.

The lower gap formation (yellow region) must be due to the hybridization effect between the continuum acoustic band and the particle resonances since it cannot be described by the zone folding effect caused by the periodic structure responsible for a Bragg gap. The existence of particle resonance (largely localized) is further indicated by the

appearance of the flat mode at around 2.3 GHz. Due to the weak intensity and limited spectral resolution, some possible fine structures at the very low frequencies are not well-resolved in **Fig. 8.7**. However this does not affect the prominent feature of the dispersion relation. As for the upper Bragg gap, the band right above it is also rather flat, suggesting this gap formation includes very likely the contribution from higher order particle resonance mode.

To further check the generality of the observation of the hybridization gap effect, this investigation was extended to the PDMS infiltrated PMMA fcc colloidal crystals. Similar behavior was observed as shown by the blue open circles in **Fig. 8.9a**, which depict the phonon propagation along Γ -M. The previously encountered two gaps, the Bragg gap and hybridization gap, are clearly present. The small increase in the elastic contrast between

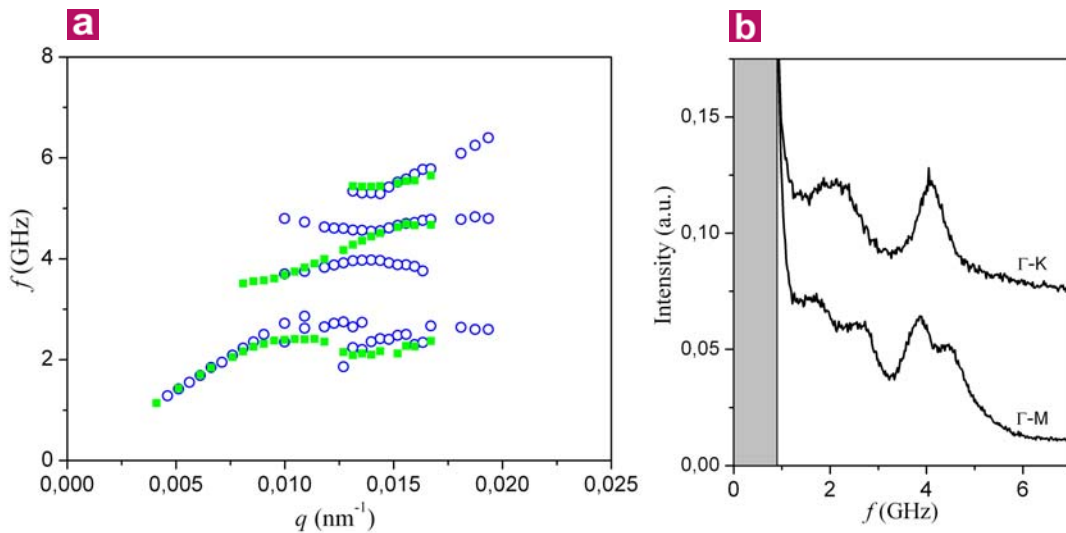


Figure 8.9 Phonon propagation in PDMS infiltrated PMMA colloidal crystal. a, Dispersion relations corresponding to phonon propagation along two different directions: Γ -M (blue open dots) and Γ -K (green solid squares). It is remarkable that the Bragg gap observed along Γ -M is not present for phonon propagation in the Γ -K direction, while the hybridization gaps exist in both cases. The PMMA particle size is $d=327$ nm. **b,** Two spectra taken at $q=0.0127$ nm^{-1} are selected to show the spectral changes corresponding to the changes in the dispersion relation in panel (a).

PMMA ($c_l=2800$ m/s and $c_t=1400$ m/s) and PDMS leads to a slightly higher effective medium sound velocity which is (1720 ± 20) m/s. Note that another narrow gap seems to appear above the Bragg gap, which is less obvious in the PS colloidal crystal in **Fig. 8.8**. This should be related to the particle resonances close to that frequency region. This effect, being stronger in the PMMA colloidal system, may be due to the slightly increased elastic

mismatch between the particles and the surrounding medium. It has been pointed out [141,142] that the hybridization gap should be insensitive to the lattice structure as its formation strongly depends on the localized resonances which are not much affected by the long range order of the scatterers. Indeed, by mapping the phonon propagation along the Γ -K (see **Fig. 8.2**) direction which is further away from the BZ face center, the central gap around 4.2 GHz observed along Γ -M vanishes, as indicated by the corresponding dispersion relation (the green solid squares) in **Fig. 8.9a**. This observation agrees with its Bragg gap origin. It is not fully clear why the Bragg gap disappears along Γ -K [70]. Two BLS spectra taken at the same $q=0.0127 \text{ nm}^{-1}$ are shown in **Fig. 8.9b** to demonstrate the disappearing of the Bragg gap when the phonon propagation varies from Γ -M to Γ -K. On the contrary, the hybridization gaps are much less influenced by the phonon propagation direction. The excellent overlap of the two acoustic branches for the two different propagation directions at the low q limit is a solid illustration of the validity of the effective medium approach to describe the wave propagation in inhomogeneous systems at the long wavelength limit.

8.3.4 Some remarks

Structural defects, like point defects (e.g. vacancies), line defects (e.g. dislocations), stacking faults, and cracks, are usually present in colloidal crystals formed by vertical deposition [144,145] and can be well identified in SEM images. In the present crystals the approximate diameter of compact domains between cracks are in the order of 10-50 μm , an approximate point defect areal density is about $0.005 \mu\text{m}^{-2}$ at the crystal surface, while line defects and stacking faults are found about every 5-10 μm . The overall fcc crystal structure with very high orientational domain order throughout the whole crystal is commonly observed in these vertically deposited colloid crystals and was clearly identified in SEM images of fractured samples, which also reveal the high crystal quality within the whole layer [146]. Besides the visual inspection by SEM or optical microscopy, the defect characterization in such samples remains an experimental challenge. A detailed analysis of the optical diffraction patterns of the dry opals could in principle be used to investigate the defects like stacking faults [147].

Theoretically, the various structural defects can introduce states within a bandgap and thus the gap may be reduced or even totally suppressed. Experimentally, possible influence

of the presence of defects should be reflected in the detailed features of the observed peaks (e.g. shape, intensity, width, frequency and so on). In the present case, BLS spectra taken at different sample areas do not show any essential difference, which indicates that the prominent phononic properties of the crystals under investigation are free from the influence of the presence of minor defects, in accordance with the high crystal quality revealed by SEM. A systematic experimental study of the influence of the defects on the phononic properties requests that the defects in the crystal must be introduced in a controllable way. This still remains a challenge for the vertical lifting deposition.

Although the dispersion relation carries the most important information of the phononic crystal, obviously other spectral features, e.g. the peak width and the relative intensity, could also provide additional valuable details about the wave propagation. Unfortunately, at the current stage, it is very difficult to well analyse and understand these detailed features. Experimentally, the apparent width is more influenced by the unavoidable strong Rayleigh wing. More importantly, despite the general drastic increase in the width with q in the vicinity of the gap, a well-defined behaviour is not found. On the theoretical side, no theory has been well-developed to address the wavenumber dependent phonon damping in a strong multiple scattering inhomogeneous medium including also viscous loss, needless to say the complication by the structure relaxation at hypersonic regime. In addition, the viscosity contribution is almost exclusively ignored in the state-of-the-art band structure calculation for a phononic crystal [148]. However, it is highly desirable to capture the experimentally observed dispersion relation theoretically, especially regarding the unusual hybridization gap formation. It is still a challenge to completely capture the experimental dispersion curve using popular computation techniques, probably due to the neglect of viscous loss and the touch of colloidal particles which in principle could affect the band structure.

Chapter 9

Epilogue

9.1 Conclusions

In this dissertation, Brillouin light scattering (BLS) has been applied to investigate hypersonic elastic excitations in polymer thin films and colloidal crystals. The aim was to explore elastic wave propagation in inhomogeneous systems and investigate the relation of their structural characteristics and micromechanical properties. Complex elastic wave propagation and localization have been revealed in these soft mesoscopic structures including the first experimental discovery of propagation gaps at GHz frequencies. The designed approach was to first study thin amorphous polymer films and then 1D periodic polymeric multilayer films to assess possible interfacial effects. Afterwards, the focus was on colloid crystalline structures containing strong resonance units to examine the modulation of elastic waves by structure and/or local resonances.

For supported thin polymer films on a transparent (glass) substrate, various quasi-guided Lamb modes, or waves of mixed longitudinal-transverse character polarized in the sagittal plane, were detected using BLS in an appropriate transmission scattering geometry. For both PS and PMMA thin films, no appreciable change in the elastic properties compared to the bulk material was found with thickness down to 40 nm. The detection of Lamb modes using transparent substrates extends the applicability of BLS to study elastic excitations and interfacial properties in thin films. The temperature dependence of the Lamb modes allows the determination of the glass transition temperature of supported thin films by BLS. A reduction in the T_g for both PS and PMMA ultra-thin supported films was found, despite the

difference in their chemical nature as well as the interactions with silicon oxide surface. No direct correlation has been established between the elastic parameters and the T_g reductions.

Next, the study was on the in-plane elastic excitations in a 1D periodic polymeric film comprised of more than 200 alternating PMMA ($h=78$ nm) and PET ($h=118$ nm) thin layers. Five acoustic-like modes with constant phase velocities plus an additional high frequency optic-like mode were observed. Finite element analysis was used to compute the theoretical phonon dispersion relation and provide interpretation of the observed modes. Complex features of the phonon dispersion relation were attributed to elastic waves propagating within the individual polymer layers. This association was further supported by measuring the temperature dependence of sound velocities of these modes, which exhibited glass transitions at two distinctly different temperatures corresponding to the individual components. Moreover, BLS was shown to be capable of revealing the mechanical anisotropy of this multilayer film accompanied with its optical birefringence.

Further, in fcc dry colloidal crystals consisting of close-packed PS spherical submicrometer particles, a large number of localized particle resonances were observed. These modes were unambiguously identified as the vibration eigenmodes of the individual PS spheres by “single-phonon scattering-cross-section” calculations. The frequencies of these eigenmodes were found to depend on the particle diameter. The peculiar line shape of the low-frequency modes was found to be a sensitive index of the particle size distribution. A novel low-frequency continuum was also observed, whose origin remains unclear, possibly due to the eigenvibrations of small particle aggregates. By using amorphous CaCO_3 , the BLS detection of particle vibration eigenmodes was illustrated to be of great practical importance in extracting unknown elastic parameters and even the size distribution of nanoobject aggregates.

Finally, optically transparent fcc wet colloidal crystals were prepared by infiltrating the dry precursors with appropriate fluids. The application of BLS to such systems led to the first experimental observation of a hypersonic Bragg gap. Depending on the particle size and the sound velocity in the infiltration fluid, the frequency and the width of the gap were tuned. Larger gap width appeared with the increase of elastic mismatch between the solid inclusions and the fluid matrix, at the same time the phonon lifetime was reduced due to

stronger phonon scattering. For sufficiently high elastic contrast, such as PS particles in a PDMS matrix, besides the Bragg gap, additional gap formation due to the hybridization of acoustic mode and particle resonance occurred, which further complicates the phonon propagation in colloidal systems. Unlike the Bragg gap, the hybridization gap was found to be insensitive to the change of the propagation direction of the phonon, in conformity to its special origin. The successful probing of phononic properties of single crystalline colloidal crystals manifests that the combination of BLS and phononic structures constitutes an effective methodology in search of the design of optimal phononic crystals operating in the hypersonic regime.

9.2 Outlook

The results of this PhD work generated new questions and suggest future efforts in: (i) the glass transition and micromechanics of thin films, sandwiched polymer layers, and (ii) in the emerging area of phononics.

(i) To investigate the confinement effect on the change of elastic properties and glass transition of thin polymer films, one choice is to introduce stronger modification of the substrate-polymer interactions, e.g. by covalent modification of the substrate surface with molecules or polymer brushes. In the case of elastic wave propagation in multilayer polymer films, variation of the absolute and relative thickness of the individual layers would certainly advance the understanding of this phenomenon. In addition, the choice of a nearly optically isotropic multilayer assembly system would allow the distinction of the scattered light with orthogonal polarizations, facilitating the identification of the nature of the various modes. In fact, this sample requirement can be fulfilled by PC/PMMA (PC stands for polycarbonate) multilayer stacks.

(ii) In the investigation of hypersonic phononic crystals, many more possibilities and challenges lay ahead. Concerning the building blocks, instead of using simple spheres, core-shell particles are worth investigating for their capacity of modulating local resonances in a nontrivial manner. Attempts should also be directed towards altering the volume fraction of the fcc crystals as well as trying other available crystal types. Further increase of the elastic contrast of the constituents, such as using silica in place of polymeric particles, is anticipated to lead to further insights into the gap formation phenomenon, especially for the

hybridization-induced gap. Such experiments will challenge band structure calculations for different particle architectures and volume fractions. Attention should be also paid to developing other experimental techniques to overcome opacity, and realizing the potential applications, such as novel acousto-optical devices and thermal management, which utilize this unusual phononic effect.

Bibliography

- [1] Murray, C. B., Kagan, C. R. & Bawendi, M. G. Synthesis and characterization of monodisperse nanocrystals and close-packed nanocrystal assemblies. *Annu. Rev. Mater. Sci.* **30**, 545 (2000).
- [2] Campbell, M., Sharp, D. N., Harrison, M. T., Denning, R. G. & Turberfield, A. J. Fabrication of photonic crystals for the visible spectrum by holographic lithography. *Nature* **404**, 53 (2000).
- [3] Dendukuri, D., Pregibon, D. C., Collins, J., Hatton, T. A. & Doyle, P. S. Continuous-flow lithography for high-throughput microparticle synthesis. *Nature Mater.* **5**, 365 (2006).
- [4] Discher, D. E. & Kamien, R. D. Self-assembly - towards precision micelles. *Nature* **430**, 519 (2004).
- [5] Herminghaus, S. Soft lithography: harnessing the unstable. *Nature Mater.* **2**, 11 (2003).
- [6] Ikkala, O. & ten Brinke, G. Functional materials based on self-assembly of polymeric supramolecules. *Science* **295**, 2407 (2002).
- [7] Ito, T. & Okazaki, S. Pushing the limits of lithography. *Nature* **406**, 1027 (2000).
- [8] Whitesides, G. M. & Grzybowski, B. Self-assembly at all scales. *Science* **295**, 2418 (2002).
- [9] Roth, C. B. & Dutcher, J. R. Mobility on different length scales in thin polymer films, in *Soft materials (structure and dynamics)*, (eds. Dutcher, J. R. and Marangoni, A. G.) Marcel Dekker, New York, 2005.
- [10] Keddie, J. L., Jones, R. A. L. & Cory, R. A. Size-dependent depression of the glass-transition temperature in polymer-films. *Europhys. Lett.* **27**, 59 (1994).
- [11] Forrest, J. A., Dalnoki-Veress, K. & Dutcher, J. R. Interface and chain confinement effects on the glass transition temperature of thin polymer films. *Phys. Rev. E* **56**, 5705 (1997).
- [12] Kawana, S. & Jones, R. A. L. Character of the glass transition in thin supported polymer films. *Phys. Rev. E* **63**, 021501 (2001).
- [13] Tsui, O. K. C. & Zhang, H. F. Effects of chain ends and chain entanglement on the glass transition temperature of polymer thin films. *Macromolecules* **34**, 9139 (2001).
- [14] Fukao, K. & Miyamoto, Y. Glass transition temperature and dynamics of alpha-process in thin polymer films. *Europhys. Lett.* **46**, 649 (1999).
- [15] Fukao, K. & Miyamoto, Y. Glass transitions and dynamics in thin polymer films: dielectric relaxation of thin films of polystyrene. *Phys. Rev. E* **61**, 1743 (2000).
- [16] Tsui, O. K. C., Russell, T. P. & Hawker, C. J. Effect of interfacial interactions on the glass transition of polymer thin films. *Macromolecules* **34**, 5535 (2001).
- [17] DeMaggio, G. B., Frieze, W. E., Gidley, D. W., Zhu, M., Hristov, H. A. & Yee, A. F. Interface and surface effects on the glass transition in thin polystyrene films. *Phys. Rev. Lett.* **78**, 1524 (1997).
- [18] Forrest, J. A., Dalnoki-Veress, K., Stevens, J. R. & Dutcher, J. R. Effect of free surfaces on the glass transition temperature of thin polymer films. *Phys. Rev. Lett.* **77**, 2002 (1996).
- [19] Fryer, D. S., Nealey, P. F. & de Pablo, J. J. Thermal probe measurements of the glass transition temperature for ultrathin polymer films as a function of thickness. *Macromolecules* **33**, 6439 (2000).

- [20] Forrest, J. A. & Dalnoki-Veress, K. The glass transition in thin polymer films. *Adv. in Colloid and Interface Sci.* **94**, 167 (2001).
- [21] Reiter, G. & Forrest, J. Special issue on properties of thin polymer films. *Eur. Phys. J. E* **8**, 101 (2002).
- [22] Yamamoto, S., Tsujii, Y. & Fukuda, T. Glass transition temperatures of high-density poly(methyl methacrylate) brushes. *Macromolecules* **35**, 6077 (2002).
- [23] Jansen, K. M. B., Gonda, V. & Ernst, L. J. State-of-the-art of thermal mechanical characterization of thin polymer films. *J. Electron. Packag.* **127**, 530 (2006).
- [24] Sun, L., Dutcher, J. R., Giovannini, L., Nizzoli, F., Stevens, J. R. & Ord, J. L. Elastic and elasto-optic properties of thin-films of poly(styrene) spin-coated onto Si(001). *J. Appl. Phys.* **75**, 7482 (1994).
- [25] Hartschuh, R. D., Kisliuk, A., Novikov, V., Sokolov, A. P., Heyliger, P. R., Flannery, C. M., Johnson, W. L., Soles, C. L. & Wu, W. L. Acoustic modes and elastic properties of polymeric nanostructures. *App. Phys. Lett.* **87**, 173132 (2005).
- [26] Forrest, J. A., Rowat, A. C., DalnokiVeress, K., Stevens, J. R. & Dutcher, J. R. Brillouin light scattering studies of the mechanical properties of polystyrene/polyisoprene multilayered thin films. *J. Polym. Sci. Part B: Polym. Phys.* **34**, 3009 (1996).
- [27] Joannopoulos, J. D., Villeneuve, P. R. & Fan, S. H. Photonic crystals: putting a new twist on light. *Nature* **386**, 143 (1997).
- [28] Meade, R. D., Brommer, K. D., Rappe, A. M. & Joannopoulos, J. D. Photonic bound-states in periodic dielectric materials. *Phys. Rev. B* **44**, 13772 (1991).
- [29] Meade, R. D., Brommer, K. D., Rappe, A. M. & Joannopoulos, J. D. Existence of a photonic band-gap in 2 dimensions. *App. Phys. Lett.* **61**, 495 (1992).
- [30] Meade, R. D., Rappe, A. M., Brommer, K. D., Joannopoulos, J. D. & Alerhand, O. L. Accurate theoretical-analysis of photonic band-gap materials. *Phys. Rev. B* **48**, 8434 (1993).
- [31] Robertson, W. M., Arjavalingam, G., Meade, R. D., Brommer, K. D., Rappe, A. M. & Joannopoulos, J. D. Measurement of photonic band-structure in a two-dimensional periodic dielectric array. *Phys. Rev. Lett.* **68**, 2023 (1992).
- [32] Yablonovitch, E., Gmitter, T. J., Meade, R. D., Rappe, A. M., Brommer, K. D. & Joannopoulos, J. D. Donor and acceptor modes in photonic band-structure. *Phys. Rev. Lett.* **67**, 3380 (1991).
- [33] Yablonovitch, E. Inhibited spontaneous emission in solid-state physics and electronics. *Phys. Rev. Lett.* **58**, 2059 (1987).
- [34] Yablonovitch, E. & Gmitter, T. J. Photonic band-structure - the face-centered-cubic case. *Phys. Rev. Lett.* **63**, 1950 (1989).
- [35] Yablonovitch, E., Gmitter, T. J. & Leung, K. M. Photonic band-structure : the face-centered-cubic case employing nonspherical atoms. *Phys. Rev. Lett.* **67**, 2295 (1991).
- [36] Kushwaha, M. S., Halevi, P., Dobrzynski, L. & Djafarirouhani, B. Acoustic band-structure of periodic elastic composites. *Phys. Rev. Lett.* **71**, 2022 (1993).
- [37] Gorishnyy, T., Maldovan, M., Ullal, C. & Thomas, E. Sound ideas. *Phys. World* **18**, 24 (2005).
- [38] Gorishnyy, T., Ullal, C. K., Maldovan, M., Fytas, G. & Thomas, E. L. Hypersonic phononic crystals. *Phys. Rev. Lett.* **94**, 115501 (2005).

- [39] Kent, A. J., Kini, R. N., Stanton, N. M., Henini, M., Glavin, B. A., Kochelap, V. A. & Linnik, T. L. Acoustic phonon emission from a weakly coupled superlattice under vertical electron transport: observation of phonon resonance. *Phys. Rev. Lett.* **96**, 215504 (2006).
- [40] Liu, Z. Y., Zhang, X. X., Mao, Y. W., Zhu, Y. Y., Yang, Z. Y., Chan, C. T. & Sheng, P. Locally resonant sonic materials. *Science* **289**, 1734 (2000).
- [41] Maldovan, M. & Thomas, E. L. Simultaneous localization of photons and phonons in two-dimensional periodic structures. *App. Phys. Lett.* **88**, 251907 (2006).
- [42] Martinez-sala, R., Sancho, J., Sanchez, J. V., Gomez, V., Llinares, J. & Meseguer, F. Sound attenuation by sculpture. *Nature* **378**, 241 (1995).
- [43] Montero de Espinosa, F. R. M., Jimenez, E. & Torres, M. Ultrasonic band gap in a periodic two-dimensional composite. *Phys. Rev. Lett.* **80**, 1208 (1998).
- [44] Vasseur, J. O., Deymier, P. A., Chenni, B., Djafari-Rouhani, B., Dobrzynski, L. & Prevost, D. Experimental and theoretical evidence for the existence of absolute acoustic band gaps in two-dimensional solid phononic crystals. *Phys. Rev. Lett.* **86**, 3012 (2001).
- [45] Modinos, A., Stefanou, N., Psarobas, I. E. & Yannopoulos, V. On wave propagation in inhomogeneous systems. *Physica B* **296**, 167 (2001).
- [46] Sigalas, M. & Economou, E. N. Band-structure of elastic-waves in 2-dimensional systems. *Solid State Communications* **86**, 141 (1993).
- [47] Yang, S. X., Page, J. H., Liu, Z. Y., Cowan, M. L., Chan, C. T. & Sheng, P. Ultrasound tunneling through 3D phononic crystals. *Phys. Rev. Lett.* **88**, 104301 (2002).
- [48] Yang, S. X., Page, J. H., Liu, Z. Y., Cowan, M. L., Chan, C. T. & Sheng, P. Focusing of sound in a 3D phononic crystal. *Phys. Rev. Lett.* **93**, 024301 (2004).
- [49] Zhang, X. D. & Liu, Z. Y. Negative refraction of acoustic waves in two-dimensional phononic crystals. *App. Phys. Lett.* **85**, 341 (2004).
- [50] Landau, L. D. & Lifshitz, E. M. *Theory of elasticity*, 3 ed. (Reed Educational and Professional, Oxford, 1986).
- [51] Nye, J. F. *Physical properties of crystals*. (Oxford University Press, Oxford, 1960).
- [52] Kafesaki, M. & Economou, E. N. Multiple-scattering theory for three-dimensional periodic acoustic composites. *Phys. Rev. B* **60**, 11993 (1999).
- [53] Liu, Z. Y., Chan, C. T., Sheng, P., Goertzen, A. L. & Page, J. H. Elastic wave scattering by periodic structures of spherical objects: theory and experiment. *Phys. Rev. B* **62**, 2446 (2000).
- [54] Psarobas, I. E., Stefanou, N. & Modinos, A. Scattering of elastic waves by periodic arrays of spherical bodies. *Phys. Rev. B* **62**, 278 (2000).
- [55] Straton, J. A. *Electromagnetic theory*. (McGraw-Hill, New York, 1941).
- [56] Temme, N. M. *Special functions: an introduction to the classical functions of mathematical physics*. (John Wiley & Sons, New York, 1996).
- [57] Farnell, G. W. & Adler, E. L. Elastic wave propagation in thin layers, in *Physical acoustics, principles and methods*, (eds. Mason, W. P. and Thurston, R. N.) Academic Press, New York, 1972.
- [58] Loudon, R. Theory of surface-ripple Brillouin-scattering by solids. *Phys. Rev. Lett.* **40**, 581 (1978).

- [59] Glass, N. E. & Maradudin, A. A. Leaky surface-elastic waves on both flat and strongly corrugated surfaces for isotropic, nondissipative media. *J. Appl. Phys.* **54**, 796 (1983).
- [60] Hillebrands, B., Lee, S., Stegeman, G. I., Cheng, H., Potts, J. E. & Nizzoli, F. Evidence for the existence of guided longitudinal acoustic phonons in ZnSe films on GaAs. *Phys. Rev. Lett.* **60**, 832 (1988).
- [61] Lamb, H. On the vibrations of an elastic sphere. *Proc. Math. Soc. London* **13**, 189 (1882).
- [62] Kafesaki, M. & Economou, E. N. Interpretation of the band-structure results for elastic and acoustic-waves by analogy with the LCAO approach. *Phys. Rev. B* **52**, 13317 (1995).
- [63] Penciu, R. S. Acoustic and elastic waves in periodic and random media. PhD thesis, University of Crete, 2002.
- [64] John, S. & Rangarajan, R. Optimal structures for classical wave localization - an alternative to the Ioffe-Regel criterion. *Phys. Rev. B* **38**, 10101 (1988).
- [65] Economou, E. N. & Zdetsis, A. Classical wave-propagation in periodic structures. *Phys. Rev. B* **40**, 1334 (1989).
- [66] Sainidou, R., Stefanou, N. & Modinos, A. Widening of phononic transmission gaps via Anderson localization. *Phys. Rev. Lett.* **94**, 205503 (2005).
- [67] Economou, E. N. & Sigalas, M. Stop bands for elastic-waves in periodic composite-materials. *J. Acoust. Soc. Am.* **95**, 1734 (1994).
- [68] Kushwaha, M. S., Halevi, P., Martinez, G., Dobrzynski, L. & Djafarirouhani, B. Theory of acoustic band-structure of periodic elastic composites. *Phys. Rev. B* **49**, 2313 (1994).
- [69] Sigalas, M. M. & Garcia, N. Theoretical study of three dimensional elastic band gaps with the finite-difference time-domain method. *J. Appl. Phys.* **87**, 3122 (2000).
- [70] Ashcroft, N. W. & Mermin, D. N. *Solid state physics*. (Holt, Rinehart and Winston, Philadelphia, 1976).
- [71] Edmonds, A. R. *Angular momentum in quantum mechanics*. (Princeton University Press, Princeton, 1974).
- [72] Sainidou, R., Stefanou, N., Psarobas, I. E. & Modinos, A. A layer-multiple-scattering method for phononic crystals and hetero structures of such. *Computer Phys. Commun.* **166**, 197 (2005).
- [73] Long, D. A. *The Raman effect: a unified treatment of the theory of Raman scattering by molecules*. (John Wiley & Sons, Chichester, 2002).
- [74] Berne, B. & Pecora, R. *Dynamic light scattering with applications to chemistry, biology and physics*. (Dover Publications, New York, 1976).
- [75] Chu, B. *Laser light scattering: basic principles and practice*, 2 ed. (Academic Press, San Diego, 1991).
- [76] Brillouin, L. *Ann. de Physique (Paris)* **17**, 88 (1922).
- [77] Fabelinskii, I. L. *Molecular scattering of light*. (Plenum Press, New York, 1968).
- [78] Strutt, J. W. & Rayleigh, B. *The theory of sound*, 3 ed. (Macmillan, London, 1896).
- [79] Wood, A. B. *A textbook of sound*, 3 ed. (Bell & Sons, London, 1964).

- [80] Landau, L. & Placzek, G. *Phys. Z. Sowjetunion* **5**, 172 (1934).
- [81] Patterson, G. D. Light scattering from bulk polymers. *Ann. Rev. Mater. Sci.* **13**, 219 (1983).
- [82] Loudon, R. Theory of lineshapes for oblique-Incidence Brillouin-scattering by acoustic phonons. *J. Phys. C:Solid State Phys.* **11**, 2623 (1978).
- [83] Sandercock, J. R. Structure in Brillouin spectra of thin films. *Phys. Rev. Lett.* **29**, 1735 (1972).
- [84] Hecht, E. *Optics*. (Addison-Wesley Longman, Amsterdam, 2002).
- [85] Sandercock, J. R., presented at the Proc. 2nd Int. Conf. on light scattering in solids, Paris, 1971 (unpublished).
- [86] Mock, R., Hillebrands, B. & Sandercock, R. Construction and performance of a Brillouin scattering set-up using a triple-pass tandem Fabry-Perot interferometer. *J. Phys. E: Sci. Instrum.* **20**, 656 (1987).
- [87] Sainidou, R., Stefanou, N. & Modinos, A. Green's function formalism for phononic crystals. *Phys. Rev. B* **69** (2004).
- [88] Sainidou, R., Djafari-Rouhani, B., Pennec, Y. & Vasseur, J. O. Locally resonant phononic crystals made of hollow spheres or cylinders. *Phys. Rev. B* **73**, 184301 (2006).
- [89] Wittkowski, T., Distler, G., Jung, K., Hillebrands, B. & Comins, J. D. General methods for the determination of the stiffness tensor and mass density of thin films using Brillouin light scattering: study of tungsten carbide films. *Phys. Rev. B* **69**, 205401 (2004).
- [90] Champion, J. V. & Jackson, D. A. Brillouin-scattering from liquid normal-alkanes. *Molec. Phys.* **31**, 1159 (1976).
- [91] Adam, G. & Gibbs, J. H. On temperature dependence of cooperative relaxation properties in glass-forming liquids. *J. Chem. Phys.* **43**, 139 (1965).
- [92] Hempel, E., Hempel, G., Hensel, A., Schick, C. & Donth, E. Characteristic length of dynamic glass transition near T_g for a wide assortment of glass-forming substances. *J. Phys. Chem. B* **104**, 2460 (2000).
- [93] Reinsberg, S. A., Qiu, X. H., Wilhelm, M., Spiess, H. W. & Ediger, M. D. Length scale of dynamic heterogeneity in supercooled glycerol near T_g. *J. Chem. Phys.* **114**, 7299 (2001).
- [94] Forrest, J. A. & Mattsson, J. Reductions of the glass transition temperature in thin polymer films: probing the length scale of cooperative dynamics. *Phys. Rev. E* **61**, R53 (2000).
- [95] Kim, J. H., Jang, J. & Zin, W. C. Estimation of the thickness dependence of the glass transition temperature in various thin polymer films. *Langmuir* **16**, 4064 (2000).
- [96] Torres, J. A., Nealey, P. F. & de Pablo, J. J. Molecular simulation of ultrathin polymeric films near the glass transition. *Phys. Rev. Lett.* **85**, 3221 (2000).
- [97] Keddie, J. L., Jones, R. A. L. & Cory, R. A. Interface and surface effects on the glass-transition temperature in thin polymer-films. *Faraday Discuss.* **98**, 219 (1994).
- [98] Sharp, J. S. & Forrest, J. A. Dielectric and ellipsometric studies of the dynamics in thin films of isotactic poly(methylmethacrylate) with one free surface. *Phys. Rev. E* **67**, 031805 (2003).
- [99] Fryer, D. S., Peters, R. D., Kim, E. J., Tomaszewski, J. E., de Pablo, J. J., Nealey, P. F., White, C. C. & Wu, W. L. Dependence of the glass transition temperature of polymer films on interfacial energy and thickness. *Macromolecules* **34**, 5627 (2001).

- [100] Santen, L. & Krauth, W. Absence of thermodynamic phase transition in a model glass former. *Nature* **405**, 550 (2000).
- [101] Dalnoki-Veress, E., Forrest, J. A., Murray, C., Gigault, C. & Dutcher, J. R. Molecular weight dependence of reductions in the glass transition temperature of thin, freely standing polymer films. *Phys. Rev. E* **63**, 031801 (2001).
- [102] Wunderlich, B. *Thermal analysis*. (Academic Press, New York, 1990).
- [103] Grohens, Y., Hamon, L., Reiter, G., Soldera, A. & Holl, Y. Some relevant parameters affecting the glass transition of supported ultra-thin polymer films. *Eur. Phys. J. E* **8**, 217 (2002).
- [104] Forrest, J. A., Dalnoki-Veress, K. & Dutcher, J. R. Brillouin light scattering studies of the mechanical properties of thin freely standing polystyrene films. *Phys. Rev. E* **58**, 6109 (1998).
- [105] Ellison, C. J., Kim, S. D., Hall, D. B. & Torkelson, J. M. Confinement and processing effects on glass transition temperature and physical aging in ultrathin polymer films: novel fluorescence measurements. *Eur. Phys. J. E* **8**, 155 (2002).
- [106] Ellison, C. J. & Torkelson, J. M. Sensing the glass transition in thin and ultrathin polymer films via fluorescence probes and labels. *J. Polym. Sci. part B: Polym. Phys.* **40**, 2745 (2002).
- [107] Ellison, C. J. & Torkelson, J. M. The distribution of glass-transition temperatures in nanoscopically confined glass formers. *Nature Mater.* **2**, 695 (2003).
- [108] Priestley, R. D., Ellison, C. J., Broadbelt, L. J. & Torkelson, J. M. Structural relaxation of polymer glasses at surfaces, interfaces and in between. *Science* **309**, 456 (2005).
- [109] Weber, M. F., Stover, C. A., Gilbert, L. R., Nevitt, T. J. & Ouderkirk, A. J. Giant birefringent optics in multilayer polymer mirrors. *Science* **287**, 2451 (2000).
- [110] Bandhu, R. S., Zhang, X., Sooryakumar, R. & Busmann, K. Acoustic vibrations in free-standing double layer membranes. *Phys. Rev. B* **70**, 075409 (2004).
- [111] Grimsditch, M., Bhadra, R. & Schuller, I. K. Lamb waves in unsupported thin-films - a Brillouin-scattering study. *Phys. Rev. Lett.* **58**, 1216 (1987).
- [112] Anders, S. H., Eberle, R., Peetz, L., Kruger, J. K., Goschel, U. & Pietralla, M. Anisotropic properties of poly(ethylene terephthalate) by Brillouin spectroscopy: anisotropic properties of oriented bulk and nanostructured poly(ethylene terephthalate) determined by Brillouin spectroscopy and birefringence experiments. *J. polym. sci. part B: polym. phys.* **40**, 1201 (2002).
- [113] Chan, O. K., Chen, F. C., Choy, C. L. & Ward, I. M. Elastic-constants of extruded polypropylene and polyethylene terephthalate. *J. Phys. D: Appl. Phys.* **11**, 617 (1978).
- [114] Feng, R. & Farris, R. J. Linear thermoelastic characterization of anisotropic poly(ethylene terephthalate) films. *J. Appl. Polym. Sci.* **86**, 2937 (2002).
- [115] Cheng, W., Fytas, G., Kiyanova, A. V., Efremov, M. Y. & Nealey, P. F. Submicron polymer gratings: optical diffraction and spontaneous Brillouin scattering. *Macromol. Rapid Commun.* **27**, 702 (2006).
- [116] Liu, J., Ye, L., Weitz, D. A. & Ping, S. Novel acoustic excitations in suspensions of hard-sphere colloids. *Phys. Rev. Lett.* **65**, 2602 (1990).
- [117] Penciu, R. S., Kriegs, H., Petekidis, G., Fytas, G. & Economou, E. N. Phonons in colloidal systems. *J. Chem. Phys.* **118**, 5224 (2003).

- [118] Penciu, R. S., Fytas, G., Economou, E. N., Steffen, W. & Yannopoulos, S. N. Acoustic excitations in suspensions of soft colloids. *Phys. Rev. Lett.* **85**, 4622 (2000).
- [119] Kuok, M. H., Lim, H. S., Ng, S. C., Liu, N. N. & Wang, Z. K. Brillouin study of the quantization of acoustic modes in nanospheres (vol 20, art no 255502, 2003). *Phys. Rev. Lett.* **91**, 149901 (2003).
- [120] Lim, H. S., Kuok, M. H., Ng, S. C. & Wang, Z. K. Brillouin observation of bulk and confined acoustic waves in silica microspheres. *Appl. Phys. Lett.* **84**, 4182 (2004).
- [121] Jonas, U. & Krueger, C. The effect of polar, nonpolar, and electrostatic interactions and wetting behavior on the particle assembly at patterned surfaces. *J. Supramol. Chem.* **2**, 255 (2002).
- [122] Krueger, C. & Jonas, U. Synthesis and pH-sensitive adsorption of latex particles onto photolithographically patterned silane layers. *J. Colloid Interface Sci.* **252**, 331 (2002).
- [123] Auld, B. A. *Acoustic fields and waves in solids*, 2 ed. (Krieger, Malabar, 1990).
- [124] Duval, E. Far-infrared and Raman vibrational transitions of a solid sphere - selection-rules. *Phys. Rev. B* **46**, 5795 (1992).
- [125] Li, Y., Lim, H. S., Ng, S. C., Wang, Z. K., Kuok, M. H., Vekris, E., Kitaev, V., Peiris, F. C. & Ozin, G. A. Micro-Brillouin scattering from a single isolated nanosphere. *App. Phys. Lett.* **88**, 023112 (2006).
- [126] Cheng, Z. D., Zhu, J. X., Russel, W. B. & Chaikin, P. M. Phonons in an entropic crystal. *Phys. Rev. Lett.* **85**, 1460 (2000).
- [127] Phan, S. E., Li, M., Russel, W. B., Zhu, J. X., Chaikin, P. M. & Lant, C. T. Linear viscoelasticity of hard sphere colloidal crystals from resonance detected with dynamic light scattering. *Phys. Rev. E* **60**, 1988 (1999).
- [128] Addadi, L., Raz, S. & Weiner, S. Taking advantage of disorder: amorphous calcium carbonate and its roles in biomineralization. *Adv. Mater.* **15**, 959 (2003).
- [129] Raz, S., Hamilton, P. C., Wilt, F. H., Weiner, S. & Addadi, L. The transient phase of amorphous calcium carbonate in sea urchin larval spicules: the involvement of proteins and magnesium ions in its formation and stabilization. *Adv. Funct. Mater.* **13**, 480 (2003).
- [130] Faatz, M., Grohn, F. & Wegner, G. Amorphous calcium carbonate: synthesis and potential intermediate in biomineralization. *Adv. Mater.* **16**, 996 (2004).
- [131] Bolze, J., Pontoni, D., Ballauff, M., Narayanan, T. & Colfen, H. Time-resolved SAXS study of the effect of a double hydrophilic block-copolymer on the formation of CaCO₃ from a supersaturated salt solution. *J. Colloid Interface Sci* **277**, 84 (2004).
- [132] Nelson, D. F., Lax, M. & Lazay, P. D. Brillouin-scattering in anisotropic media - calcite. *Phys. Rev. B* **6**, 3109 (1972).
- [133] Van Krevelen, D. V. & Hoftyzer, P. J. *Properties of polymers*, 2 ed. (Elsevier, Amsterdam, 1976).
- [134] Jang, J. H., Ullal, C. K., Gorishnyy, T., Tsukruk, V. V. & Thomas, E. L. Mechanically tunable three-dimensional elastomeric network/air structures via interference lithography. *Nano Lett.* **6**, 740 (2006).
- [135] Ye, L., Liu, J., Sheng, P. & Weitz, D. A. Sound-propagation in suspensions of solid spheres. *Phys. Rev. E* **48**, 2805 (1993).
- [136] Kriegs, H., Petekidis, G., Fytas, G., Penciu, R. S., Economou, E. N. & Schofield, A. B. Phonons in suspensions of hard sphere colloids: volume fraction dependence. *J. Chem. Phys.* **121**, 7849 (2004).

- [137] Penciu, R. S., Kafesaki, M., Fytas, G., Economou, E. N., Steffen, W., Hollingsworth, A. & Russel, W. B. Phonons in colloidal crystals. *Europhys. Lett.* **58**, 699 (2002).
- [138] Psarobas, I. E., Modinos, A., Sainidou, R. & Stefanou, N. Acoustic properties of colloidal crystals. *Phys. Rev. B* **65**, 064307 (2002).
- [139] Giugni, A. & Cunsolo, A. Structural relaxation in the dynamics of glycerol: a joint visible, UV and X-ray inelastic scattering study. *J. Phys. Condens. Matter* **18**, 889 (2006).
- [140] Gaunard, G. C. & Wertman, W. Comparison of effective medium theories for inhomogeneous continua. *J. Acoust. Soc. Am* **85**, 541 (1989).
- [141] Sainidou, R., Stefanou, N. & Modinos, A. Formation of absolute frequency gaps in three-dimensional solid phononic crystals. *Phys. Rev. B* **66**, 212301 (2002).
- [142] Li, C., Han, X. Y. & Wen, X. S. Band-structure results for elastic waves interpreted with multiple-scattering theory. *Phys. Rev. B* **74**, 153101 (2006).
- [143] Zhao, H. G., Liu, Y. Z., Wang, G., Wen, J. H., Yu, D. L., Han, X. Y. & Wen, X. S. Resonance modes and gap formation in a two-dimensional solid phononic crystal. *Phys. Rev. B* **72**, 012301 (2005).
- [144] Gu, Z. Z., Fujishima, A. & Sato, O. Fabrication of high-quality opal films with controllable thickness. *Chem. Mater.* **14**, 760 (2002).
- [145] Jiang, P., Bertone, J. F., Hwang, K. S. & Colvin, V. L. Single-crystal colloidal multilayers of controlled thickness. *Chem. Mater.* **11**, 2132 (1999).
- [146] Fustin, C. A., Glasser, G., Spiess, H. W. & Jonas, U. Site-selective growth of colloidal crystals with photonic properties on chemically patterned surfaces. *Adv. Mater.* **15**, 1025 (2003).
- [147] Asher, S. A., Weissman, J. M., Tikhonov, A., Coalson, R. D. & Kesavamoorthy, R. Diffraction in crystalline colloidal-array photonic crystals. *Phys. Rev. E* **69**, 066619 (2004).
- [148] Sigalas, M., Kushwaha, M. S., Economou, E. N., Kafesaki, M., Psarobas, I. E. & Steurer, W. Classical vibrational modes in phononic lattices: theory and experiment. *Z. Kristallogr.* **220**, 765 (2005).

Acknowledgement

First of all, I would like to give my most sincere thanks to Prof. G. Fytas with whom I have been closely working during the past two and a half years. From him I inherited precious knowledge on Brillouin light scattering and phononics. I always feel that it was my great luck to become his PhD student, one of the many reasons is that he never gives me the feeling that he is my senior and tries to keep distance from me. Instead he is more like a friend who would like to share his knowledge and experiences with me. Working with such a fellow under an academically free atmosphere was really a fun, this was a great feeling I had never experienced before I met him. His great passion toward science and optimistic attitude toward life and career never stop affecting me, particularly during his visit in Mainz. Besides giving me great scientific help, he also shared with me his rich academic and life experiences, which certainly are treasure to me. In addition, I have to deliver my pure-hearted appreciation for his tolerance in taking all kinds of my emotions and sometimes, very negative ones.

Secondly, I have to express my deep thanks to Prof. H.-J. Butt for offering me such a rare opportunity to work in his group. Indeed, my thanks to Prof. Butt have to date back to October 2001 and go back to the city of Siegen, when and where I started my Master study in chemistry. He taught us physical chemistry at the time and strongly motivated me to come to the interface between chemistry and physics. But for him, I would most probably follow a completely different path and would have certainly missed the life in Mainz. His constant concern of my work was important to the outcome.

I would like to give my great thanks to Prof. W. Steffen at MPIP who gave me a lot of help in BLS instrumentation. He also helped me with all kinds of headache computer problems. Moreover, he provided me great assistance in my personal affairs, smoothing out my life in Mainz, which I appreciate very much. He was also so kind to proofread my thesis.

I have to thank Dr. U. Jonas and Jianjun Wang at MPIP for their collaboration on colloidal crystals. Working together with them was an amazingly pleasant and impressive

experience, for both their great personality and their expertise in colloidal crystal fabrication. Our collaboration led to not only fruitful scientific outcome but also great friendship.

I have to thank Prof. Stefanou and Dr. R. Sainidou at University of Athens for simulation of the Lamb modes. In addition, I appreciate greatly Prof. Stefanou's kindness in detailed answering my questions on phononic crystals and careful proofreading of Chapter 2 of this dissertation. I'm also deeply in debt to Dr. R. Sainidou for my "demanding requests" in her busy days, and very much impressed with her reliability.

My sincere thanks are due to:

Taras Gorishnyy (Dept. Mat. Sci. & Eng., MIT) for the collaboration in the elastic properties of multilayer films and discussion of the finite element analysis.

Anna V. Kiyanova and Dr. M. Efremov (Dept. Chem. Eng., University of Wisconsin) for the preparation of the supported thin films and for intensive discussions.

Dr. R. S. Penciu (Dept. Phys., University of Crete) for "single-phonon scattering-cross-section calculations".

Micheal Faatz (MPIP, Mainz) for providing the amorphous CaCO_3 particles.

In MPIP Mainz, I would also like to thank:

Andreas Best for providing the temperature-control program for the sample cell and his consistent help with confocal microscopy.

Dr. R. Berger for helping me with the tapping mode AFM measurement.

Prof. J. S. Gutmann for the x-ray reflectivity measurement.

Dr. G. Tommaseo for the technical assistance during my first five months in Mainz. I still cherish those happy times we had together.

And those in AK-Butt who gave me manifold help at different times during my PhD period, asking for forgiveness for not being able to recall all of them.

Finally, I have to express my deepest thanks to my great parents for their unconditional love and support, and for their tolerance of the single child of the family staying away from them for so long time!

衷心感谢我伟大的父母一直以来对我的无私奉献，全力支持，和深情的爱！

Curriculum Vitae

Name: *Wei Cheng*

Date of Birth: *Apr. 2nd, 1979*

Place of Birth: *Hunan, China*

Education:

Sep. 1997 — Jun. 2001

Department of Polymer Science and Engineering, School of Chemistry and Chemical Engineering, Shanghai Jiao Tong University, Shanghai, China

Degree obtained: *Bachelor in Engineering*

Thesis: *Synthesis and characterization of a novel type of water-soluble hyperbranched polyester*

Representative award: *Outstanding student of Shanghai Jiao Tong University, 2000*

Oct. 2001 — Feb. 2004

Department of Chemistry, University of Siegen, Siegen, Germany

Degree obtained: *Master in Chemistry*

Thesis: *Surface and resonance enhanced micro-Raman spectroscopy of Rhodamine 6G: wavelength dependence of the continuum background*

Representative award: *“Studienpreis Chemie” of University of Siegen, 2004*

Jun. 2004 — now

Max Planck Institute for Polymer Research, Mainz, Germany

Degree to be obtained: *PhD in natural science (Dr. rer. nat.)*

List of publications:

1. Gao, C., Yan, D. Y. & **Cheng, W.** Self-association and degree of branching: Fluorescence-probe study of hyperbranched poly(sulfone-amine)s in aqueous solution. *Macromolecular Rapid Communications* **23**, 465 (2002).
 2. Gao, C., Yan, D. Y., Zhang, B. & **Cheng, W.** Fluorescence studies on the hydrophobic association of pyrene-labeled amphiphilic hyperbranched poly(sulfone-amine)s. *Langmuir* **18**, 3708 (2002).
 3. Gao, C., Xu, Y. M., Yan, D. Y. & **Cheng, W.** Water-soluble degradable hyperbranched polyesters: Novel candidates for drug delivery? *Biomacromolecules* **4**, 704 (2003).
-
4. Priadilova, O., **Cheng, W.**, Tommaseo, G., Steffen, W., Gutmann, J. S. & Fytas, G. Probing the micromechanical behavior of semicrystalline polypropylene films by Brillouin spectroscopy. *Macromolecules* **38**, 2321 (2005).
 5. Faatz, M., **Cheng, W.**, Wegner, G., Fytas, G., Penciu, R. S. & Economou, E. N. Mechanical strength of amorphous CaCO₃ colloidal spheres. *Langmuir* **21**, 6666 (2005).
 6. **Cheng, W.**, Wang, J. J., Jonas, U., Steffen, W., Fytas, G., Penciu, R. S. & Economou, E. N. The spectrum of vibration modes in soft opals. *Journal of Chemical Physics* **123**, 121104 (2005).
 7. **Cheng, W.**, Fytas, G., Kiyanova, A. V., Efremov, M. Y. & Nealey, P. F. Submicron polymer gratings: Optical diffraction and spontaneous Brillouin scattering. *Macromolecular Rapid Communications* **27**, 702 (2006).
 8. **Cheng, W.**, Wang, J. J., Jonas, U., Fytas, G. & Stefanou, N. Observation and tuning of hypersonic bandgaps in colloidal crystals. *Nature Materials* **5**, 830 (2006).
 9. **Cheng, W.**, Gorishnyy, T., Krikorian, V., Fytas, G. & Thomas, E. L. In-plane elastic excitations in 1D polymeric photonic structures. *Macromolecules* **39**, 9614 (2006).